

University of Windsor

Scholarship at UWindor

Electronic Theses and Dissertations

Theses, Dissertations, and Major Papers

8-23-2019

The Use of Fluorite in Assessing Fluid History and Metal Endowment in Hydrothermal Sn-W-Mo Deposits: An Example from Mt. Pleasant, Canada

James Greene
University of Windsor

Follow this and additional works at: <https://scholar.uwindsor.ca/etd>

Recommended Citation

Greene, James, "The Use of Fluorite in Assessing Fluid History and Metal Endowment in Hydrothermal Sn-W-Mo Deposits: An Example from Mt. Pleasant, Canada" (2019). *Electronic Theses and Dissertations*. 7784.

<https://scholar.uwindsor.ca/etd/7784>

This online database contains the full-text of PhD dissertations and Masters' theses of University of Windsor students from 1954 forward. These documents are made available for personal study and research purposes only, in accordance with the Canadian Copyright Act and the Creative Commons license—CC BY-NC-ND (Attribution, Non-Commercial, No Derivative Works). Under this license, works must always be attributed to the copyright holder (original author), cannot be used for any commercial purposes, and may not be altered. Any other use would require the permission of the copyright holder. Students may inquire about withdrawing their dissertation and/or thesis from this database. For additional inquiries, please contact the repository administrator via email (scholarship@uwindsor.ca) or by telephone at 519-253-3000ext. 3208.

The Use of Fluorite in Assessing Fluid History and Metal Endowment in Hydrothermal
Sn-W-Mo Deposits: An Example from Mt. Pleasant, Canada

By

James Greene

A Thesis

Submitted to the Faculty of Graduate Studies
through the School of the Environment
in Partial Fulfillment of the Requirements for
the Degree of Master of Science
at the University of Windsor

Windsor, Ontario, Canada

2019

© 2019 James Greene

The Use of Fluorite in Assessing Fluid History and Metal Endowment in Hydrothermal
Sn-W-Mo Deposits: An Example from Mt. Pleasant, Canada

by

James Greene

APPROVED BY:

S. Mundle
Department of Chemistry and Biochemistry

A. Polat
School of the Environment

I. Samson, Co-Advisor
School of the Environment

J. Gagnon, Co-Advisor
School of the Environment

August 23, 2019

DECLARATION OF ORIGINALITY

I hereby certify that I am the sole author of this thesis and that no part of this thesis has been published or submitted for publication.

I certify that, to the best of my knowledge, my thesis does not infringe upon anyone's copyright nor violate any proprietary rights and that any ideas, techniques, quotations, or any other material from the work of other people included in my thesis, published or otherwise, are fully acknowledged in accordance with the standard referencing practices. Furthermore, to the extent that I have included copyrighted material that surpasses the bounds of fair dealing within the meaning of the Canada Copyright Act, I certify that I have obtained a written permission from the copyright owner(s) to include such material(s) in my thesis and have included copies of such copyright clearances to my appendix.

I declare that this is a true copy of my thesis, including any final revisions, as approved by my thesis committee and the Graduate Studies office, and that this thesis has not been submitted for a higher degree to any other University or Institution.

ABSTRACT

The Mount Pleasant Sn-W-Mo deposit is located in southern New Brunswick, Canada and consists of two zones: the North Zone (NZ) and the Fire Tower Zone (FTZ). The North Zone hosts predominantly Sn with minor W-Mo mineralization, whereas the Fire Tower Zone hosts predominantly Mo and W with minor Sn mineralization. Fluorite is an important gangue mineral as it is ubiquitous throughout the deposit and is used to provide a record of fluid evolution. The complexity of the deposit is apparent from the deposit-scale to micrometer-scale trace-element variations in fluorite crystals such that fluorite is key to understanding the composition of the ore-forming fluids and their relationship to the metal endowment of the deposit. Tungsten- and Mo-related fluorite crystals from the FTZ generally exhibit homogenous to simply-zoned cathodoluminescent (CL) character, whereas Sn-related fluorite from the NZ is complexly zoned. Based on LA-ICP-MS analysis, distinct bivariate trends (most notably between Fe and Rb) that are unique to each mineralization assemblage suggest that three compositionally different fluids were responsible for the three types of mineralization. Intra-crystal trace-element variability in single fluorite crystals define trends consistent with Rayleigh fractionation during fluid exsolution and suggest these three fluids originated from three magmas that underwent pulsed crystallization. The W/Mo ratio in W-related fluorite (~3) is higher than in Mo-related fluorite (~0.5), reflecting precipitation from chemically distinct fluids with metal signatures that in part reflect the associated ore bodies. No Sn was detected in samples of fluorite from Mount Pleasant.

DEDICATION

This thesis is dedicated to my family and girlfriend for their love, support, and encouragement throughout my journey. I could not have done this without them.

ACKNOWLEDGEMENTS

I would like to express my sincere gratitude and respect to Dr. Iain Samson, my co-advisor, for all his support throughout this journey. His commitment to high-caliber research and genuine compassion for teaching has made this journey more fulfilling and rewarding than I had ever imagined. Without his guidance, this dissertation would not be possible.

I would also like to express my sincere appreciation for Dr. Joel Gagnon, my co-advisor, for all his support through my research. His passion for research and invaluable advice provided me with necessary support throughout my research. He also encouraged and facilitated my professional growth outside of research, which led to a position on the department council, search committees, appointments committees, and my involvement with the surrounding community, for which I am forever thankful. This research was funded by NSERC research grants to Dr. Iain Samson and Dr. Joel Gagnon.

I also want to thank all the faculty and staff at the University of Windsor who helped me along my journey, especially Melissa Price for her indispensable help and wealth of knowledge. I also want to thank Sharon Lackie and J.C. Barrette from the Great Lakes Institute of Environmental Research for their support during SEM and LA-ICP-MS analyses. I thank all the current and former graduate students in the department for their camaraderie and help along the way.

Finally, I would like to give a special thanks to my family and girlfriend. Their love and support made this journey possible.

TABLE OF CONTENTS

DECLARATION OF ORIGINALITY	iii
ABSTRACT	iv
DEDICATION	v
ACKNOWLEDGEMENTS	vi
LIST OF TABLES	ix
LIST OF FIGURES	x
LIST OF ELECTRONIC APPENDICES	xiv
LIST OF ABBREVIATIONS/SYMBOLS	xv
CHAPTER 1 Introduction	1
CHAPTER 2 Geologic Setting	3
CHAPTER 3 Analytical Methods	6
3.1 Sampling	6
3.2 Scanning electron microscopy-energy dispersive X-ray spectrometry (SEM-EDS).....	6
3.3 Scanning electron microscopy-cathodoluminescence (SEM-CL)	6
3.4 Laser-Ablation Inductively-Coupled Plasma Mass Spectrometry (LA-ICP-MS).....	6
CHAPTER 4 Results	16
4.1 Fluorite Petrography.....	16
4.1.1 W-related Fluorite.....	16
4.1.2 Mo-related Fluorite.....	16
4.1.3 Sn-related Fluorite I.....	16
4.1.4 Sn-related Fluorite II	17
4.2 Fluorite CL Characteristics	17
4.3 Trace-Element Concentrations in Fluorite	18

4.3.1 Intracrystal Variability.....	19
CHAPTER 5 Discussion	80
5.1 Previous Work.....	80
5.2 Fluorite Growth History	80
5.3 Implications of Fluorite Chemistry	83
5.4 Comparison with Other Deposits	86
CHAPTER 6 Conclusions	96
Suggestions for Future Work	97
REFERENCES	98
VITA AUCTORIS	103

LIST OF TABLES

Table 3.1 Colour coding depicting quality of laser ablation spectra.....	12
Table 3.2 Explanation of wording used to describe the quality of laser ablation holes.....	13
Table 3.3 Testing of laser power (%) and repetition rate (Hz) in clear fluorite.....	14
Table 3.4 Testing of laser power (%) and repetition rate (Hz) in purple fluorite.....	15

LIST OF FIGURES

Figure 2.1 Cross section 15500E through the Fire Tower Zone and North Zone, Mount Pleasant, illustrating the relationship between the granitic phases and mineralized bodies	4
Figure 2.2 Simplified paragenetic sequence of minerals in the North Zone and Fire Tower Zone.....	5
Figure 3.1 An example of good quality laser ablation spectra (colour code green).....	8
Figure 3.2 An example of suboptimal quality laser ablation spectra with rising Ca signal example (colour code yellow).....	9
Figure 3.3 An example of poor quality laser ablation spectra (colour code red).....	10
Figure 3.4 Explanation of wording used to describe the quality of laser ablation holes.....	11
Figure 4.1 PPL image of W-related fluorite, wolframite, chlorite, and quartz.....	21
Figure 4.2 (a) PPL image of W-related fluorite (b) and (c) BSE images showing numerous wolframite (green arrows), monazite (yellow arrow) and REE-fluorocarbonate (red arrows) inclusions within the fluorite.....	22
Figure 4.3 PPL image of Mo-related fluorite within an assemblage of fluorite + molybdenite + quartz + monazite. Red arrow denotes where fluorite protrudes into quartz.....	23
Figure 4.4 PPL + Reflected light image of Mo-related fluorite, molybdenite, and quartz illustrating how molybdenite mantles fluorite. Red arrow denoting where molybdenite is present within a fracture in fluorite....	24
Figure 4.5 TL and RL image of Sn-related fluorite I in an assemblage comprising fluorite + chlorite + arsenopyrite + cassiterite + quartz.....	25
Figure 4.6 TL image of a vein in earlier Sn-related fluorite I containing chlorite, arsenopyrite, and cassiterite.....	26
Figure 4.7 TL image of a hexagonal chlorite pseudomorph that has replaced biotite.....	27
Figure 4.8 TL image of topaz crystals within earlier Sn-related fluorite I and radiating around quartz and chlorite grains.....	28
Figure 4.9 TL and BSE image identifying the mineral inclusions in the rim of Sn-related I as REE-fluorocarbonates (red arrows) and monazite (yellow arrows).....	29
Figure 4.10 TL image of Sn-related fluorite II crosscutting arsenopyrite and quartz (red arrows).....	30
Figure 4.11 TL image of cassiterite in Sn-related fluorite II.....	31
Figure 4.12 TL image of cassiterite that has precipitated into open space within arsenopyrite grains.....	32
Figure 4.13 CL image of W-related fluorite showing simple planar zoning with alternating bright and dark CL zones.....	33
Figure 4.14 CL image of W-related fluorite showing a planar zoned crystal with a prominent, darker CL zone filled with numerous wolframite (green arrows), REE-fluorocarbonates (red arrows), and monazite (gold arrow) inclusions.....	34

Figure 4.15 CL images of W-related fluorite illustrating that the prominent, darker CL zone with abundant mineral inclusions occurs in between planar zones, within the core of a crystal, and as a rim.....	35
Figure 4.16 CL image of Mo-related fluorite showing a bright CL rim where mantled by molybdenite (red arrows).....	36
Figure 4.17 CL image of Sn-related fluorite I showing a bright complex core, surrounded by planar zoning with sporadic dissolution features.....	37
Figure 4.18 Core of Sn-related I fluorite with grains of quartz that are mantled by thin dark CL zones of fluorite that contain acicular topaz crystals.....	38
Figure 4.19 CL image within the core of Sn-related fluorite I depicting the two stages of bright CL growth (red arrows).....	39
Figure 4.20 CL image with red arrows indicating where irregular dull zones mantle topaz-rich dark CL zones in Sn-related fluorite I.....	40
Figure 4.21 Red box denoting a dissolution feature in Sn-related fluorite I.....	41
Figure 4.22 CL image of Sn-related fluorite I with REE-fluorocarbonate (red arrows) and monazite (yellow arrows) inclusions in the dark CL rim....	42
Figure 4.23 An uncommon crystal of bright CL Sn-related fluorite II with planar growth zoning.....	43
Figure 4.24 Dark-CL fluorite crystal of Sn-related fluorite II that has experienced veining and dissolution.....	44
Figure 4.25 CL and TL images showing the correlation between bright-CL dissolution features and cassiterite grains.....	45
Figure 4.26 CL image of Sn-related fluorite II with red arrows illustrating the two stages of bright CL fluorite that crosscuts dark CL fluorite.....	47
Figure 4.27 Summary of fluorite CL characteristics exhibited at Mount Pleasant.....	48
Figure 4.28 Box whisker plot showing the concentration of Mo and W in the FTZ and NZ.....	49
Figure 4.29 Box whisker plot showing the concentration of Mo and W in the four different types of fluorite.....	50
Figure 4.30 Box whisker plot showing overlap in element concentrations among the different types of fluorite.....	51
Figure 4.31 Box whisker plot showing the most notable differences in element concentrations among the different types of fluorite.....	52
Figure 4.32 Box whisker plot showing the highest REE concentrations in Mo-related fluorite, followed by Sn-related fluorite I, W-related fluorite, and Sn-related fluorite II.....	53
Figure 4.33 Element concentration plots of Zn, Cu, Fe, and Rb versus total REE showing a negative correlation.....	54
Figure 4.34 Element concentration plots of Cu vs Rb, Zn vs Fe, Sr vs Rb, and Cs vs Rb to show they all covary.....	55
Figure 4.35 Fe vs Rb plot showing each three distinct trends correlated to the primary ore mineralization.....	56
Figure 4.36 Element concentration plot of W versus total REE showing both a negative correlation and a positive correlation.....	57
Figure 4.37 Elemental concentration plots of Ce vs La, Gd vs Nd, Lu vs Yb, and Tm vs Ho to show they all covary.....	58

Figure 4.38 Lanthanum versus Ytterbium plot showing a positive correlation with significant scatter.....	59
Figure 4.39 CL image of W-related fluorite and a line graph illustrating changes in La/Yb, within singular zones, from the earliest generation to fluorite to the latest.....	60
Figure 4.40 CL image of Sn-related fluorite and a line graph illustrating changes in La/Yb from core to rim within singular zones.....	61
Figure 4.41 Lanthanum / Ytterbium versus Total REE plot showing a negative correlation.....	62
Figure 4.42 CL image of W-related fluorite and a line graph illustrating how Fe, Cu, Zn, Rb, Sr, La, and Yb vary throughout the crystal.....	63
Figure 4.43 CL image of W-related fluorite and a line graph illustrating how Fe, Cu, Zn, Rb, Sr, Mo, and Pb all covary from core to rim within singular zones.....	64
Figure 4.44 CL image of W-related fluorite and a line graph illustrating the exception where Fe, Cu, Zn, Rb, Sr, Mo, and Pb do not covary within a crystal.....	65
Figure 4.45 CL image of W-related fluorite and a line graph illustrating changes in W, La, and Ho from core to rim within singular zones.....	66
Figure 4.46 CL image of W-related fluorite and a line graph illustrating changes in W, La, and Ho from core to rim within singular zones.....	67
Figure 4.47 CL image of Sn-related fluorite I and a line graph illustrating how Fe, Cu, Zn, Rb, Sr, Mo, and Pb all covary from core to rim within singular zones.....	68
Figure 4.48 CL image of Sn-related fluorite I and a line graph illustrating how Fe, Cu, Zn, Rb, Sr, La, and Yb vary throughout the crystal.....	69
Figure 4.49 CL image of Sn-related fluorite I and a line graph illustrating how W, Fe, Cu, Rb, Sr, La, and Yb vary within a crystal.....	70
Figure 4.50 CL image of Sn-related fluorite II and a line graph illustrating how Fe, Cu, Zn, Rb, Sr, Mo, and Pb vary within a crystal.....	71
Figure 4.51 CL image of Sn-related fluorite II and a line graph illustrating how Fe, Cu, Rb, Sr, Pb, La, and Yb vary throughout the crystal.....	72
Figure 4.52 CL image of Sn-related fluorite II and a line graph illustrating how W, Fe, Cu, Rb, Sr, La, and Yb vary within a crystal.....	73
Figure 4.53 Box whisker plot comparing the planar zones in MPS to the dark CL, mineral inclusion-rich zones.....	74
Figure 4.54 Laser ablation spectra of a zone of W-related fluorite with numerous REE-mineral inclusions, illustrating the uniformity of the spectra.....	75
Figure 4.55 Box whisker plot comparing element concentrations in dull homogenous Mo-related fluorite to those with a bright rim where mantled by molybdenite.....	76
Figure 4.56 Box whisker plot showing Fe, Cu, Zn, Rb, Sr, Mo, and Cs decrease in concentration from Type 1 to Type 4 Sn-related fluorite I.....	77
Figure 4.57 Box whisker plot showing As, W, REE, Y, and Th increase in concentration from Type 1 to Type 4 Sn-related fluorite I.....	78

Figure 4.58 Box whisker plot showing Pb, Bi, and U are similar in concentration in Type 1, Type 2, and Type 4 but are lower in concentration in Type 3 Sn-related fluorite I.....	79
Figure 4.59 Box whisker plot showing similar element concentrations of three different generations of Sn-related fluorite II in one grain of fluorite...	80
Figure 5.1 An example of laser ablation spectra from fluorite showing Sn below the limit of detection.....	89
Figure 5.2 Iron versus Rubidium plot showing all Fe/Rb trends and their same correlations with La/Yb.....	90
Figure 5.3 La/Yb versus total REE plot showing a negative correlation.....	91
Figure 5.4 Cesium versus Rubidium plot showing how Rb and Cs vary from zone to zone within a single crystal of W-related fluorite, overlain by the Cs/Rb fields of all samples.....	92
Figure 5.5 Zinc versus Rubidium plot showing a positive correlation.....	93
Figure 5.6 Two compatible elements representing the composition of the fractionating phase. Cf = concentration in fractionating phase (mineral or fluid). Data labels = f.....	94
Figure 5.7 Bivariate plots showing Cs plotted against Fe, Rb, Zn, and Sr....	95
Figure 5.8 An incompatible element plotted against a compatible element, representing the composition of the fractionating phase. Cf = concentration in fractionating phase (mineral or fluid). Data labels = f.....	96
Figure 5.9 Iron versus rubidium plot showing the various Fe/Rb trends at Mount Pleasant and other W, Mo, and Sn deposits.....	97

LIST OF ELECTRONIC APPENDICES

Appendix A: Trace-element composition (LA-ICP-MS) of fluorite from Mount Pleasant

LIST OF ABBREVIATIONS/SYMBOLS

Asp = Arsenopyrite

Chl = Chlorite

Cf = concentration in fractionating phase

CL = Cathodoluminescence

Cst = Cassiterite

EDS = Energy dispersive X-ray spectrometry

Fl = Fluorite

FTZ = Fire Tower Zone

GI = Granite-I

GII = Granite-II

GIII = Granite-III

HREE = Heavy rare-earth elements

LA-ICP-MS = Laser-ablation Inductively-Coupled Plasma Mass Spectrometry

LREE = Light rare-earth elements

Mnz = Monazite

Mol = Molybdenite

NZ = North Zone

P = Pressure

Qtz = Quartz

REE = Rare-earth elements

SEM = Scanning electron microscopy

T = Temperature

Wlf = Wolframite

CHAPTER 1

Introduction

Ore deposits are often thought of in terms of: (1) where the metals were sourced, (2) how the metals were transported and (3) how the metals were trapped or concentrated where they occur today. In deposits with complex fluid histories, determining which fluids contain the metals is key in understanding the formation of an ore deposit. One way to identify which fluid carried the metals as well as to understand the fluid history is to analyze a mineral that serves as a proxy for fluid composition and physiochemical conditions. Laser ablation inductively coupled plasma mass spectrometry (LA-ICP-MS) can be used to determine the element concentrations within a mineral and track the chemical evolution throughout a crystal.

Numerous ore deposits have been documented and their parageneses researched, but very few studies have characterized the relationship between metal concentrations in the hydrothermal fluids and the metal endowment of the mineral deposit. Research has been done that shows a positive correlation between the metal content of the parent aqueous fluid, the type of mineralization, and the metal endowment (Audetat et al., 2000; 2008), but it remains unclear if this relationship is seen in other hydrothermal deposits. More research needs to be conducted and particular attention needs to be given to the minerals sampled to ensure they represent the mineralizing fluids of interest.

Mount Pleasant is a Sn-W-Mo deposit located in southern New Brunswick and hosts two mineralized zones, the North Zone and Fire Tower Zone, that contain different proportions of ore minerals, making it a suitable place to examine the relationship between metal concentrations and metal endowment. The Fire Tower Zone (FTZ) hosts a large low-grade orebody of W-Mo mineralization that occurs mainly in the lower part of a breccia pipe as well as the upper part of the underlying fine-grained granite (Sinclair et al., 2006). The North Zone (NZ) hosts a number of Sn-bearing orebodies. Kooiman et al. (1986) noticed crosscutting mineralized fractures and veins, suggesting mineralization occurred in multiple stages. In the FTZ it was concluded that earlier stages were wolframite-rich and later stages were molybdenite-rich, both of which have been superimposed by tin-bearing polymetallic veins and replacement bodies. Samson (1990) conducted a fluid inclusion study that noted both stages of mineralization being associated with subcritical orthomagmatic fluids and suggested that the fluids responsible for W-Mo and Sn mineralization originated from two different granitic phases. Fluorite is ubiquitous at Mount Pleasant and is associated with wolframite, molybdenite, and cassiterite, making it an ideal proxy for fluid composition and physicochemical conditions.

Fluorite (CaF_2), a common gangue mineral in mineral deposits, and at Mount Pleasant in particular, has an isometric lattice structure with Ca^{2+} cations in eightfold coordination with F^- anions. The Ca^{2+} ion in fluorite can be substituted by Li^+ , Na^+ , K^+ , Rb^+ , Mg^{2+} , Mn^{2+} , $\text{Fe}^{2+,3+}$, Zn^{2+} , Sr^{2+} , Y^{3+} , Zr^{4+} , Ba^{2+} , lanthanides ions, Pb^{2+} , Th^{4+} , and U^{4+} (Bailey et al., 1974; Bill and Calas, 1978; Gagnon et al., 2003; Schwinn and Markl, 2005; Xu et al., 2012; Deng et al., 2014; Mao et al., 2015).

Vacancies and defects in the crystal structure are common in fluorite leading to a large suite of trace element substitutions in the form of impurities that otherwise possibly would not be incorporated. With several different ways to incorporate a large suite of trace elements into fluorite, its trace element chemistry could potentially be used to infer aspects of fluid compositions, mineralizing processes, and physiochemical conditions. Fluorite trace-element chemistry has been used to assess fluorite genesis (Möller et al., 1976; Eppinger and Closs, 1990; Gagnon et al., 2003; Schwinn and Markl, 2005; Ehya, 2012; Deng et al., 2014; Makin et al., 2014; Mao et al., 2015; Assadzadeh et al., 2017). The ratio of LREE to HREE has been used to determine relative age relationships (i.e., early vs late) between fluorite crystals and zones because the ionic radii of LREE are more similar to Ca than HREE, resulting in LREE becoming depleted in the fluid earlier (Möller et al., 1976; Ekambaram et al., 1986; Eppinger and Closs, 1990; Hill et al., 2000; Ehya, 2012). Cathodoluminescence (CL) has been used to document variations in composition (Assadzadeh et al., 2017), lattice structure (Götze et al., 2013), and structural defects (Götze et al., 2013). Fluorite is known to exhibit a range of CL characteristics, making this a useful technique to understand fluorite chemistry. Assadzadeh et al. (2017) examined fluorite trace element chemistry at Mount Pleasant and noticed a positive correlation between Sn-W-Mo mineralization, REE enrichment in fluorite, and REE mineral precipitation. They ablated traverses across fluorite crystals that represent averages for multiple growth zones, with the exception of one crystal in which only three zones were ablated.

The complex fluid history at Mount Pleasant has resulted in strikingly different mineralization across the 1 km width of the deposits. The metal endowment at Mount Pleasant is not only spatially separated (i.e., the FTZ and NZ), but also temporally distinct (e.g., W mineralization, followed by Mo mineralization, and subsequent Sn mineralization). To address this, fluorite associated with each mineralization type (i.e. Sn-related, W-related, and Mo-related) was examined in detail with CL and analyzed with LA-ICP-MS to determine their trace element chemistry. This thesis presents evidence that three different ore fluids were responsible for the Sn-W-Mo mineralization, as indicated by the distinct bivariate trends in trace-element chemistry (most notably between Fe and Rb) in fluorite from the three different associated mineralization types. A comparison with Fe/Rb values in fluorite and in fluid inclusions in other Sn-W and Mo deposits suggests Fe/Rb can be used to discriminate between different sources and potentially fingerprint W and Mo mineralization.

CHAPTER 2

Geologic Setting

The Mount Pleasant W-Mo-Sn deposit is located in southern New Brunswick along the southwestern margin of the Late Devonian Mount Pleasant Caldera Complex (McCutcheon et al., 1997). The Mount Pleasant Caldera Complex consists of felsic volcanic and sedimentary units (i.e., the Piskahegan Group), and was emplaced in an anorogenic, post-collisional setting (McCutcheon et al., 1997). The Piskahegan volcanic and sedimentary units were intruded by three ca. 361 Ma granitic phases, with which the mineralization is associated (Hunt and Roddick, 1990; Sinclair et al., 2006). These granitic phases are collectively called the Mount Pleasant Porphyry (McCutcheon et al., 1997). From oldest to youngest the granitic intrusions in the FTZ are the fine-grained granite, the granite porphyry, and the porphyritic granite. (Thorne et al., 2013; Zhang et al., 2017). In the NZ, the granitic intrusion from oldest to youngest are granite-I, granite-II, and granite-III (Inverno and Hutchinson, 2004; 2006). These intrusions are mineralogically and chemically similar, and are generally fine grained (Sinclair et al., 2006; Inverno and Hutchinson, 2006). The fine-grained granite and granite-I are mineralogically and chemically similar, and show cross cutting relationships that indicate they are the oldest granites (Sinclair et al., 2006; Thorne et al., 2013). The granite porphyry/granite-II are also mineralogically and chemically similar, as are the porphyritic granite/granite-III, and as such they will be referred to as granite I (GI), granite II (GII), and granite III (GIII) (Sinclair et al., 2006; Thorne et al., 2013). Two breccia pipes have developed above these granitic intrusions in two places, termed the Fire Tower Zone (FTZ) and North Zone (NZ) (Fig. 2.1).

Although they are only one km apart, the dominant ore metals are W and Mo in the FTZ and Sn in the NZ. W-Mo mineralization is hosted primarily in granite I and the Fire Tower Zone breccia. The FTZ had a pre-mining resource of 9.4 Mt, grading 0.31 % W and 0.12% Mo (Kooiman et al., 1986). In the Fire Tower Zone, wolframite and molybdenite are the principal ore minerals, occurring with quartz, topaz, fluorite, arsenopyrite, and loellingite (Kooiman et al., 1986). Further outward from the tungsten-molybdenite orebodies the main mineral assemblage is quartz, topaz, biotite, and chlorite (Pouliot et al., 1978; Kooiman et al., 1986; Samson, 1990). Molybdenite and wolframite occur disseminated through greisenized granite and breccia, in veins, or in vugs associated with fluorite. Sn mineralization is hosted primarily in granite II, the North Zone breccia and partially in granite III (Inverno and Hutchinson, 2004; Sinclair et al., 2006). The North Zone has many mineralized zones (e.g., Contact Crest, Contact Flank, Deep Tin Zone, and Endozone) with the largest being the 1.7 Mt Upper Deep Tin zone, grading 0.68% Sn, 2.26% Zn, 0.29% Cu (Sinclair et al., 2006). In the North Zone cassiterite is the principal ore mineral, occurring with fluorite, chlorite, topaz, quartz, and arsenopyrite in vugs within the granite and disseminated in chloritized rock. Fluorite in particular occurs not only in vugs, veins, and disseminated within chloritized rock, but also as a product of replacement. Assadzadeh et al. (2017) published a paragenetic sequence of minerals in the North Zone and Fire Tower Zone, which is redrawn in

Figure 2.2. Wolframite occurs before both molybdenite and cassiterite, and fluorite occurs both before and after the ore minerals.

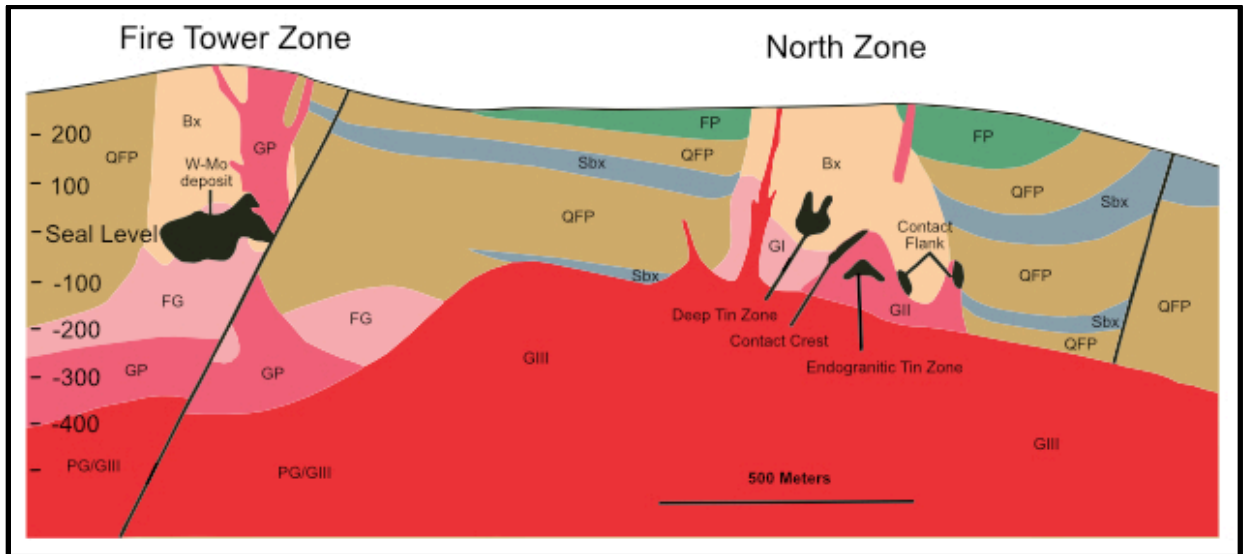


Figure 2.1 Cross section 15500E through the Fire Tower Zone and North Zone, Mount Pleasant, illustrating the relationship between the granitic phases and mineralized bodies.

(Modified after Sinclair et al., 2006)

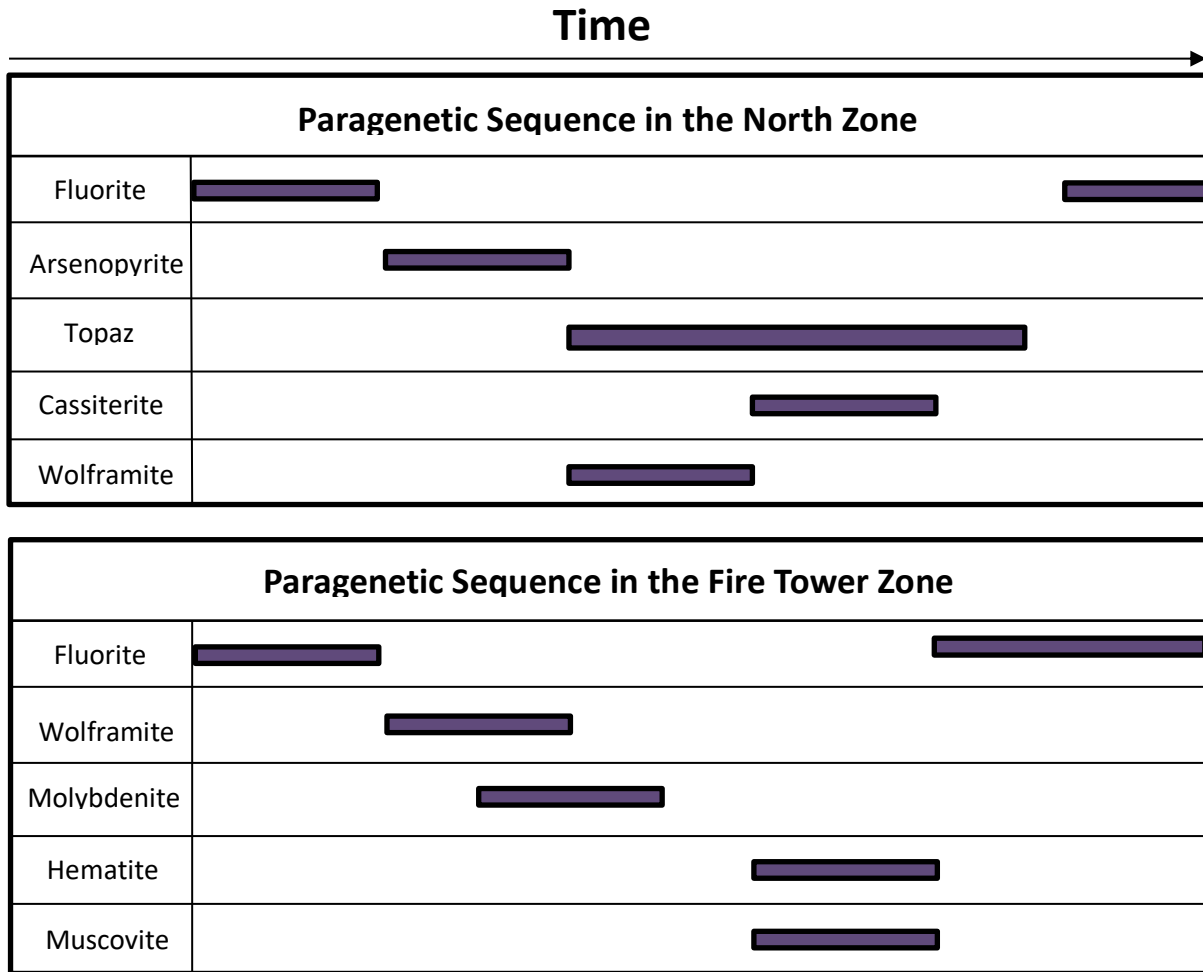


Figure 2.2 Simplified paragenetic sequence of minerals in the North Zone and Fire Tower Zone

(Modified after Assadzadeh et al., 2017)

CHAPTER 3

Analytical Methods

3.1 Sampling

Samples of fluorite hosted in mineralized granite and hydrothermal breccia were chosen as representative of both the FTZ and NZ, in addition to each type of metal association (i.e. W, Mo, and Sn-related fluorite). Sample locations are listed in Appendix A.

3.2 Scanning electron microscopy-energy dispersive X-ray spectrometry (SEM-EDS)

Fluorite at Mount Pleasant contains a variety of different mineral inclusions, most of which are too small to identify with an optical microscope. An EDAX Octane plus EDS in conjunction with a FEI® Quanta 200 FEG environmental SEM, which is located in Advanced Microscopy and Materials Characterization Facility at the University of Windsor, was used for mineral identification. Thin sections were cleaned and coated with carbon. Areas within fluorite with unidentified mineral inclusions were imaged using a back-scattered electron (BSE) detector. The settings used were as follows: an accelerating voltage of 20 kV, a spot size of 3.9 μm , a beam diameter of 2.6 nm, a beam spread of 2.5 to 5 μm , and an average working distance of 10.0 mm.

3.3 Scanning electron microscopy-cathodoluminescence (SEM-CL)

Cathodoluminescence is known to be effective at imaging growth features in fluorite. A Centaurus CL detector attached to an FEI® Quanta 200 FEG environmental SEM was used to obtain CL images, which were used to characterize growth zones, dissolution, and replacement features in fluorite. Thin sections were cleaned, carbon-coated, and attached to an aluminum stub using copper tape. Images were obtained using acceleration voltages ranging from 15 to 20 kV.

3.4 Laser-Ablation Inductively-Coupled Plasma Mass Spectrometry (LA-ICP-MS)

Trace-element analyses of fluorite were conducted at the Element and Heavy Isotope Analytical Laboratory at the University of Windsor. The laser ablation system comprises a PhotonMachines Analyte Excite 193 nm, sub 4 ns Ar-F excimer laser coupled with an Agilent 7900 fast-scanning inductively-coupled plasma quadrupole mass spectrometer (ICP-QMS).

Laser-ablation inductively-coupled plasma mass spectrometry was conducted on fluorite to determine trace-element concentrations within individual growth zones. Fluorite was analyzed for Ca, Si, Fe, Cu, Zn, As, Sr, Rb, Y, Mo, Sn, Cs, Ce, La, Pr, Nd, Sm, Eu, Gd, Dy, Tb, Er, Ho, Yb, Tm, Lu, W, Pb, Bi, Th, and U. The isotopes used to determine the element concentrations in fluorite were ^{44}Ca , ^{30}Si , ^{57}Fe , ^{63}Cu , ^{64}Zn , ^{75}As , ^{88}Sr , ^{85}Rb , ^{89}Y , ^{98}Mo , ^{120}Sn , ^{137}Ba , ^{133}Cs , ^{140}Ce , ^{139}La , ^{141}Pr , ^{146}Nd , ^{147}Sm , ^{152}Sm , ^{153}Eu , ^{155}Gd , ^{158}Gd , ^{163}Dy , ^{159}Tb , ^{166}Er , ^{165}Ho , ^{174}Yb , ^{169}Tm , ^{175}Lu , ^{184}W , ^{208}Pb , ^{209}Bi , ^{232}Th , and ^{238}U . The isotopes ^{147}Sm and ^{152}Sm were chosen to assess the potential isobaric interference of ^{152}Sm , the more abundant isotope, with ^{152}Gd and the argide interferences with Cd and Sn. The isotopes ^{155}Gd and ^{158}Gd were chosen to assess the potential isobaric interference of ^{158}Gd , the more abundant isotope, with ^{158}Dy and the molecular-ion interferences with Cd and Sn. All interferences were determined to be negligible and so the more

abundant isotopes, ^{152}Sm and ^{158}Gd , were used for quantification. Stoichiometric Ca (51.33 wt.%) in fluorite was used as the internal standard, and the NIST-610 synthetic glass standard reference material (SRM) was used as an external calibration standard.

Fluorite is a notoriously difficult mineral to ablate due to its low absorption of short wavelengths of light (Jeffries et al., 1998). The high transmission of fluorite can lead to laser energy being absorbed by the underlying glue, leading to uncontrolled ablation. The cleavage of fluorite also increases the chance of structural failure under the thermomechanical stress of ablation (Jeffries et al., 1998). This led to difficulties in performing controlled ablation. Several laser control parameters (i.e. power (mJ), repetition rate (Hz), spot size (μm), scan speed ($\mu\text{m}/\text{sec}$)) and different styles of ablation (i.e. spot versus traverse) were tested by Melissa Price in order to determine the optimal methodology for ablating fluorite.

Initial test parameters of 20 Hz, 4.1 mJ, and laser energy at 35% on a 25 μm spot, the standard operating conditions, resulted in minimal ablation. Further tests showed increasing the repetition rate and power produced more controlled ablation and better spectra (Table 3.1, 3.2, 3.3, and 3.4). The results of these experiments provided a good starting point when analyzing fluorite from Mount Pleasant. After initial tests on fluorite from Mount Pleasant, the best results resulted from a power of 4.1 mJ, a repetition rate of 100 Hz, and a spot size of 20 μm . Spot analyses were chosen over traverses to avoid mineral inclusions and contamination between individual zones in fluorite, in addition to sampling small zones with greater accuracy.

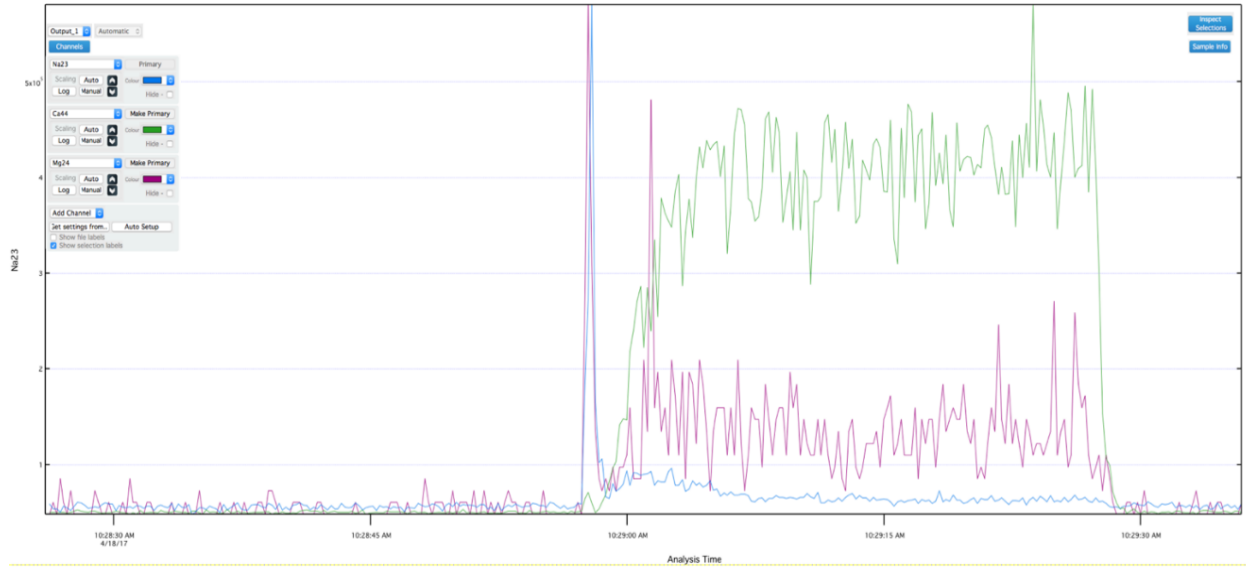


Figure 3.1 An example of good quality laser ablation spectra (colour code green).

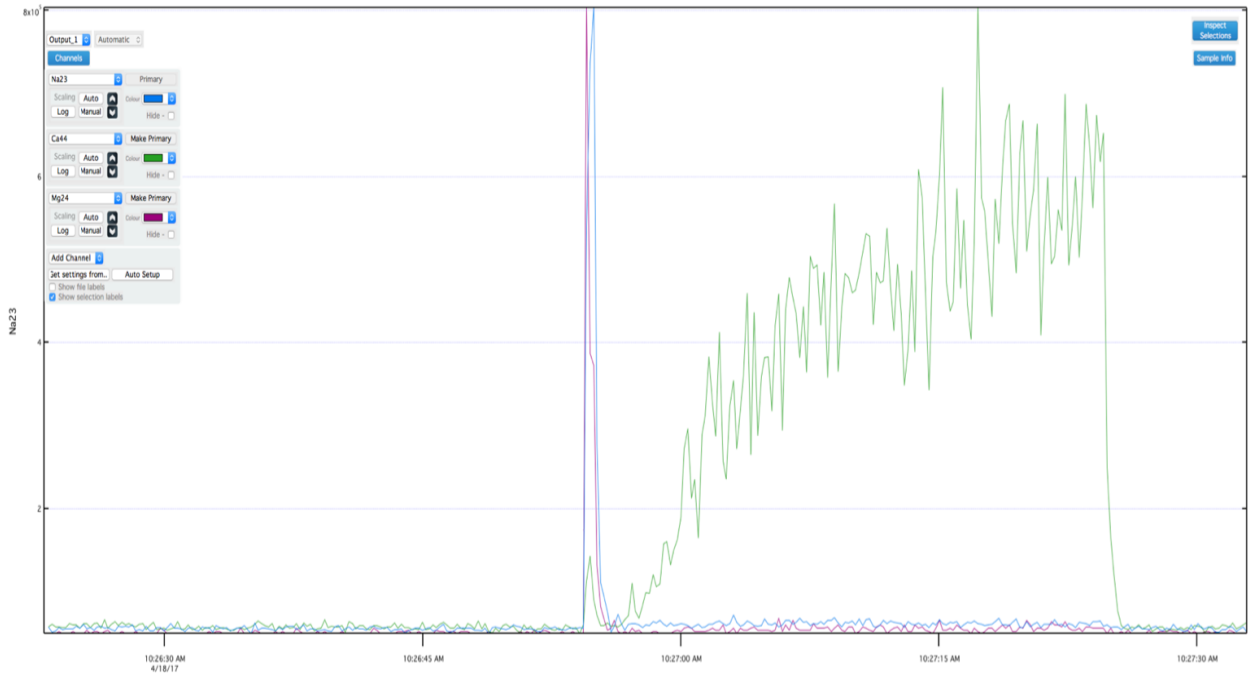


Figure 3.2 An example of suboptimal quality laser ablation spectra with rising Ca signal example (colour code yellow).

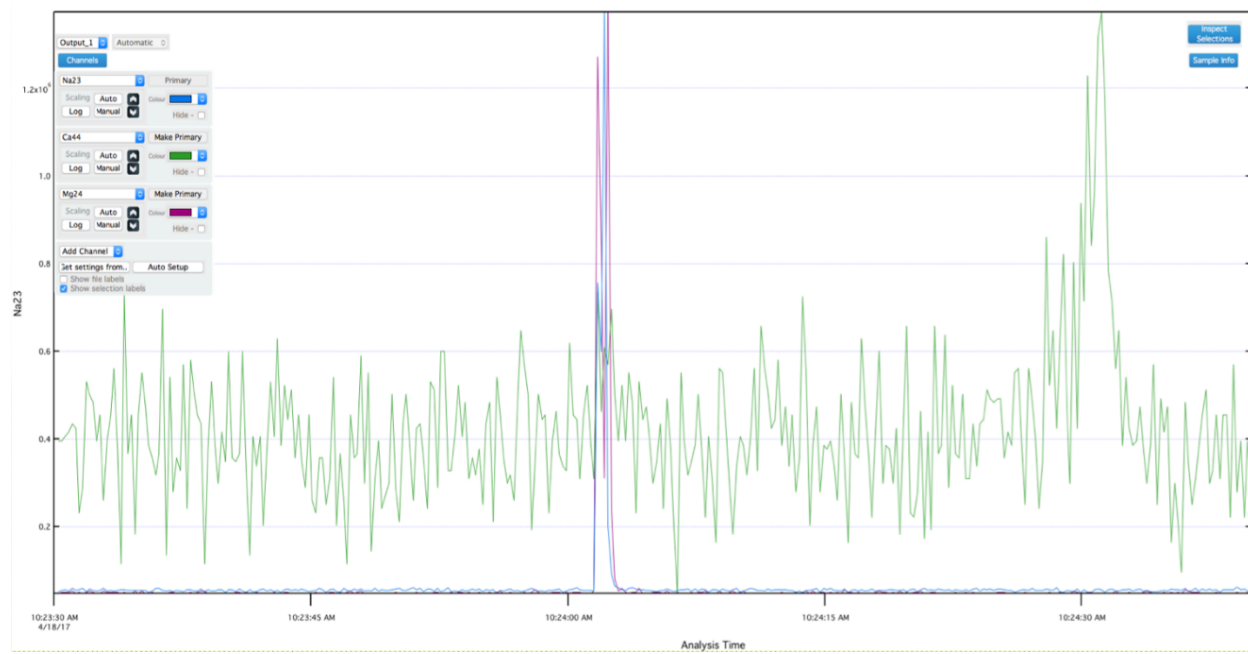


Figure 3.3 An example of poor-quality laser ablation spectra (colour code red).

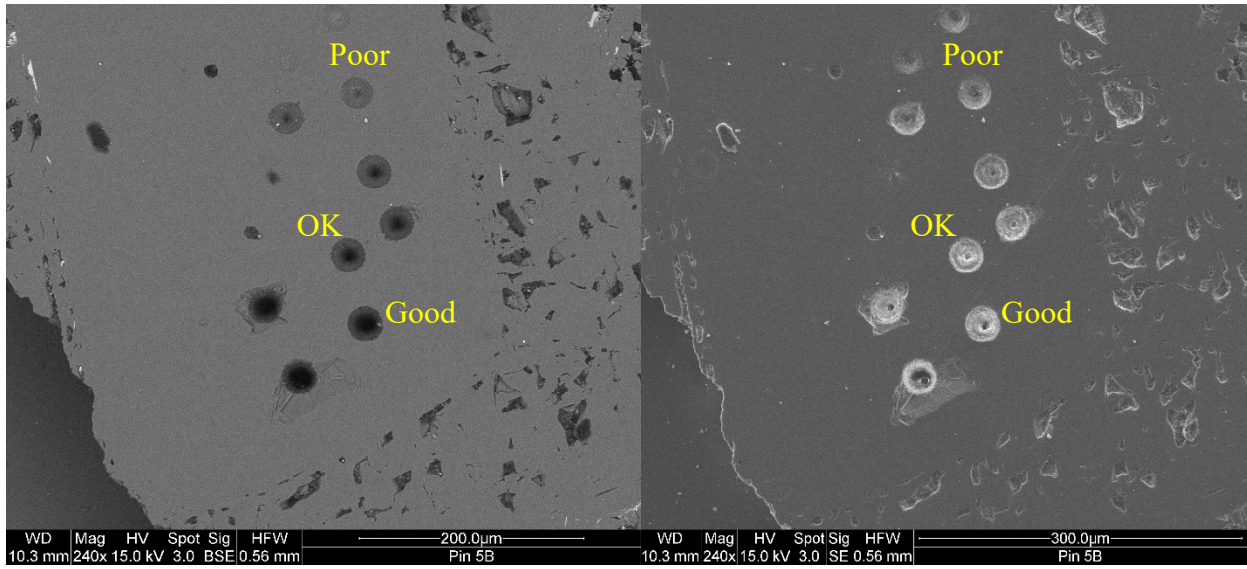


Figure 3.4 Visual representation of wording used to describe the quality of laser ablation holes.

Table 3.1 Colour coding depicting quality of laser ablation spectra (Fig. 3.1, 3.2, and 3.3)

Good quality spectra, clean and controlled, flat topped or expected peak and drop-off from drilling
Rising Ca signal that otherwise would be good quality spectrum
Either no data collection or uncontrolled, erratic data signals (unusable)

Table 3.2 Explanation of wording used to describe the quality of laser ablation holes (Fig. 4)

Description in Table 3.3	Explanation of descriptor
Good	Laser hole has defined edges and the hole is uniform and round
OK	Laser hole is present but is cone-shaped and irregular
Poor	Laser hole is not present or extremely irregular in shape, not round

Table 3.3 Testing of laser power (%) and repetition rate (Hz) in clear fluorite

Clear	20Hz	40Hz	60Hz	80Hz	100Hz	120Hz	140Hz	160Hz	180Hz	200Hz
50%	Poor	Poor	Poor	Poor	Poor	Poor	Poor	Poor	Poor	Poor
25%	Poor	Poor	Poor	Poor	Poor	Poor	OK	OK	OK	OK
75%	Poor	OK	OK	OK	OK	OK	OK	OK	OK	OK
100%	Poor	Poor	OK	OK	OK	Good	OK	OK	Good	Good

Table 3.4 Testing of laser power (%) and repetition rate (Hz) in purple fluorite

Dark	20Hz	40Hz	60Hz	80Hz	100Hz	120Hz	140Hz	160Hz	180Hz	200Hz
50%	Poor	Poor	Poor	Poor	Poor	Poor	Poor	Poor	Poor	Poor
25%	Poor	Poor	Poor	N/A	Poor	Poor	Poor	Poor	Poor	Poor
75%	Poor	Poor	Poor	Poor	Poor	Poor	Poor	Poor	Poor	Poor
100%	Good	Good	Good	Good	Good	Good	Good	Good	Good	Good

CHAPTER 4

Results

4.1 Fluorite Petrography

Fluorite crystals at Mount Pleasant are generally anhedral, but can be euhedral or subhedral, range from 1-5 mm in size, and are associated with all three of the key metallic minerals at Mount Pleasant: wolframite, molybdenite, and cassiterite. In what follows, fluorite from a given assemblage is classified based on which of the key metallic minerals is present in the greatest abundance.

4.1.1 W-related Fluorite

In the W-Mo mineralized body of the FTZ, euhedral to anhedral fluorite occurs in veins and vugs and occurs in two different assemblages. The first assemblage comprises fluorite + wolframite + chlorite + quartz + topaz + monazite (Fig. 4.1), and can contain minor amounts of molybdenite and cassiterite. In this assemblage, wolframite, molybdenite, and cassiterite grains are from 100 to 800 μm , 20 to 500 μm , and less than 25 μm in size, respectively. Wolframite is commonly partially replaced by fluorite or quartz, with fluorite replacement the more common of the two. In a couple of samples wolframite and chlorite replace fluorite, potentially suggesting two generations of fluorite in this assemblage: a pre-wolframite fluorite and a post-wolframite fluorite. Monazite is also commonly replaced by fluorite, but monazite is not a common mineral in the assemblage. Platy chlorite aggregates are abundant as disseminated masses and alteration halos around veins. These chloritized regions contain vugs that are rimmed with acicular topaz crystals and filled with fluorite (Fig. 4.1). Fluorite within these chloritized regions frequently contains topaz inclusions, but fluorite in veins lack topaz. In addition to being associated with coarse wolframite, fluorite in this assemblage can contain minor amounts of wolframite, molybdenite, and cassiterite inclusions, with cassiterite inclusions being uncommon. In a couple of samples, fluorite contains zones with abundant inclusions of wolframite, cassiterite, chlorite, bastnäsite, and hematite (Fig. 4.2).

4.1.2 Mo-related Fluorite

Another fluorite-bearing assemblage in the W-Mo mineralized body of the FTZ comprises fluorite + molybdenite + quartz + sericite + monazite (Fig. 4.3). In this assemblage, molybdenite grains typically range in length from 200 to 1000 μm . Fluorite commonly protrudes into quartz (Fig. 4). This relationship is interpreted to signify that fluorite has replaced quartz. Fluorite also crosscuts and has partially replaced monazite grains (Fig. 4.3). Molybdenite frequently mantles and is present within fractures in fluorite, suggesting it precipitated after fluorite (Fig. 4.4). Some fluorite crystals also contain molybdenite inclusions (Fig. 4.3).

4.1.3 Sn-related Fluorite I

In the Sn-mineralized bodies of the NZ, two assemblages containing fluorite are present. The fluorite in both of these assemblages is euhedral to anhedral and occurs primarily in vugs and disseminated through chloritized rock. Both fluorite-bearing assemblages comprises fluorite +

cassiterite + chlorite + quartz + arsenopyrite + topaz (Fig. 4.5). Cassiterite crystals are generally present as single euhedral grains, 125 to 5000 μm in size, or as fine-grained botryoidal masses. Fluorite in the first assemblage is mantled by arsenopyrite, that is in turn mantled by botryoidal cassiterite (i.e., wood tin) (Fig. 4.5). Quartz is present within fluorite crystals and some have been partially replaced. Some chlorite occurs as veins in fluorite that also contain cassiterite and arsenopyrite (Fig. 4.6). Chlorite is also commonly present as pseudomorphs after biotite, based on the hexagonal shape of some fine-grained chlorite aggregates (Fig. 4.7). Fluorite crystals in this assemblage commonly have abundant, radiating acicular topaz crystals in their cores. These topaz crystals may radiate out from quartz and chlorite grains, but more commonly occur as irregular aggregates within fluorite (Fig. 4.8). Fluorite in this assemblage is also characterized by REE mineral inclusion-rich rims (Fig. 4.9). Fluorite in this assemblage precipitated prior to cassiterite, is unrelated to wolframite and molybdenite, and was only observed in one sample.

4.1.4 Sn-related Fluorite II

The other fluorite-bearing assemblage has markedly different mineral relationships. Arsenopyrite and quartz are commonly crosscut by fluorite, suggesting fluorite began precipitating after arsenopyrite and quartz and partially replaced both (Fig. 4.10). Numerous cassiterite grains are disseminated through fluorite (Fig. 4.11). Where fluorite has replaced arsenopyrite, cassiterite is also commonly present in arsenopyrite crystals along with fluorite (Fig. 4.12). Anatase is a very minor component, but typically occurs as aggregates of small grains that are overgrown by cassiterite. In some samples, minor amounts of molybdenite are present as inclusions in fluorite. Because cassiterite is present as inclusions in fluorite, and molybdenite is present in low abundance, fluorite from this assemblage is hereby referred to as Sn-related fluorite II.

4.2 Fluorite CL Characteristics

Cathodoluminescence images reveal that the majority of W- and Mo-related fluorite is either homogeneous or has simple planar zoning. W-related fluorite typically shows simple planar zoning with alternating bright- and dark-CL zones (Fig. 4.13). One W-related fluorite sample (MPS-214-1166), however, is characterized by a dark-CL zone filled with abundant wolframite and REE-mineral inclusions, in addition to the typical planar zones (Fig. 4.14). This zone can occur in different parts of a crystal, such as between planar zones that have identical CL character to one another, within the core of a crystal, or as a rim (Fig. 4.15). Mo-related fluorite shows no zoning, except where it is mantled by molybdenite, where it has a bright-CL rim (Fig. 4.16).

Sn-related fluorite I in the NZ has a, primarily bright, complex core and is surrounded by planar zones with sporadic dissolution and replacement features (Fig 4.17). The zones within these crystals have been grouped into four stages of growth (Stage 1, Stage 2, Stage 3, and Stage 4), and is similar to the classification of Assadzadeh et al. (2017) for this type of fluorite (Fig. 4.17). Stage 1 represents the core of these fluorite crystals, where grains of quartz and chlorite are mantled by thin (50-100 μm) dark-CL fluorite zones that contain acicular topaz crystals (Fig. 4.18). These acicular topaz crystals extend into the surrounding bright-CL zones that make up the majority of the core. Between and surrounding these topaz-rich zones are two stages of bright-CL fluorite (Fig. 4.19). The first stage is brighter in relative CL intensity and shows no zoning. The second stage is

duller than the first stage and is characterized by planar zones that suggest it grew into open space around the first stage. Also within Stage 1 are irregular dull zones that surround both the topaz-rich, dark-CL zones and the bright-CL zones (Fig. 4.20). This complex core is overgrown by Stage 2, which consists of dull, planar, alternating light and dark-CL zones (Fig. 4.17). Stage 3 consists of zones that crosscut several earlier zones, akin to an unconformity in some instances, and are interpreted to have resulted from dissolution and replacement (Fig. 4.21). Stage 4 is represented by a dark-CL rim containing abundant REE-mineral inclusions (Fig. 4.22). From Stage 2 to Stage 4 the overall crystal form changes (Fig. 4.17). It is impossible to tell whether it is changing from octahedral to cubic or vice versa, as the orientation of the crystallographic axes are not known.

Sn-related fluorite II exhibits planar zones that range from bright to dark. Very rarely, large, bright-CL fluorite crystals with planar zoning are observed (Fig. 4.23). Most crystals typically exhibit dark-CL character with planar zoning. These dark-CL crystals commonly are either veined by bright-CL fluorite or have experienced dissolution that was followed by precipitation of bright-CL fluorite around the relicts of dark-CL fluorite (Fig. 4.24). In some cases, this bright-CL fluorite contains disseminated cassiterite (Fig. 4.25). Two stages of bright-CL fluorite seem to be present, based on crosscutting relationships (Fig. 4.26). Stage 1 represents the planar zoned, dark-CL fluorite and Stage 2 typically occurs as a rim around Stage 1 and exhibits planar zoning, suggesting open space growth. Stage 3 bright-CL fluorite is homogeneous in terms of CL character, and typically veins Stage-1 dark-CL fluorite and Stage-2 bright-CL fluorite. These CL characteristics are summarized in Figure 4.27.

4.3 Trace-Element Concentrations in Fluorite

In total, 174 LA-ICP-MS analyses on 34 individual fluorite crystals were performed to determine trace-element concentrations (Appendix 1). Ore metal concentrations are summarized in Figure 4.28 and 4.29. In this study Sn was not detected in fluorite, therefore only variations in W and Mo concentrations are described. The Mo-related fluorite and the W-related fluorite collectively represent the FTZ. The Sn-related fluorite I and Sn-related fluorite II collectively represent the NZ. Mo-related fluorite has higher concentrations of both Mo and W than W-related fluorite and both Sn-related types. Average W/Mo ratios for Sn-related fluorite I (~3) and W-related fluorite (~3) are higher overall than Mo-related fluorite (~0.5), and Sn-related fluorite II (~1). Overall, fluorite in the FTZ has higher concentrations of W and Mo compared to fluorite from the NZ (Fig. 4.28).

When comparing W-, Mo-, and Sn-related fluorite I and II, there is overlap in the concentrations of most elements (Fig. 4.30). The most distinct differences between the fluorite are as follows: W-related fluorite has higher concentrations of Zn, Mo-related fluorite has higher concentrations of As, Sn-related fluorite I has higher concentrations of Th and lower concentrations of Mo, and Sn-related fluorite II has higher concentrations of Sr (Fig. 4.31). Typically, Y and the REE are highest in concentration in Mo-related fluorite, followed by Sn-related fluorite I, W-related fluorite, and lowest in Sn-related fluorite II (Fig. 4.32).

As noted above, fluorite from different ore assemblages has notably different REE, Zn, and Sr concentrations. A bivariate plot of either Zn or Sr versus any REE element shows that there is a strong negative correlation for the sample suite as a whole (Fig. 4.33a). That relationship relative to the REE is also shown by Fe, Cu, Zn, Rb, Sr, and Cs (Fig. 4.33b-d). Iron, Cu, Zn, Rb, Sr, and Cs all covary, are positively correlated, and to varying degrees define different populations for the three metal associations (Fig. 4.34a-d). These trends are linear (e.g. Cu-Rb, Zn-Fe) or curved (e.g. Sr-Rb, Cs-Rb). The three populations are most distinctly defined by Fe and Rb, which show three separate trends with no overlap and minimal scatter (Fig. 4.35). Sn-related fluorite I and II directly overlap. All three trends exhibit a high concentration cluster and a trend that extends towards the origin. The three Rb-Fe populations are defined by Fe/Rb ratios of ~ 100 , ~ 20 , and ~ 40 , for W-related fluorite, Mo-related fluorite, and Sn-related fluorite, respectively. All three trends have an r^2 value greater than 0.97. Tungsten shows a complex relationship with the REE, and doesn't show a correlation with any other elements, as it shows either a negative correlation or a positive correlation depending on the sample (Fig. 4.36). All REE and Y covary and are positively correlated (Fig. 4.37). Amongst the REE, La and Yb display the most scatter (Fig. 38). There is considerable intra-crystal variability in La/Yb (2 to 400). In W-related fluorite, La/Yb fluctuates, but not significantly (Fig. 4.39). In Sn-related fluorite I, La/Yb fluctuates significantly from zone to zone, with a low of ~ 0.5 followed by a high of ~ 300 , and low La/Yb is correlated to the sporadic dissolution features in some crystals (Fig. 4.40). La/Yb ranges from approximately 2 to 50 in Sn-related fluorite II, but shows no consistent relationship related to dissolution features. There is a strong negative correlation between La/Yb and total REE (Fig. 4.41).

4.3.1 Intracrystal Variability

In general, Fe, Cu, Zn, Rb, Sr, Mo, and Pb all covary across a crystal and are present in high concentrations where REE concentrations are low (Fig. 4.42). Some W-related samples exhibit distinct covariation among Fe, Cu, Zn, Rb, Sr, Mo, and Pb (Fig. 4.43), but other samples do not and are more difficult to interpret (Fig. 4.44). In one W-related fluorite crystal (Fig. 4.43), Fe, Cu, Zn, Rb, Sr, and Pb are high in concentration in all zones except for Zone 2 and Zone 4. Molybdenum behaves similarly with the exception that it is also low in concentration in Zone 9. Although W does not correlate with Fe, Cu, Zn, Rb, Sr, Mo, and Pb, it does share the same relative relationship these elements show with the REE. In zones where W concentrations are high, REE concentrations are low (Fig. 4.45). This relationship is especially evident in the W-related fluorite crystals that are characterized by dark-CL and abundant mineral inclusions, where the high concentrations of REE occur in the dark-CL, mineral inclusion-rich zones (Fig. 4.46).

In Sn-related fluorite I, the concentrations of Fe, Cu, Zn, Rb, and Sr are high throughout the crystal except in the growth zone that has abundant dissolution surfaces (i.e., Zone 6) and the REE mineral inclusion-rich rim (i.e., Zone 9), where the concentrations of these elements are low (Fig. 4.47). Molybdenum and Pb behave similarly throughout the crystal to the aforementioned elements, with the exception of Zone 8 where Mo is low in concentration and Zone 9 where Pb is high in concentration. The dissolution zone also contains high REE concentrations in addition to Zones 7 through 9, with Zone 9 having the highest REE concentrations (Fig. 4.48). Tungsten in Sn-related

fluorite I has similar characteristics to W-related fluorite in that W is low in concentration where REE concentrations are high (Fig. 4.48). Tungsten is also low in Zone 2 where REE concentrations are also low. Sn-related fluorite also shows a relationship between REE concentration and CL character, with higher REE concentrations correlating to darker CL character (Fig. 4.49).

In Sn-related fluorite II, Fe, Cu, Rb, Sr, and Pb are high in concentration in Zones 1, 2, and 5, but low in Zones 3 and 4 (Fig. 4.50). Zinc and Mo behave slightly differently as they are high in concentration in Zone 4 and low in concentration in Zone 5 (Fig. 4.50). Rare-earth elements behave the same as they do in the other types of fluorite in that they are low in concentration where Fe, Cu, Zn, Rb, Sr, Mo, and Pb are high in concentration (Fig. 4.51). Tungsten concentrations are low where REE concentrations are high (Fig. 4.52).

All of the fluorite types exhibit considerable intracrystal variability. In W-related fluorite the starkest difference in composition is between the bright-CL, planar zones and the dark-CL, mineral inclusion-rich zones. The dark-CL zones that have abundant REE mineral inclusions have higher concentrations of REE, Y, and Th, and lower concentrations of every other element than other zones (Fig. 4.53). The high concentrations of REE do not seem to reflect the presence of REE-mineral inclusions based on the uniformity of the laser ablation spectra (Fig. 5.54). The bright-CL rim on Mo-related fluorite (where mantled by molybdenite) exhibits higher concentrations of Mo and Bi and lower concentrations of REE compared to the rest of the crystal (Fig. 4.55). Even within homogenous crystals there is intracrystal variability in chemistry, but it can not be assessed in terms of growth of the crystal. Elements in stages 1, 2, 3, and 4 in Sn-related fluorite I behave in one of three ways: they can progressively increase or decrease with crystal growth (time), or show a more complex behavior. Iron, Cu, Zn, Rb, Sr, Mo, and Cs decrease in concentration systematically from Stage 1 to Stage 4 (Fig. 4.56). Arsenic, W, REE, Y, and Th increase in concentration systematically from Stage 1 to Stage 4 (Fig. 4.57). Lead, Bi, and U decrease in concentration from Stage 1 to Stage 3 and then increase in concentration in Stage 4 (Fig. 4.58). In Sn-related fluorite II, regardless of textural complexity, different stages of fluorite have very similar compositions (Figs. 4.26, 4.59).

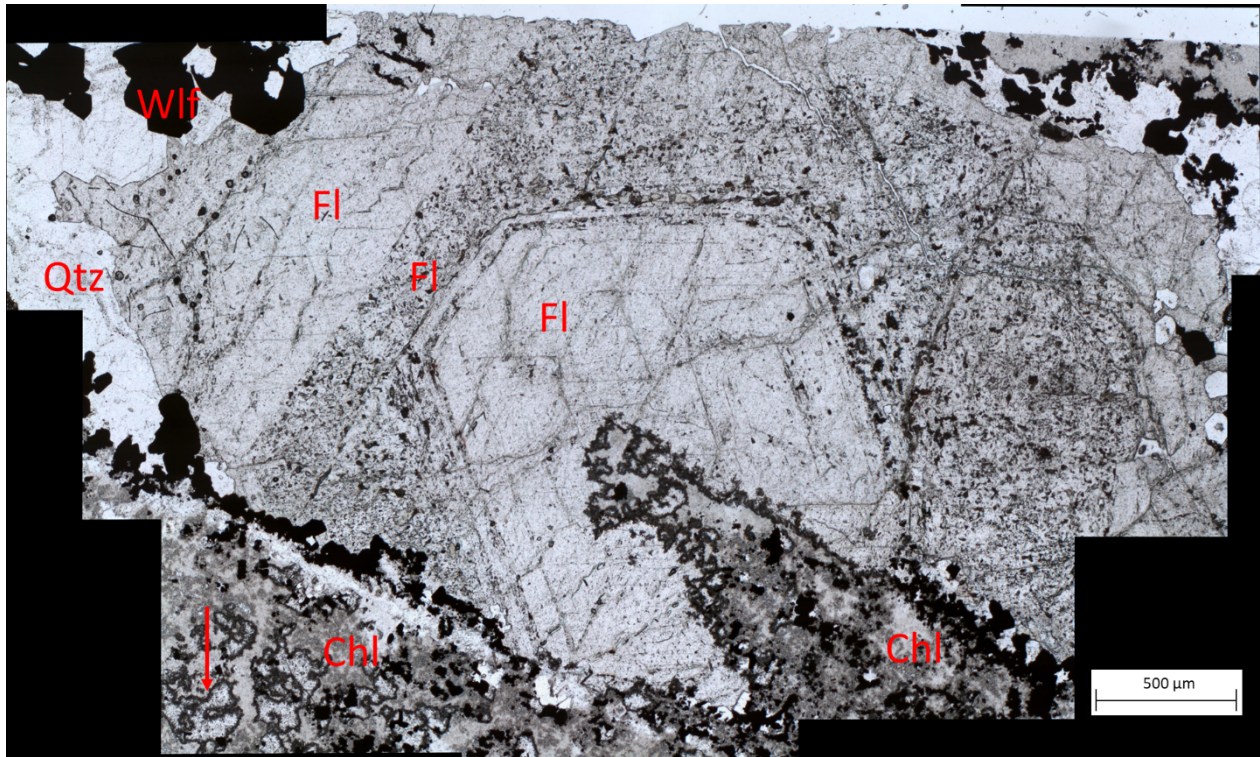


Figure 4.1 Plane-polarized light (PPL) image of W-related fluorite, wolframite, chlorite, and quartz. The red arrow points to acicular topaz crystals in a vug with fluorite.

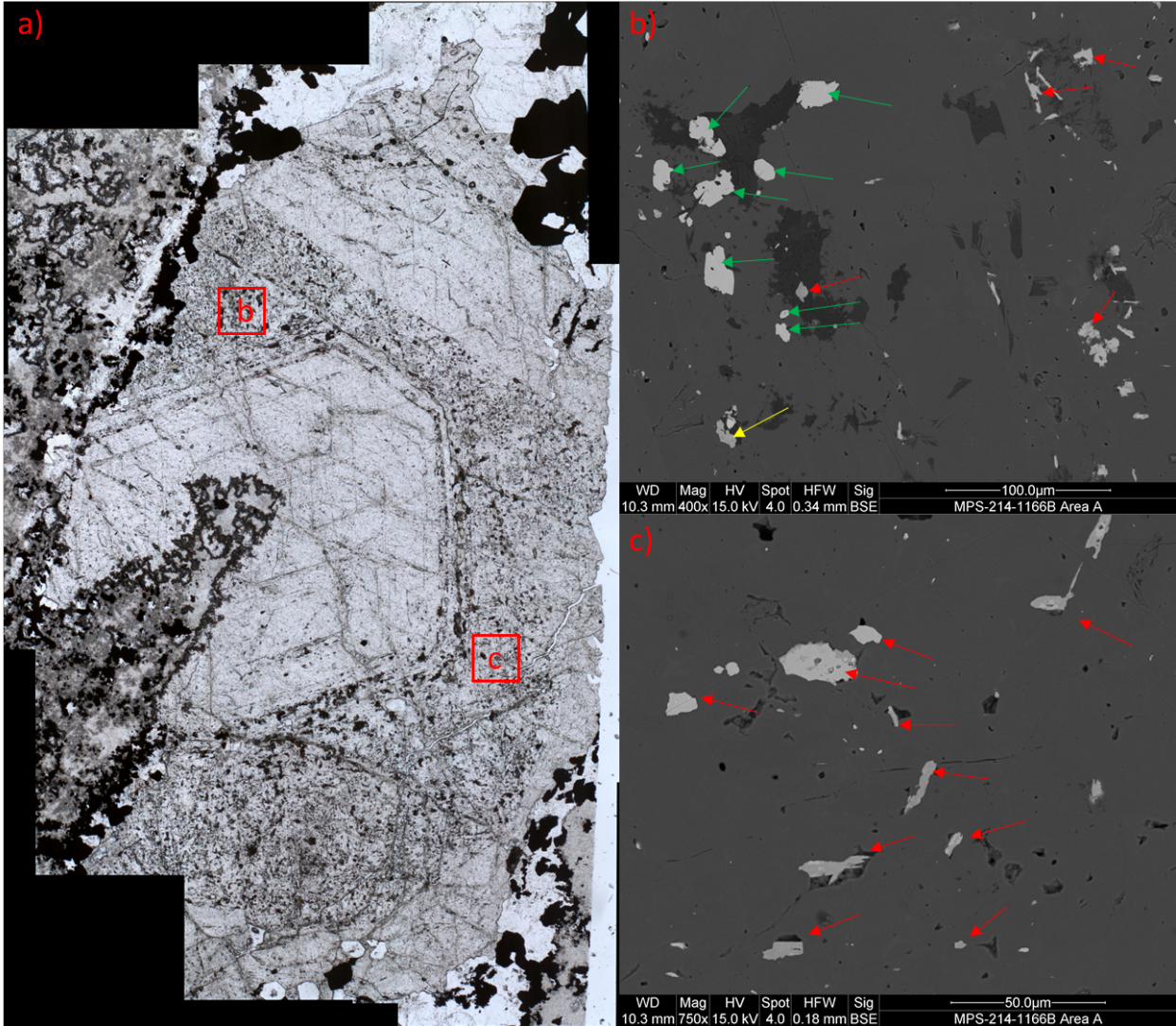


Figure 4.2 (a) PPL image of W-related fluorite (b) and (c) BSE images showing numerous wolframite (green arrows), monazite (yellow arrow) and REE-fluorocarbonate (red arrows) inclusions within the fluorite

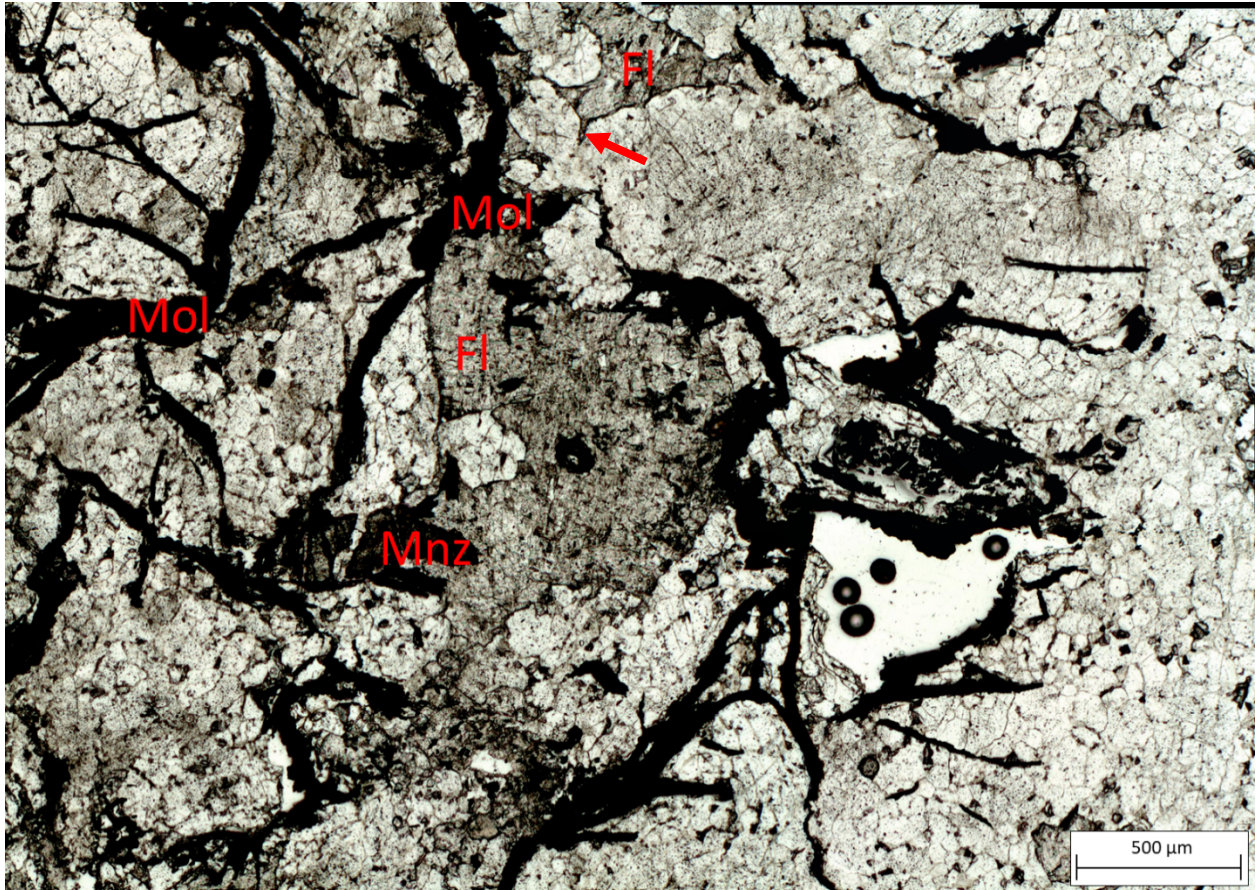


Figure 4.3 PPL image of Mo-related fluorite within an assemblage of fluorite + molybdenite + quartz + monazite. Red arrow denotes where fluorite is interstitial to quartz.

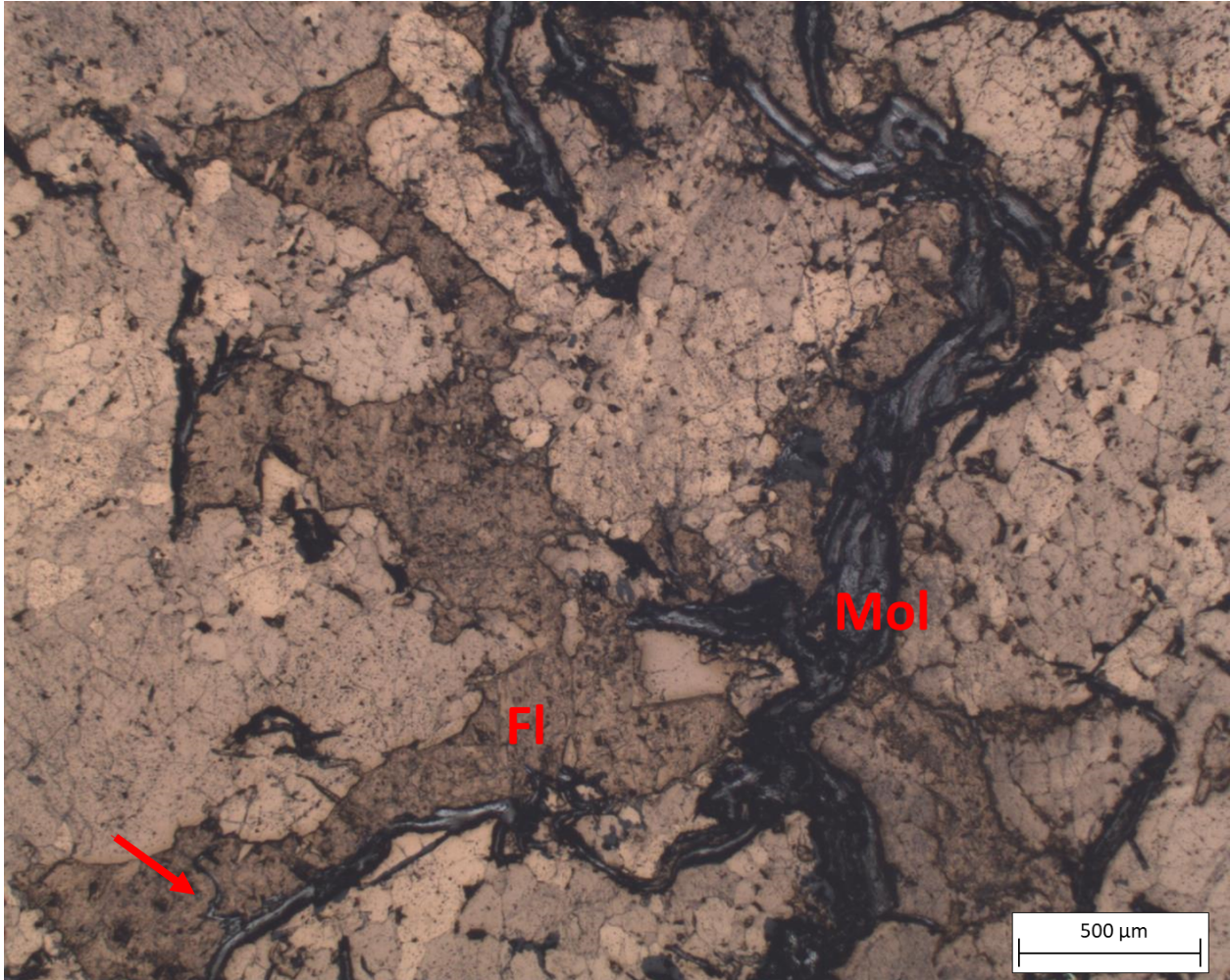


Figure 4.4 Combined PPL + Reflected light image of Mo-related fluorite, molybdenite, and quartz illustrating how molybdenite mantles fluorite. Red arrow denoting where molybdenite is present within a fracture in fluorite.

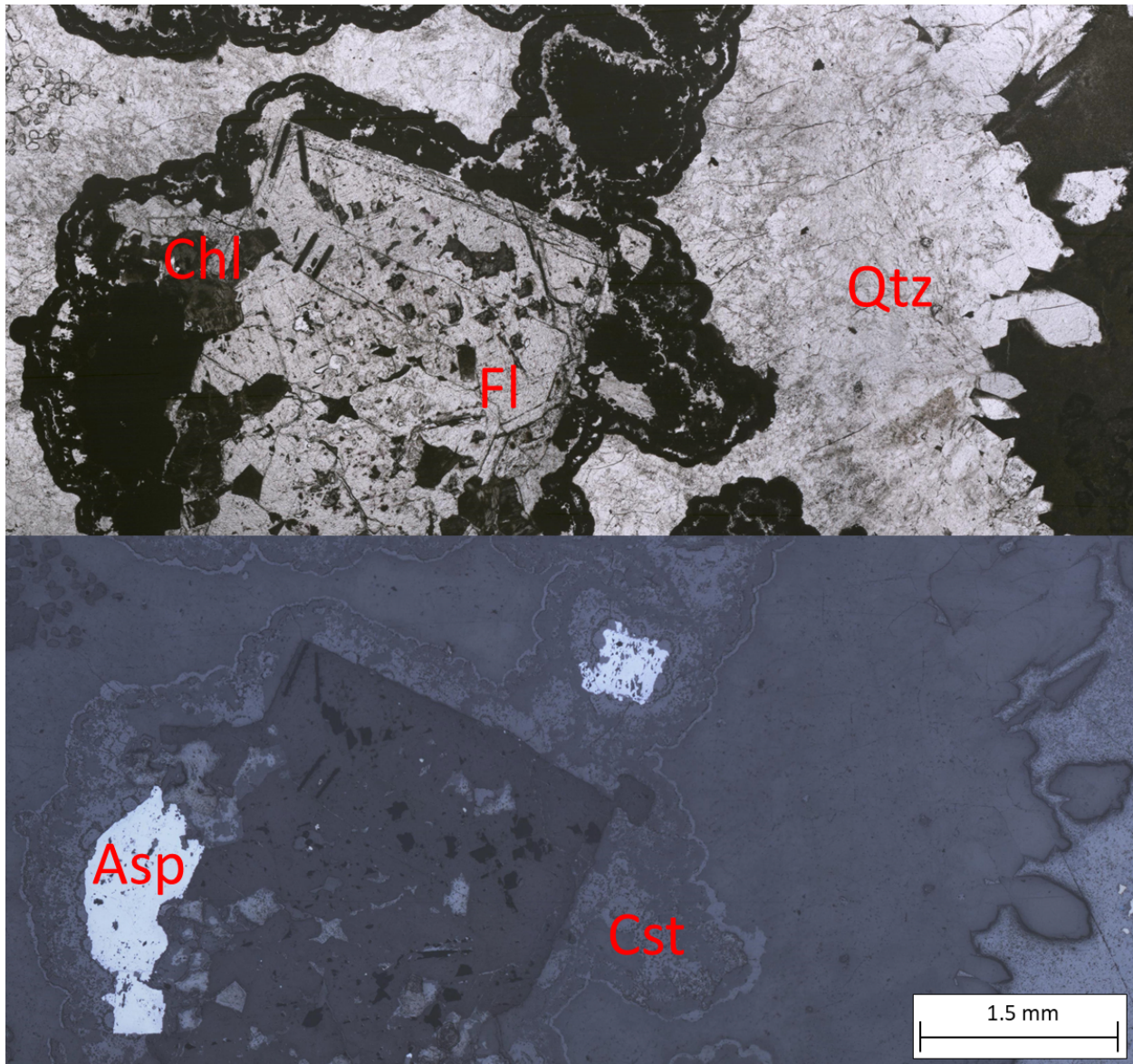


Figure 4.5 PPL and reflected light (RL) image of Sn-related fluorite I in an assemblage comprising fluorite + chlorite + arsenopyrite + cassiterite + quartz.

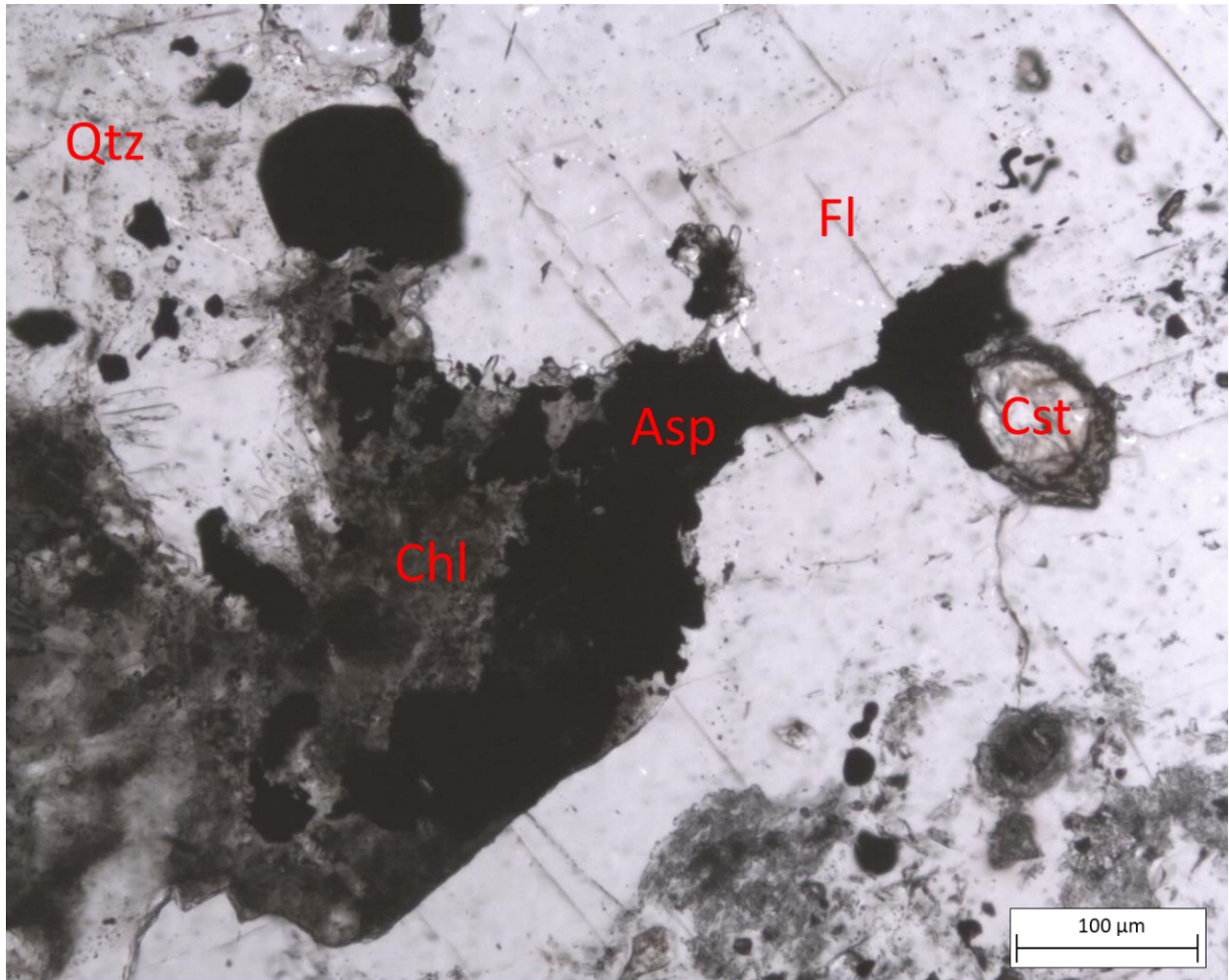


Figure 4.6 PPL image of a vein in earlier Sn-related fluorite I containing chlorite, arsenopyrite, and cassiterite.

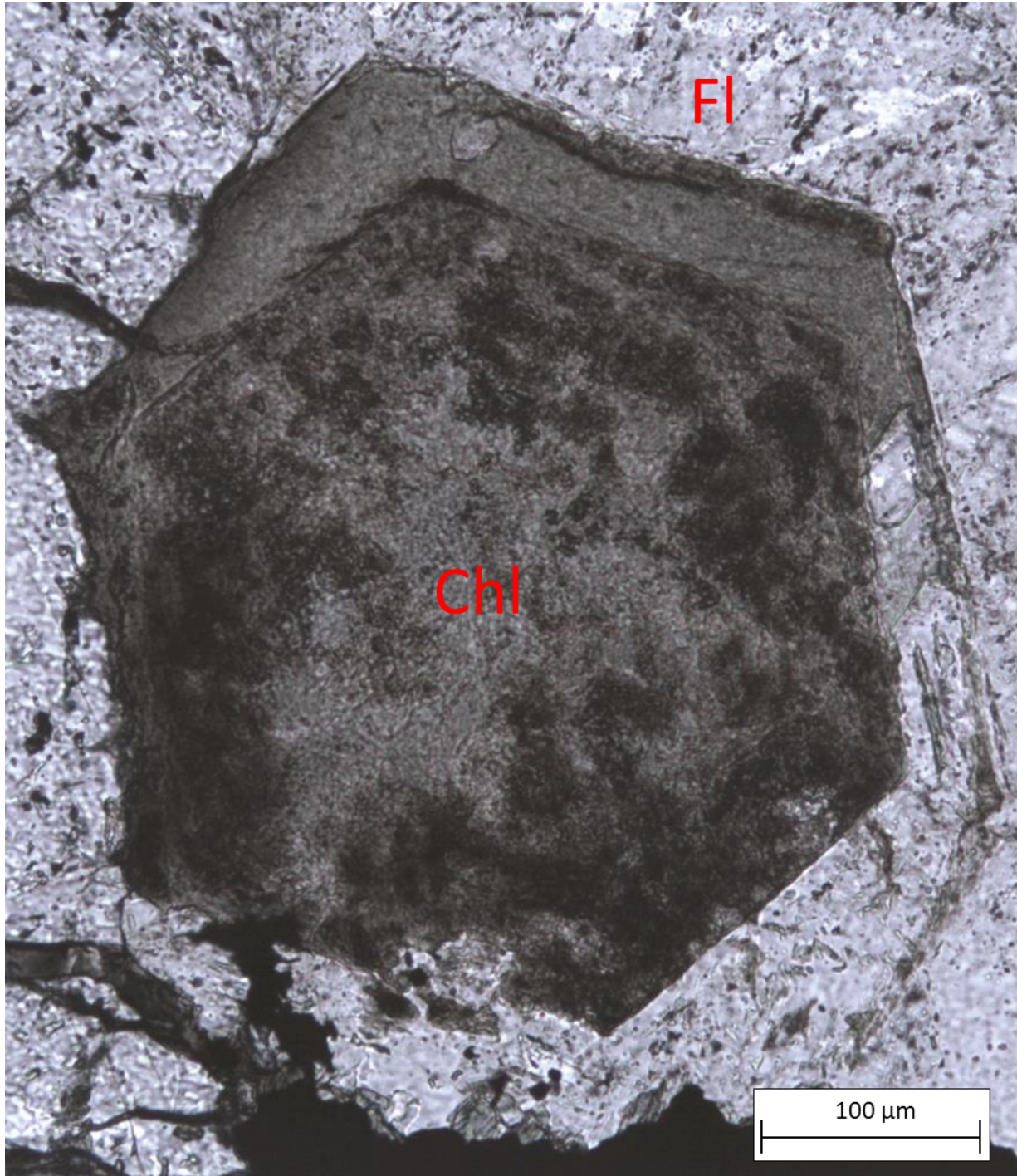


Figure 4.7 PPL image of a hexagonal chlorite-rich pseudomorph that is interpreted to have replaced biotite.

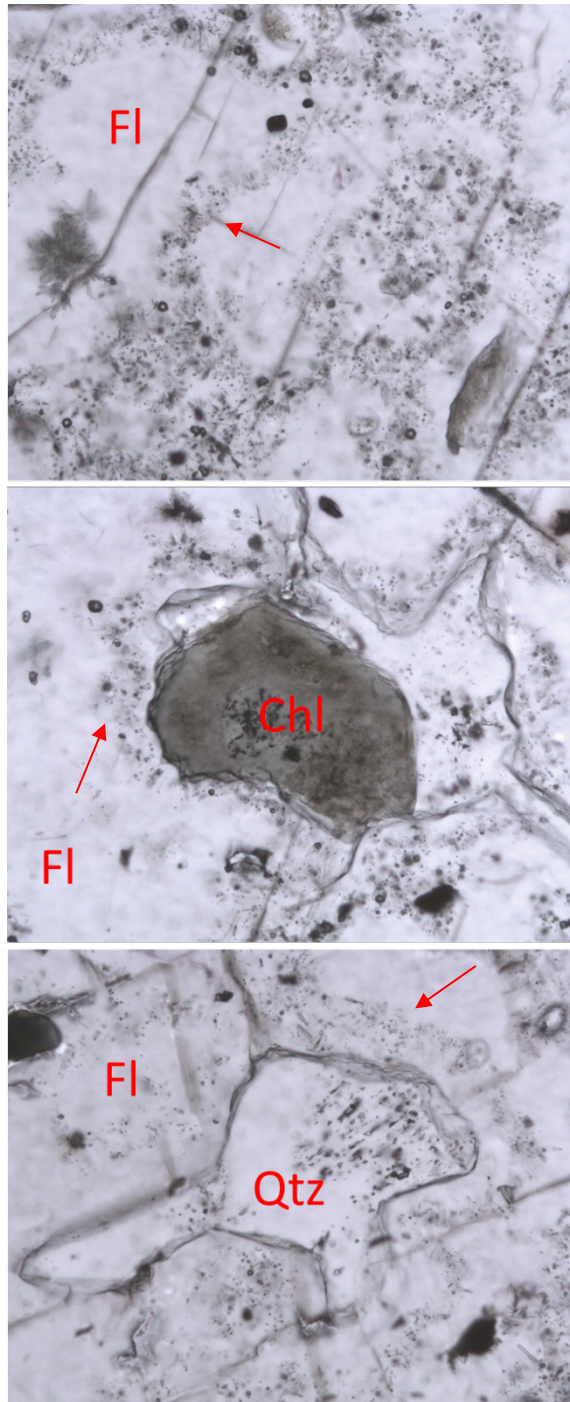


Figure 4.8 PPL image of topaz crystals (red arrows) within earlier Sn-related fluorite I and radiating out from quartz and chlorite grains.

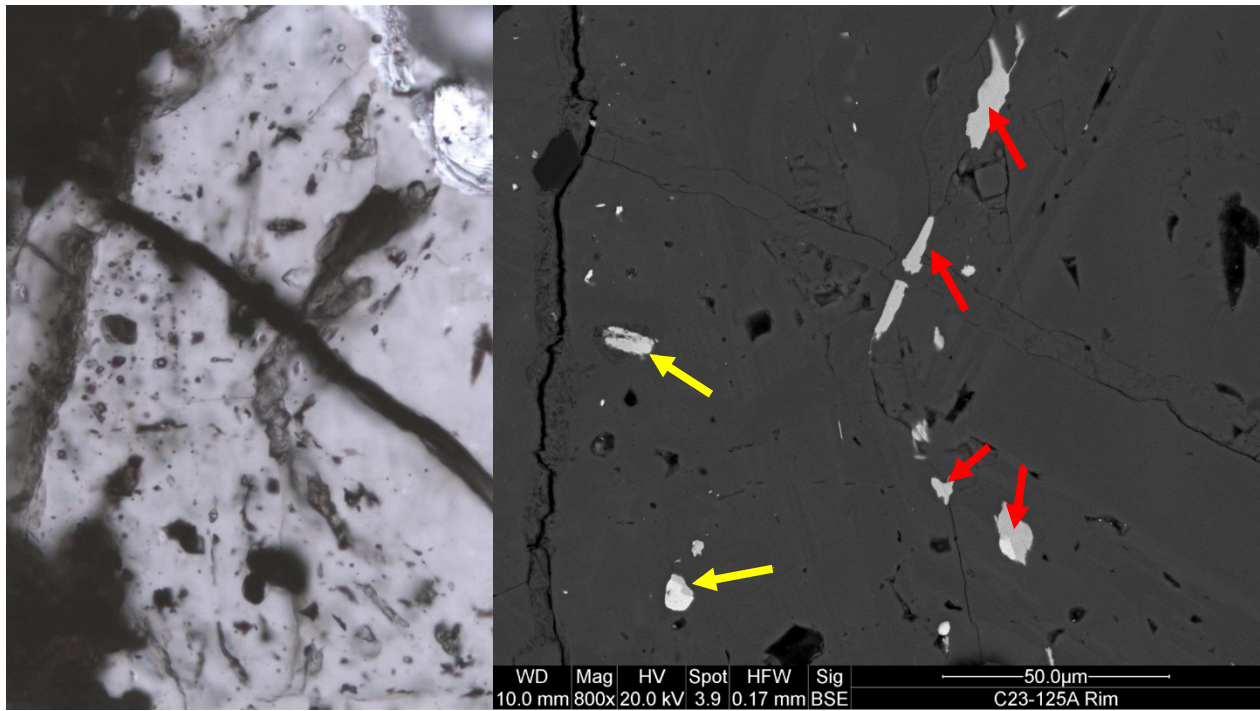


Figure 4.9 PPL and BSE images illustrating the mineral inclusions in the rim of Stage 4, Sn-related fluorite I: REE-fluorocarbonates (red arrows) and monazite (yellow arrows).

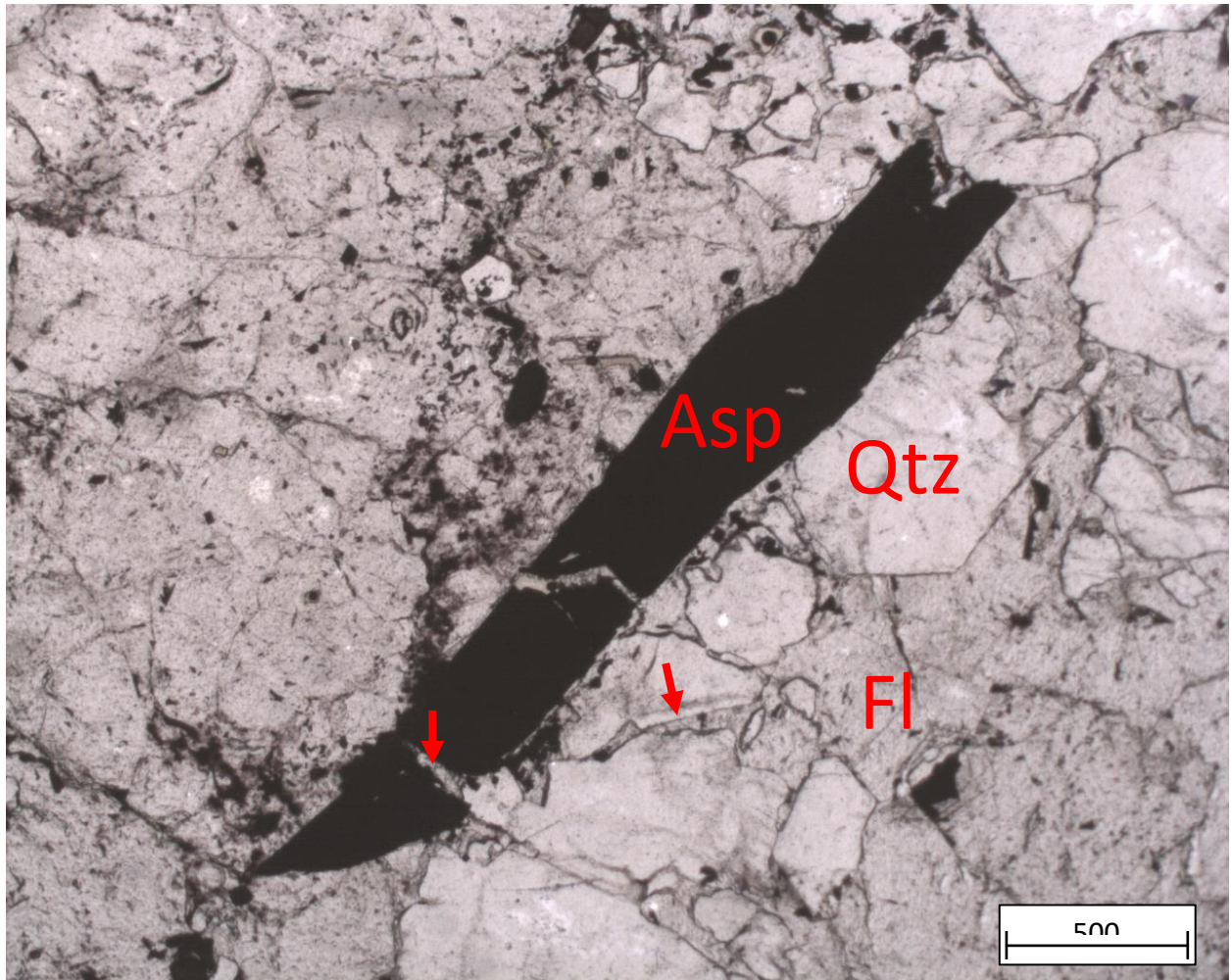


Figure 4.10 PPL image of Sn-related fluorite II crosscutting arsenopyrite and quartz (red arrows).

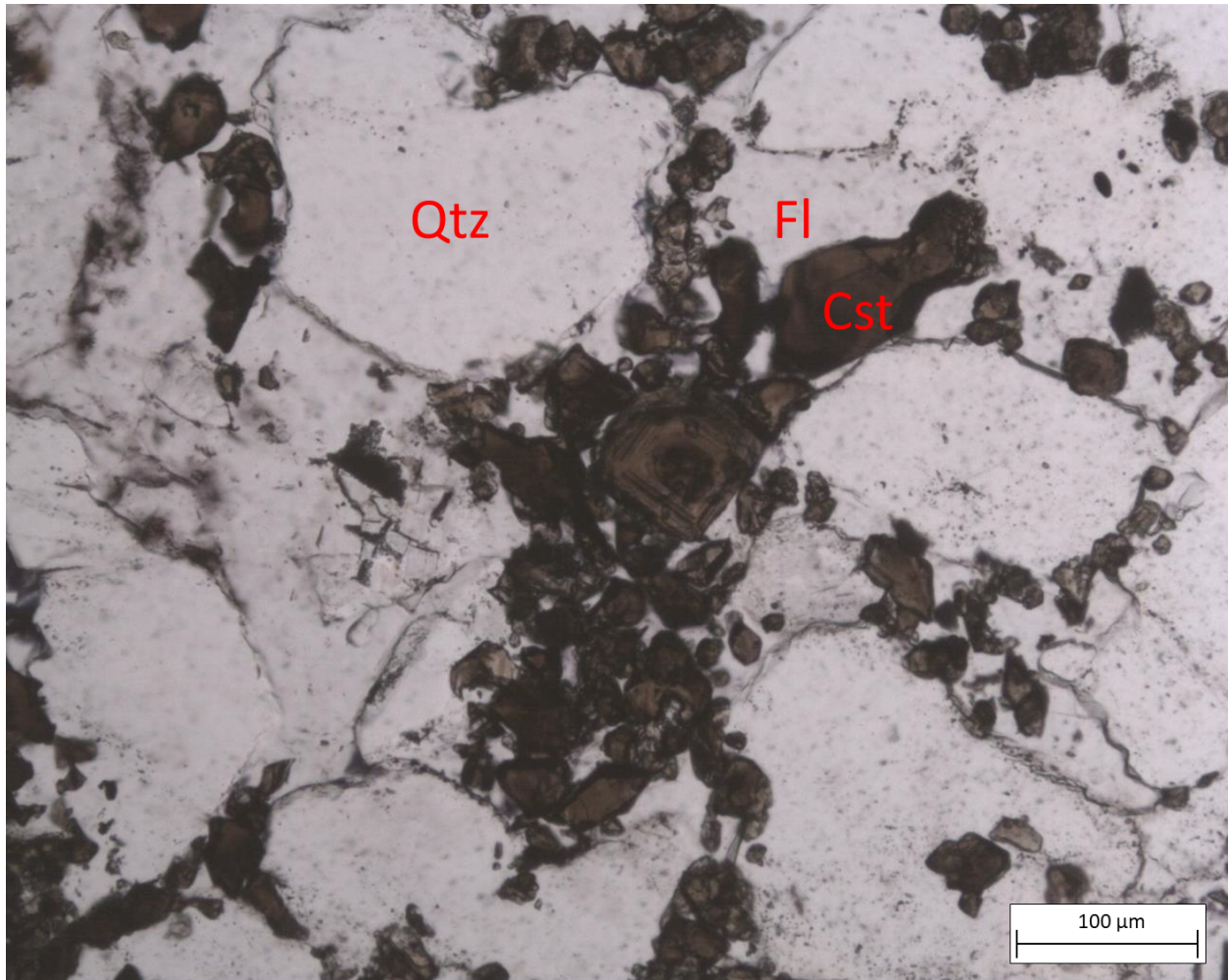


Figure 4.11 PPL image of cassiterite in Sn-related fluorite II.

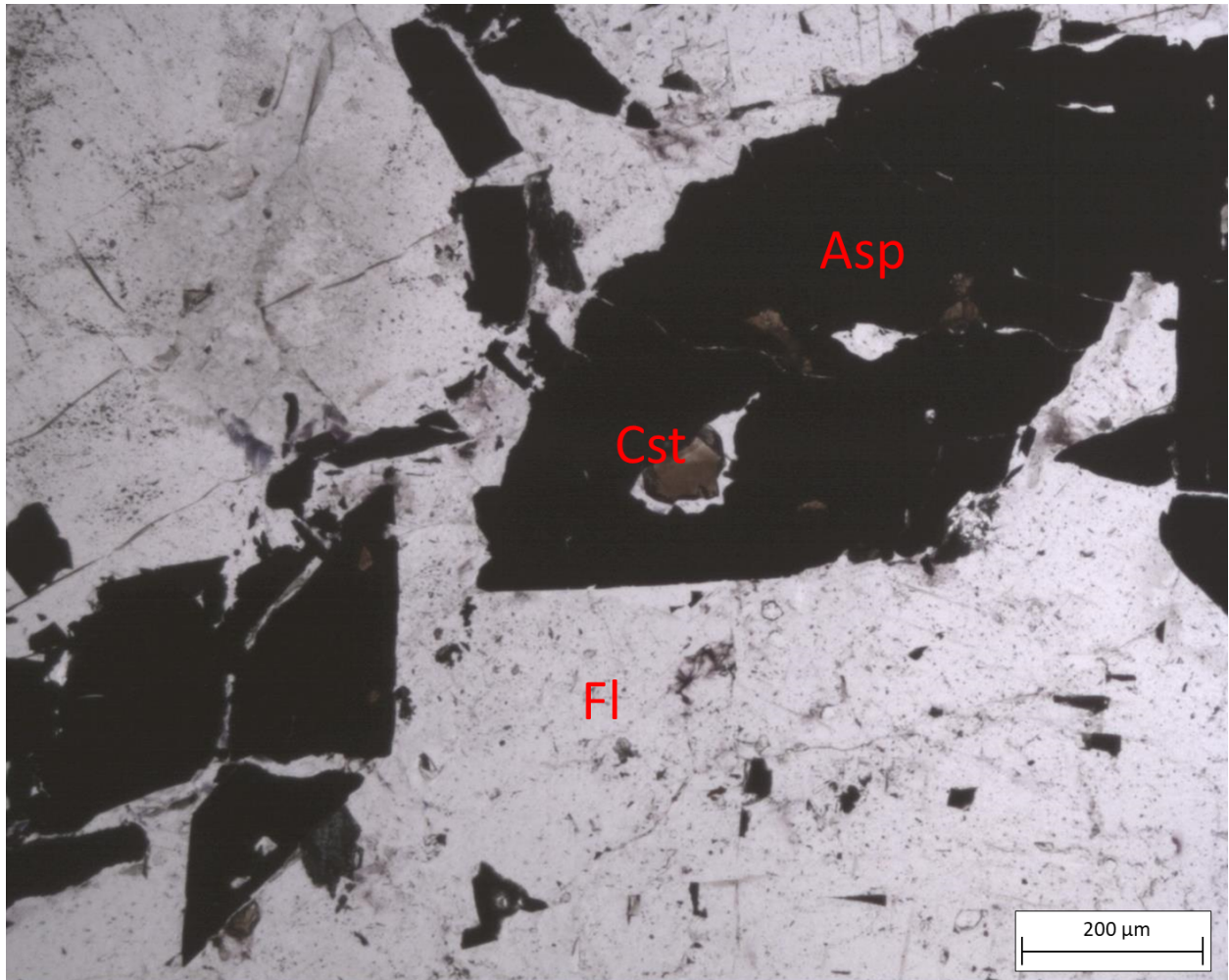


Figure 4.12 PPL image of cassiterite that has precipitated into open space within arsenopyrite grains.

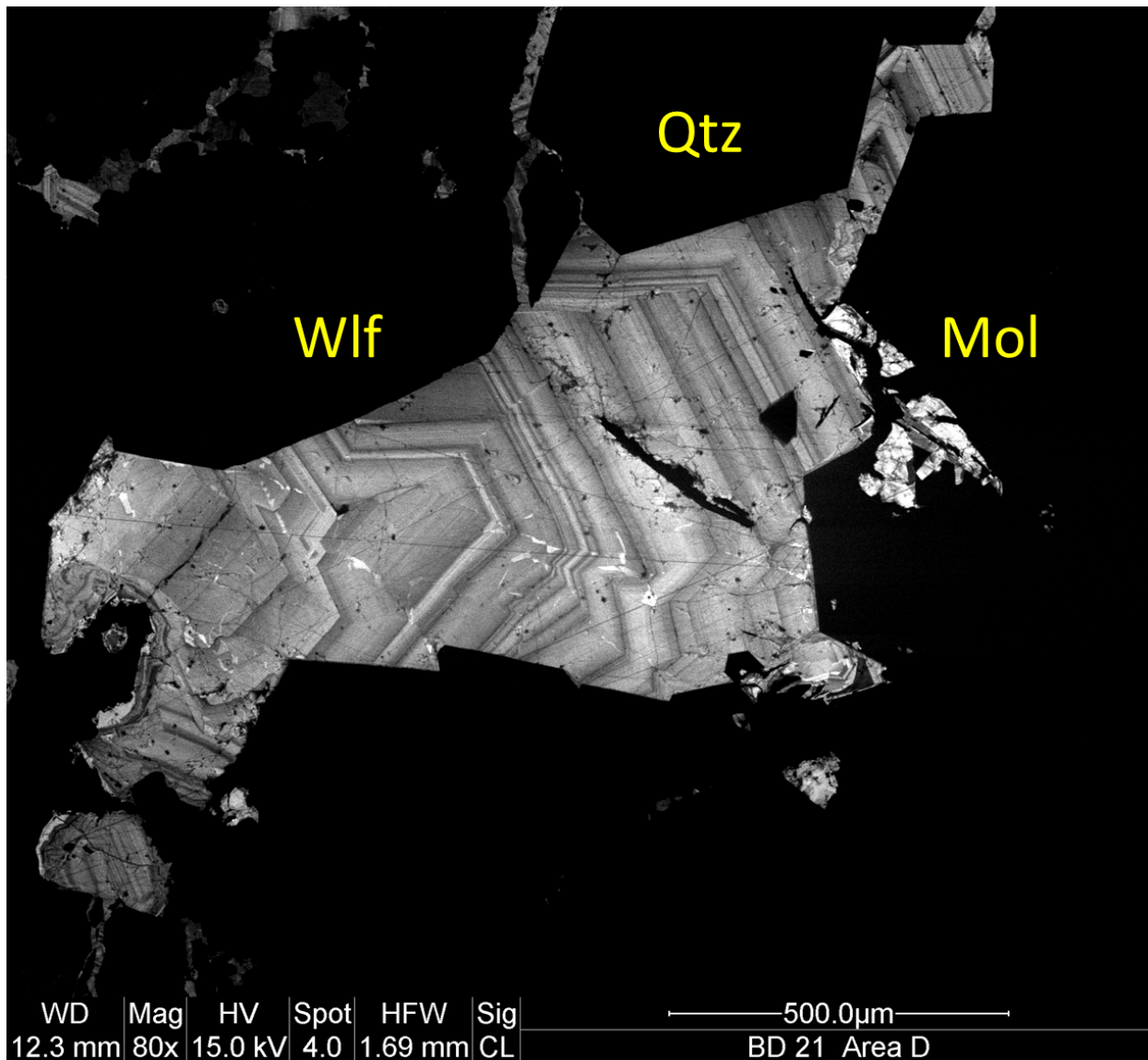


Figure 4.13 CL image of W-related fluorite showing simple planar zoning with alternating bright and dark CL zones.

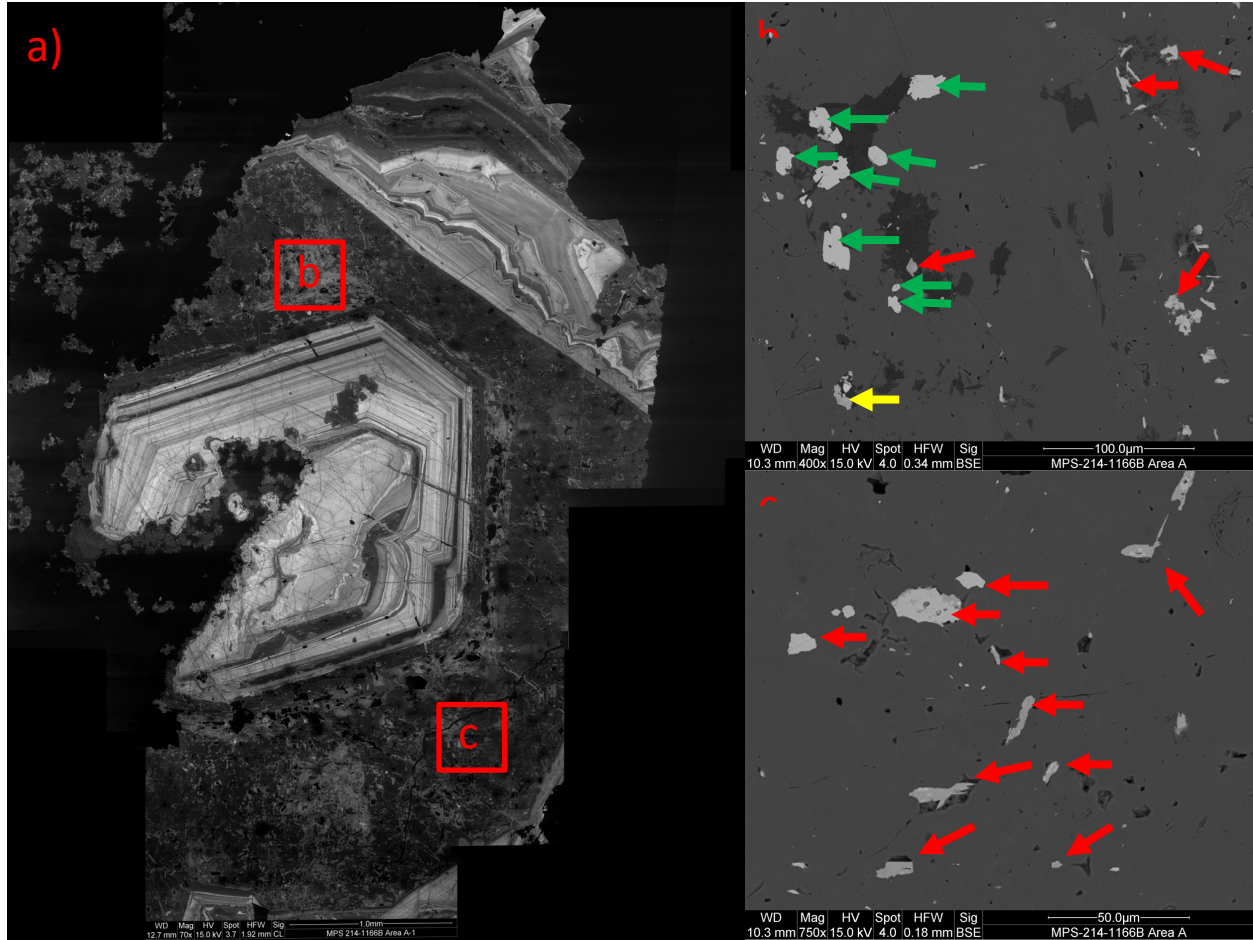


Figure 4.14 CL image of W-related fluorite showing a planar zoned crystal with a prominent, darker CL zone filled with numerous wolframite (green arrows), REE-fluorocarbonates (red arrows), and monazite (gold arrow) inclusions.

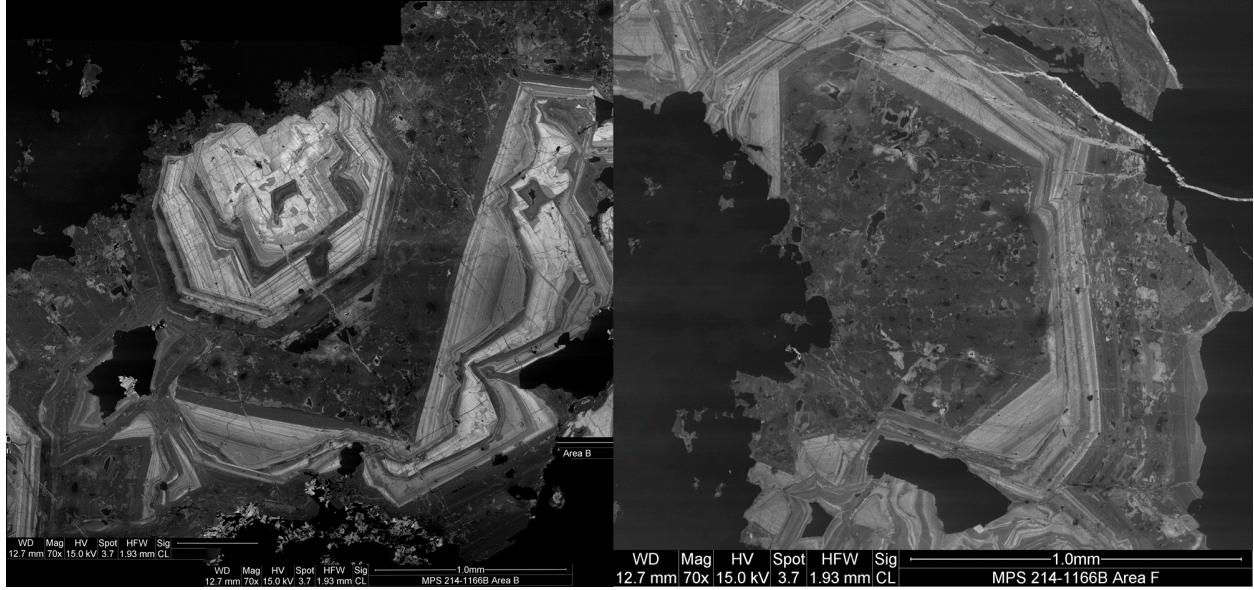


Figure 4.15 CL images of W-related fluorite illustrating that the prominent, darker CL zone with abundant mineral inclusions occurs between planar zones, within the core of a crystal, and as a rim.

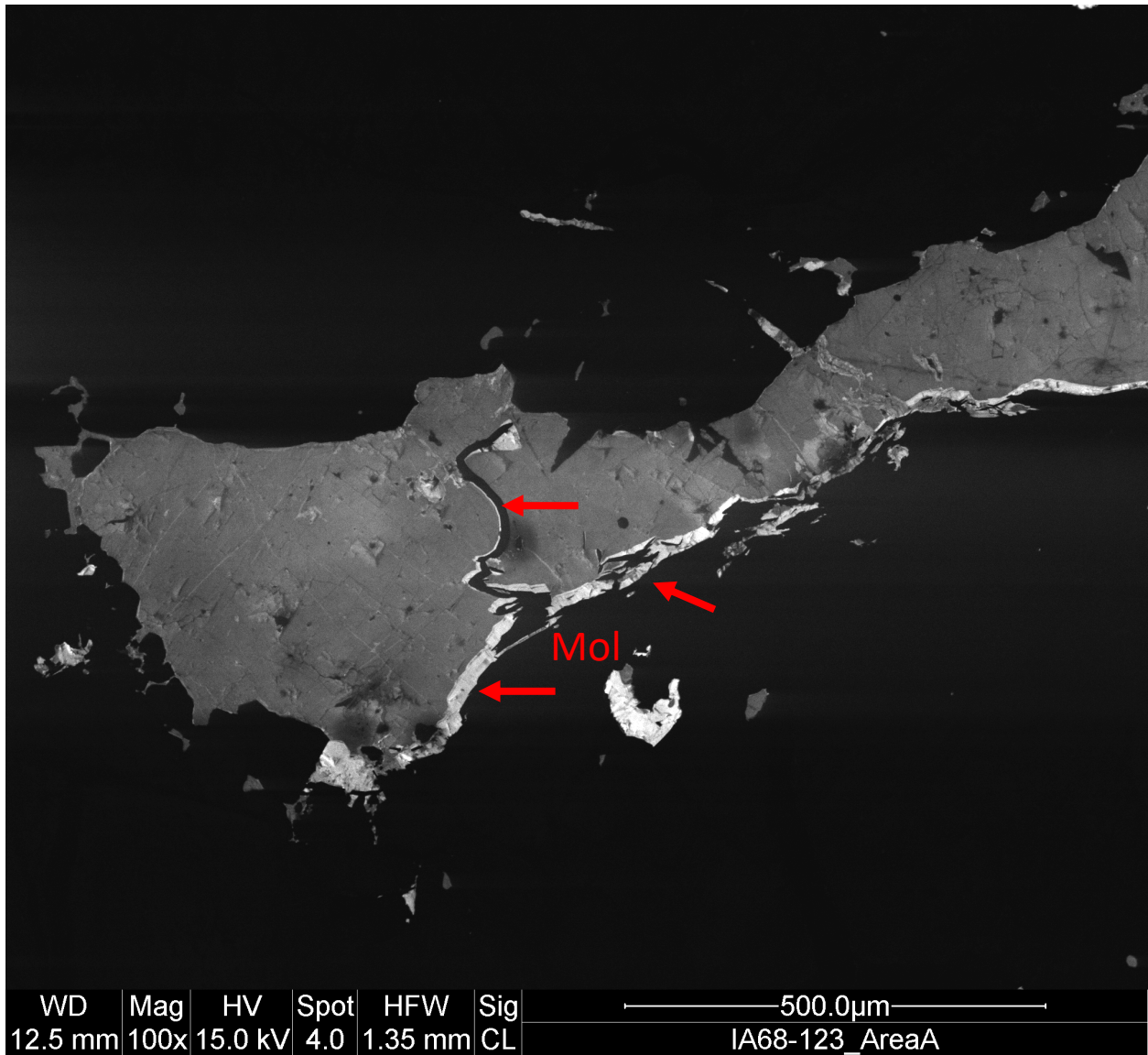


Figure 4.16 CL image of Mo-related fluorite showing a bright CL rim where mantled by molybdenite (red arrows).

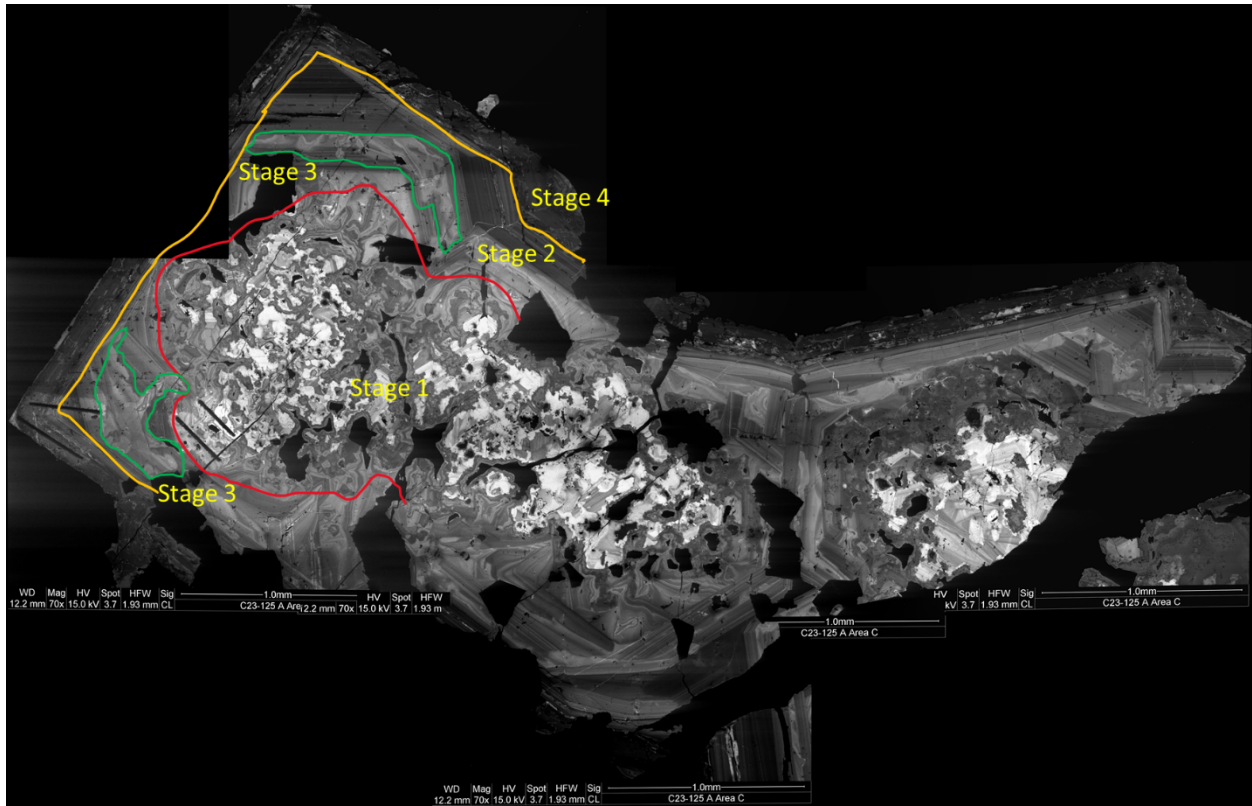


Figure 4. 17 CL image of Sn-related fluorite I showing a bright complex core, surrounded by planar zoning with sporadic dissolution features (Stage 3).

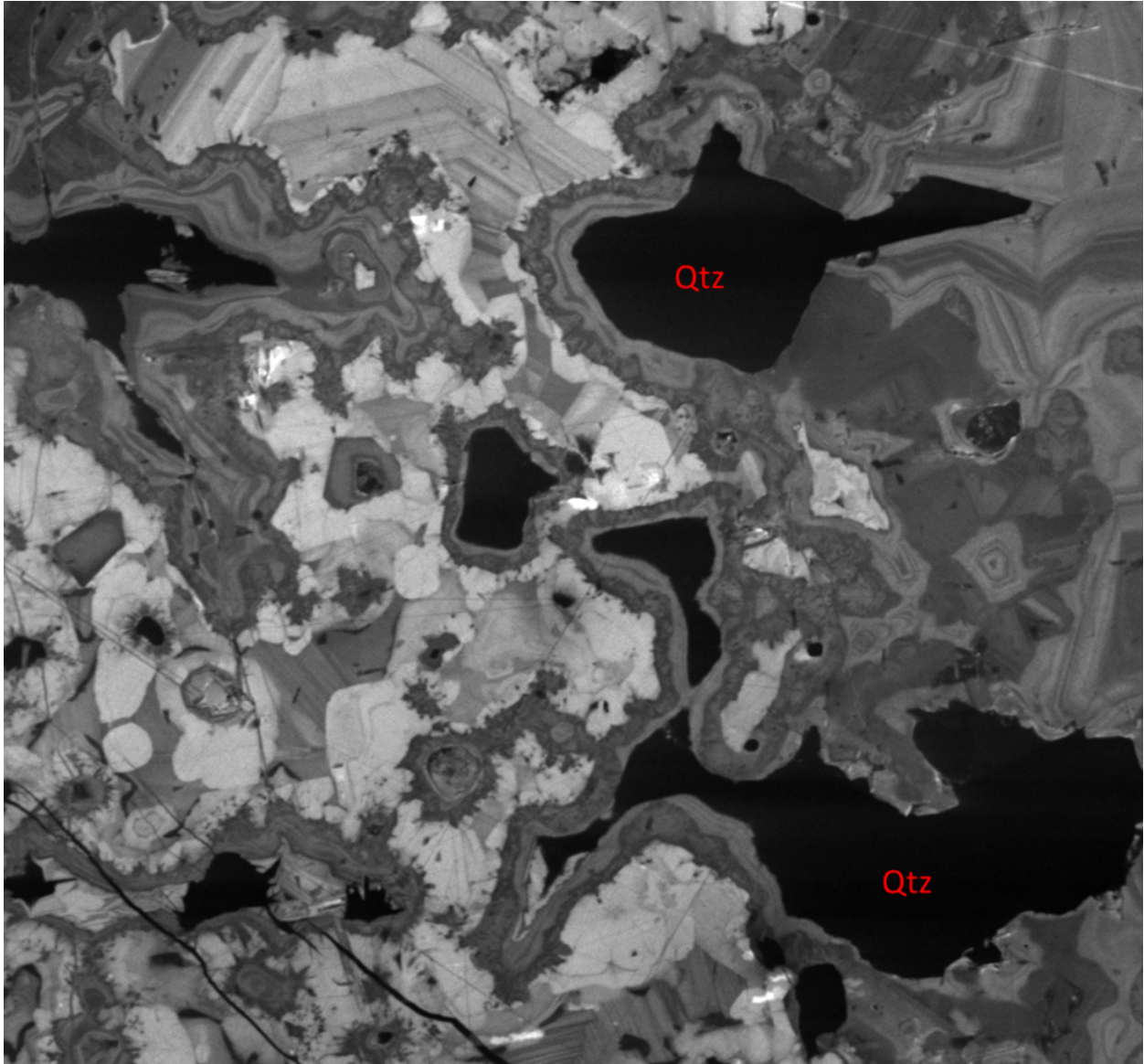


Figure 4.18 Stage 1 in Sn-related fluorite I with grains of quartz that are mantled by thin dark-CL zones of fluorite that contain acicular topaz crystals.

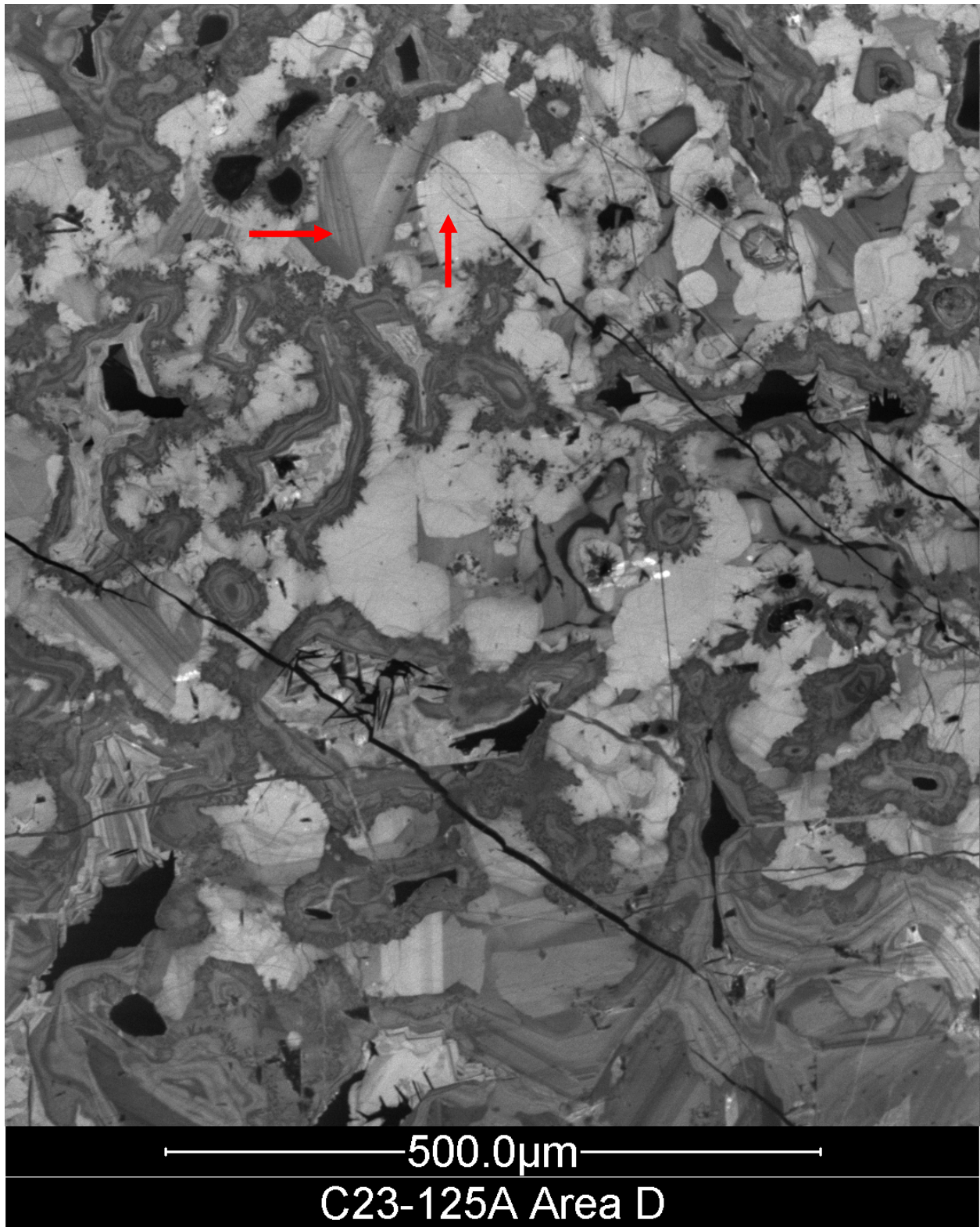


Figure 4.19 CL image within the core of Sn-related fluorite I depicting the two stages of bright-CL growth (red arrows).

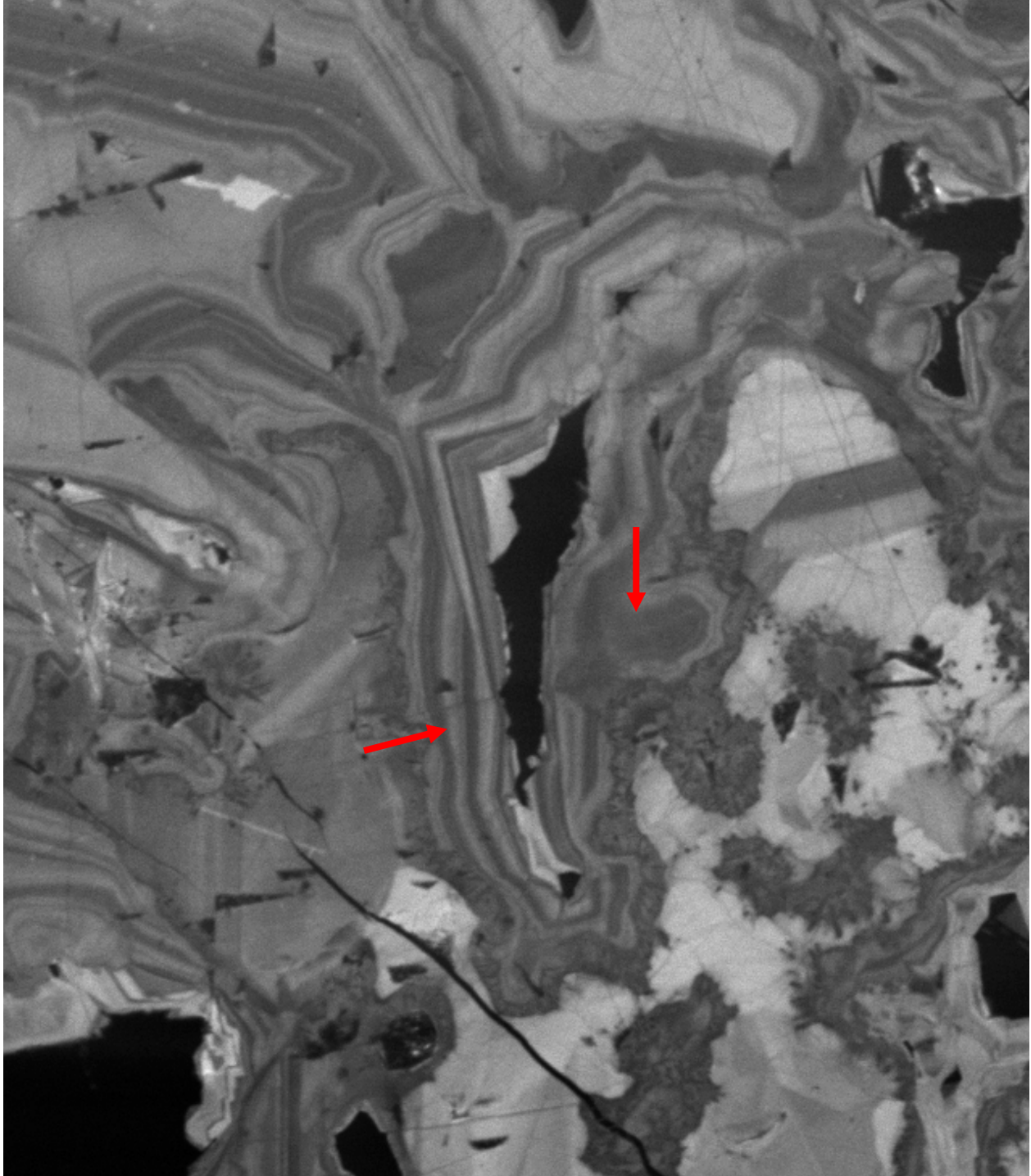


Figure 4.20 CL image with red arrows indicating where irregular dull zones mantle topaz-rich dark-CL zones in Sn-related fluorite I.



Figure 4.21 Red box denoting a dissolution feature in Sn-related fluorite I that has crosscut earlier growth zones.

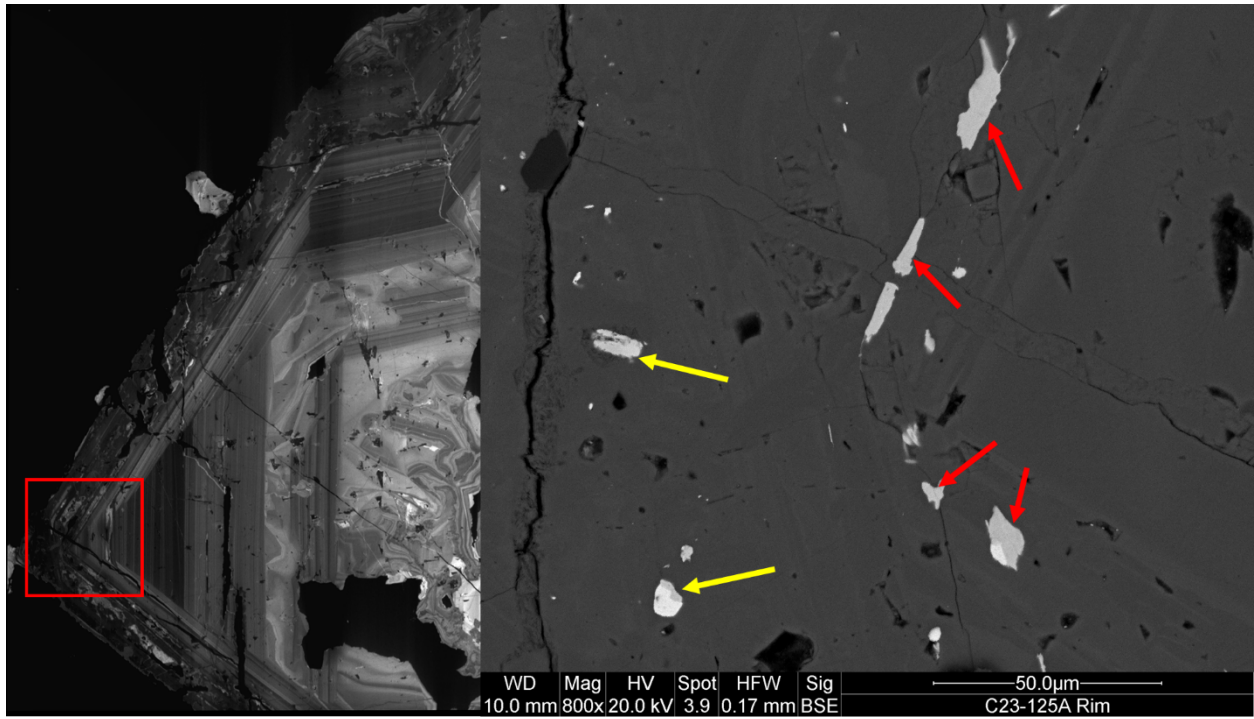


Figure 4.22 CL image of Sn-related fluorite I with REE-fluorocarbonate (red arrows) and monazite (yellow arrows) inclusions in the dark-CL rim.

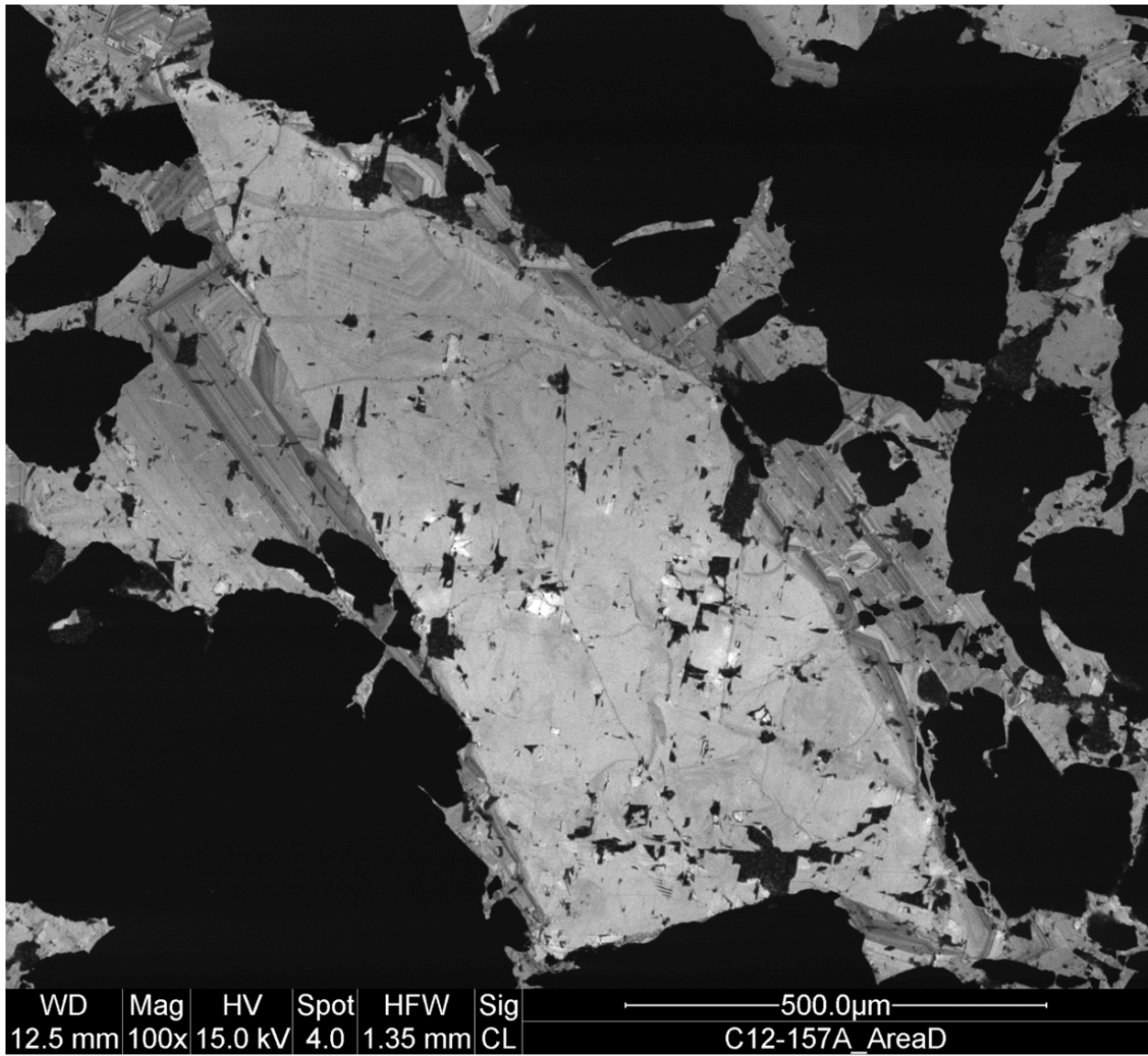


Figure 4.23 An uncommonly observed crystal of bright CL Sn-related fluorite II with planar growth zoning.

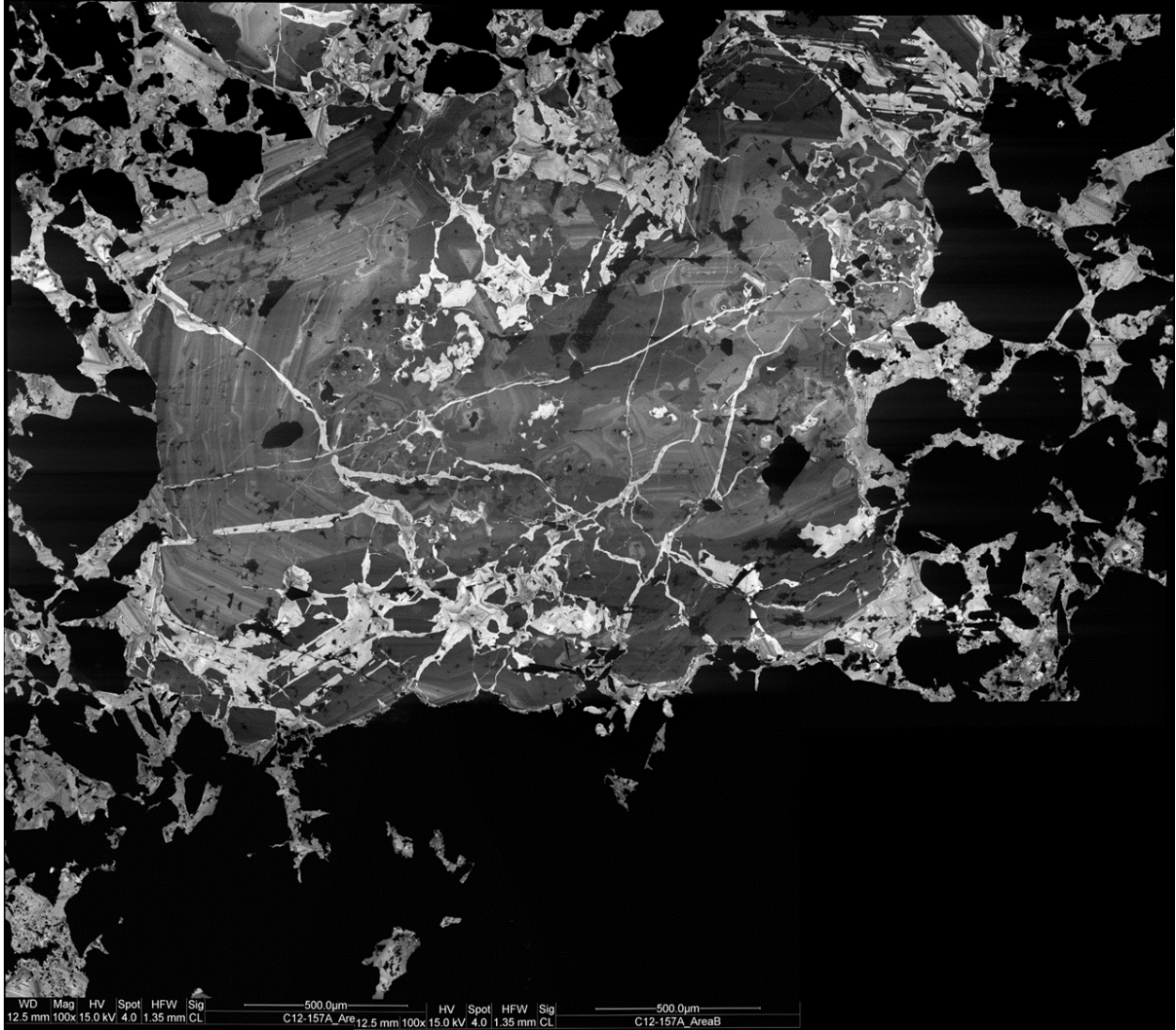


Figure 4.24 Dark-CL fluorite crystal of Sn-related fluorite II that has been dissolved, veined, and overgrown (e.g. bottom right) by later bright-CL fluorite.

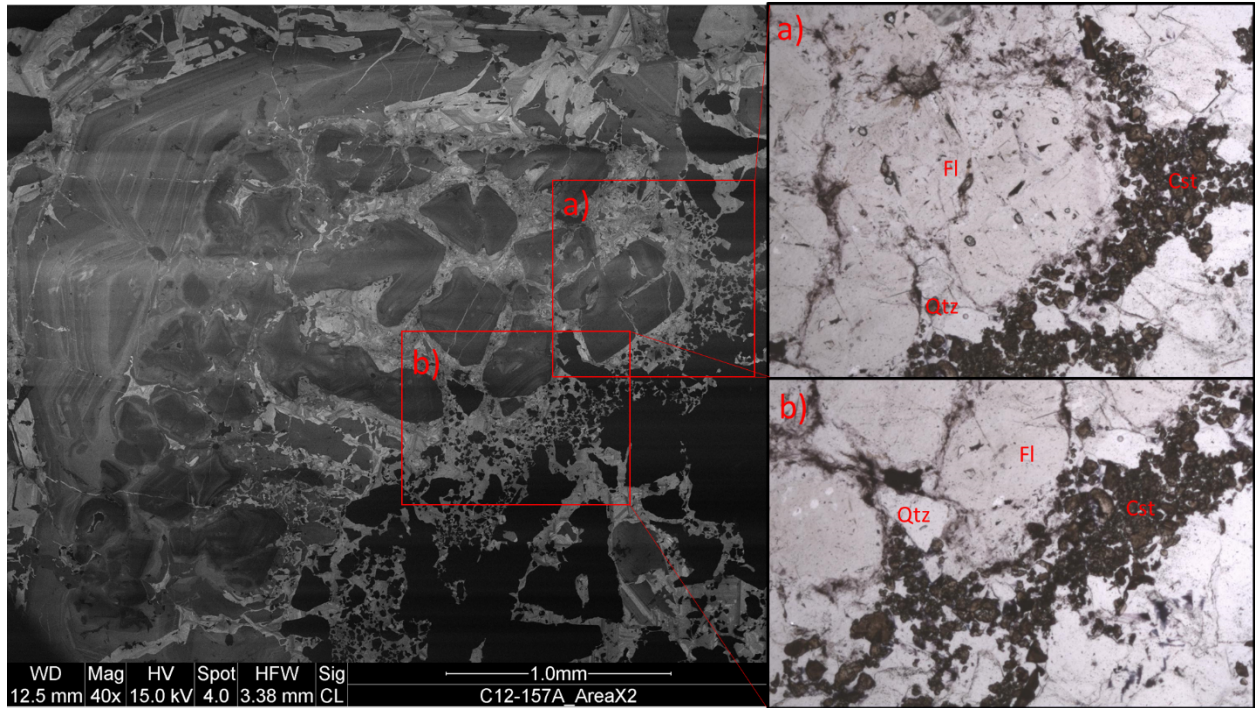


Figure 4.25 CL and PPL images showing the correlation between bright-CL dissolution features and cassiterite grains.

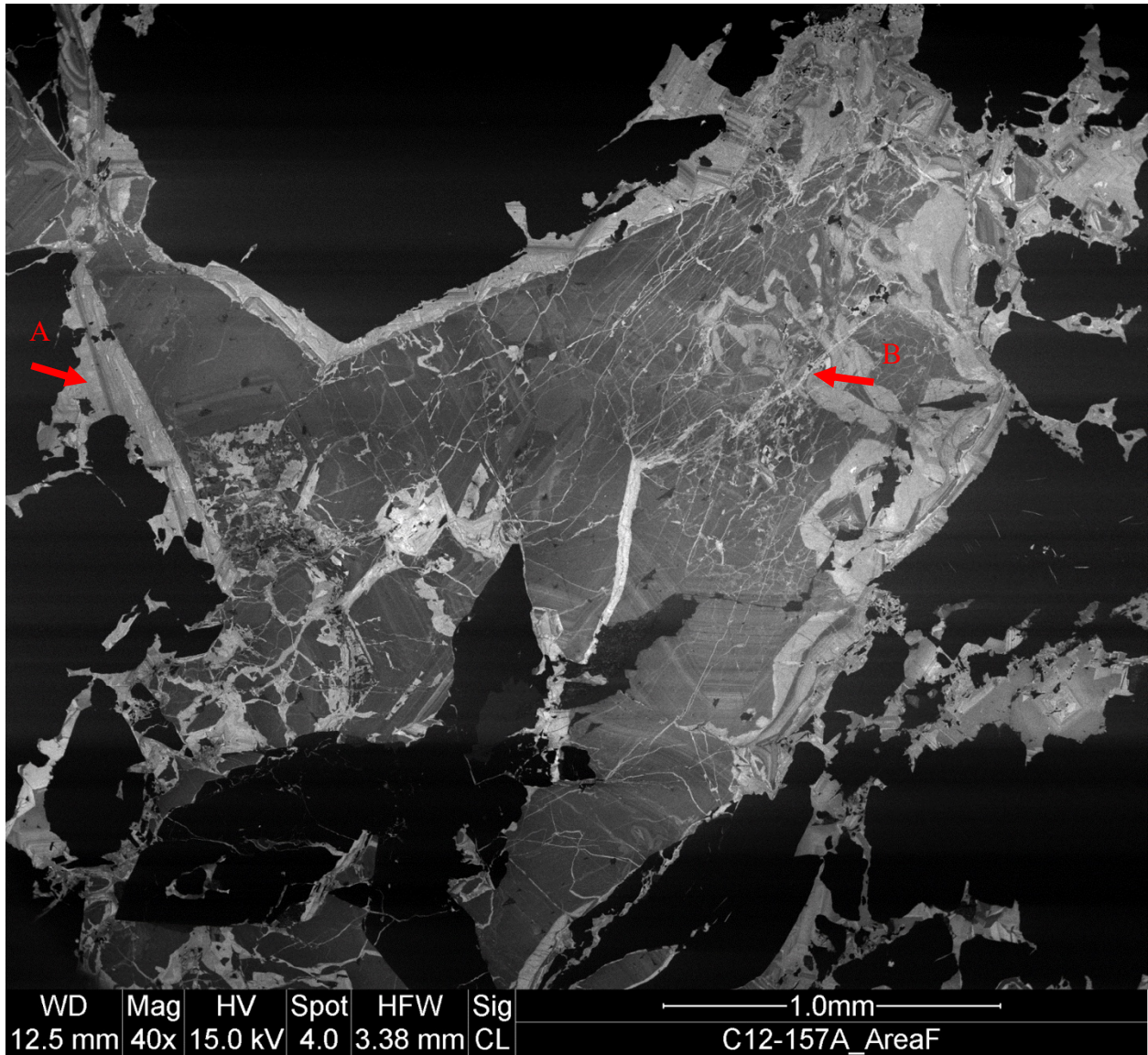


Figure 4.26 CL image of Sn-related fluorite II illustrating the two stages of bright CL fluorite that crosscuts dark CL fluorite. One stage of bright-CL fluorite has crosscut dark-CL fluorite as well precipitated as a rim around the crystal (red arrow “A”). A second stage of bright-CL fluorite has crosscut this earlier bright CL-fluorite (red arrow “B”).



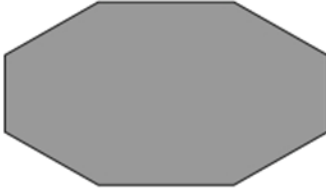
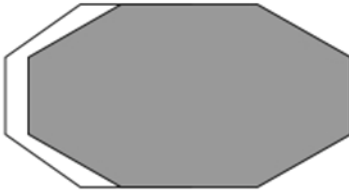
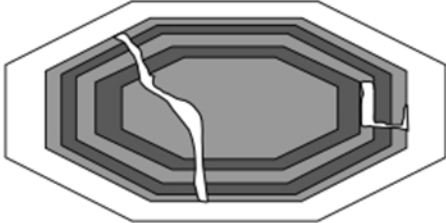

	Common CL Characteristics	Uncommon CL Characteristics
W-related fluorite		
Mo-related fluorite		
Sn-related fluorite		

Figure 4.27 Summary of CL characteristics exhibited by fluorite from Mount Pleasant. W-related fluorite commonly exhibits alternating bright and dark-CL, planar zones. Uncommonly, some W-related fluorite crystals exhibit a late replacement zone (black zone) that contains mineral inclusions (white diamond shapes) including REE-minerals, wolframite, hematite, and chlorite. Mo-related fluorite commonly exhibits no zoning, with the exception of where it is mantled by molybdenite. Sn-related fluorite commonly exhibits dull-CL planar zones, dissolution features, and later bright-CL fluorite. Uncommonly, Sn-related fluorite crystals exhibit complex bright-CL cores, dull-CL zones that are planar, sporadic dissolution features, and a late, dark-CL zone containing REE-mineral inclusions.

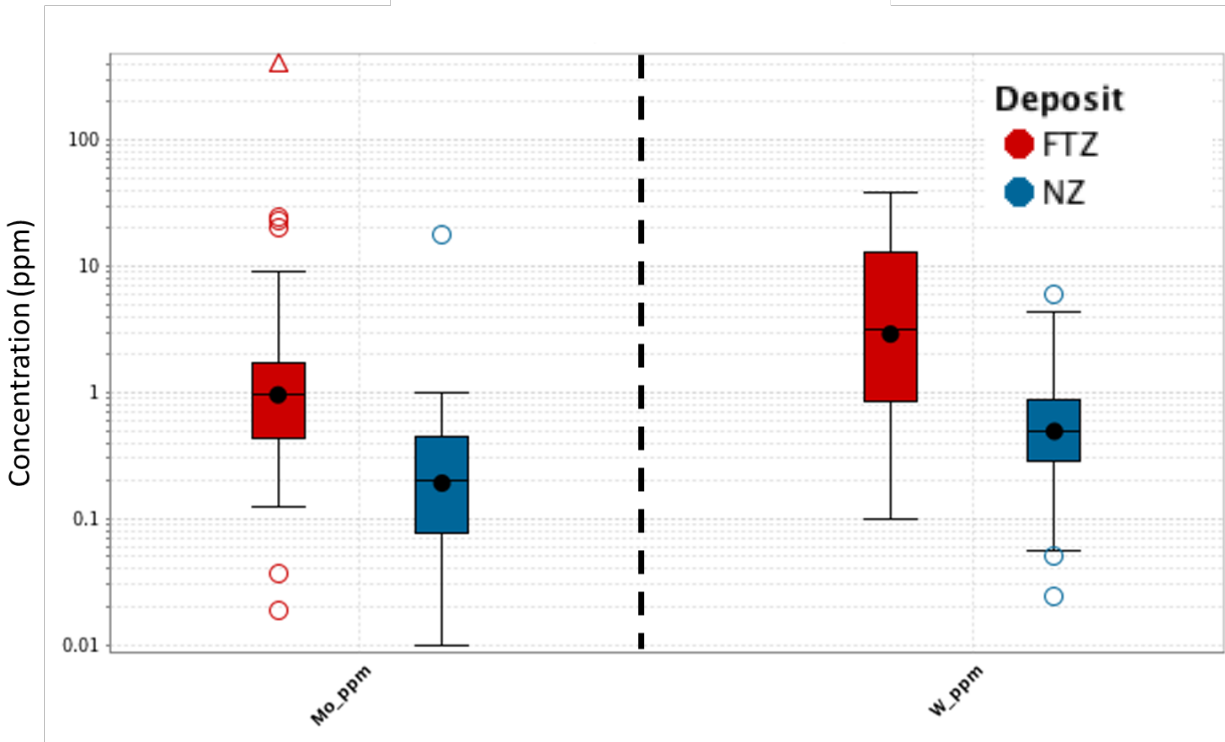


Figure 4.28 Box-whisker plot showing the concentration of Mo and W in fluorite from the FTZ and NZ. The whiskers represent the 10th and 90th percentile, the lower end and upper end of the box represent the 25th and 75th percentile, the line inside the box represents the median, the black circle represents the mean, and the open circles represent data below the 10th percentile and above the 90th percentile. All other box-whisker plots are constructed with the same parameters.

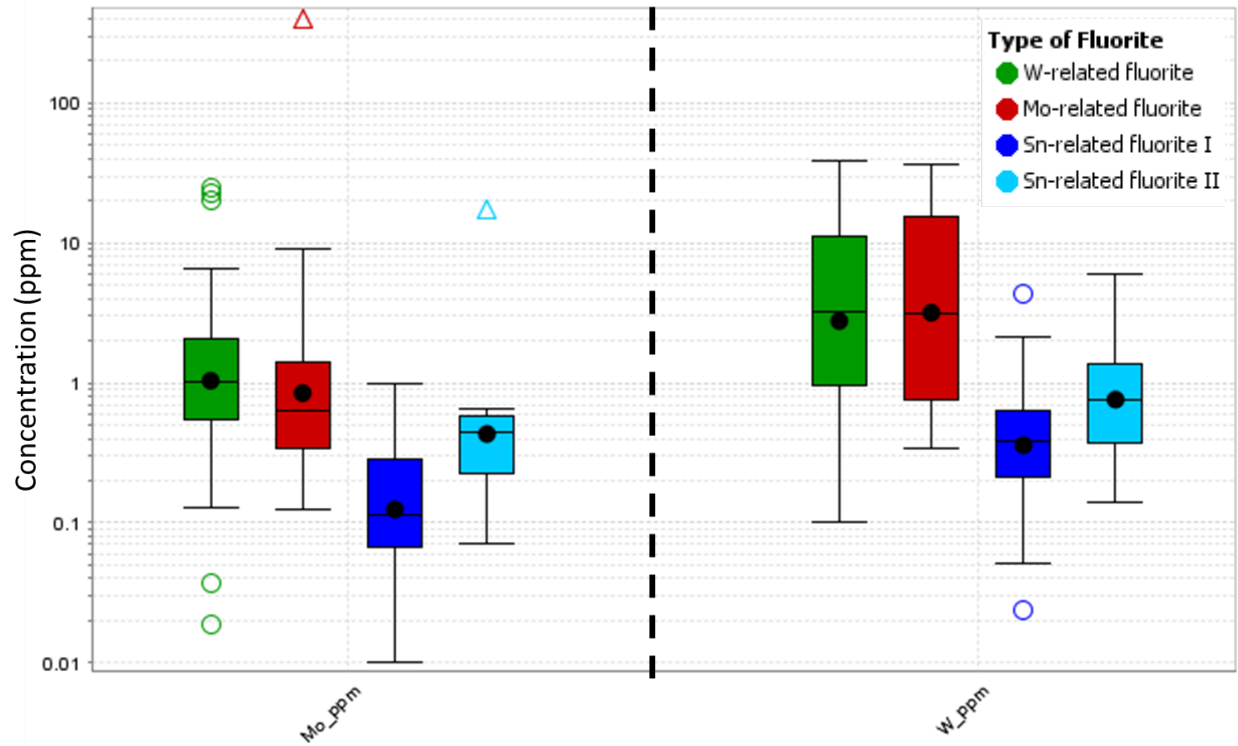


Figure 4.29 Box-whisker plot showing the concentration of Mo and W in the four different types of fluorite.

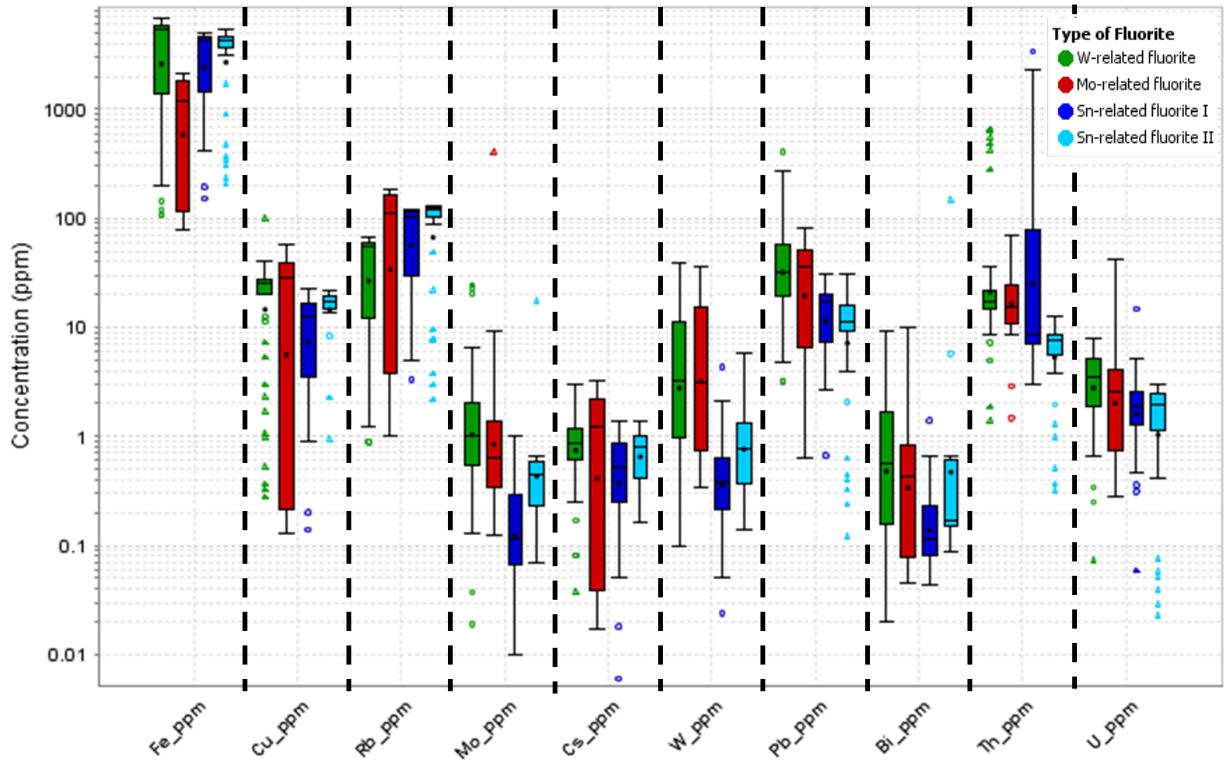


Figure 4.30 Box-whisker plot showing overlap in element concentrations among the different types of fluorite.

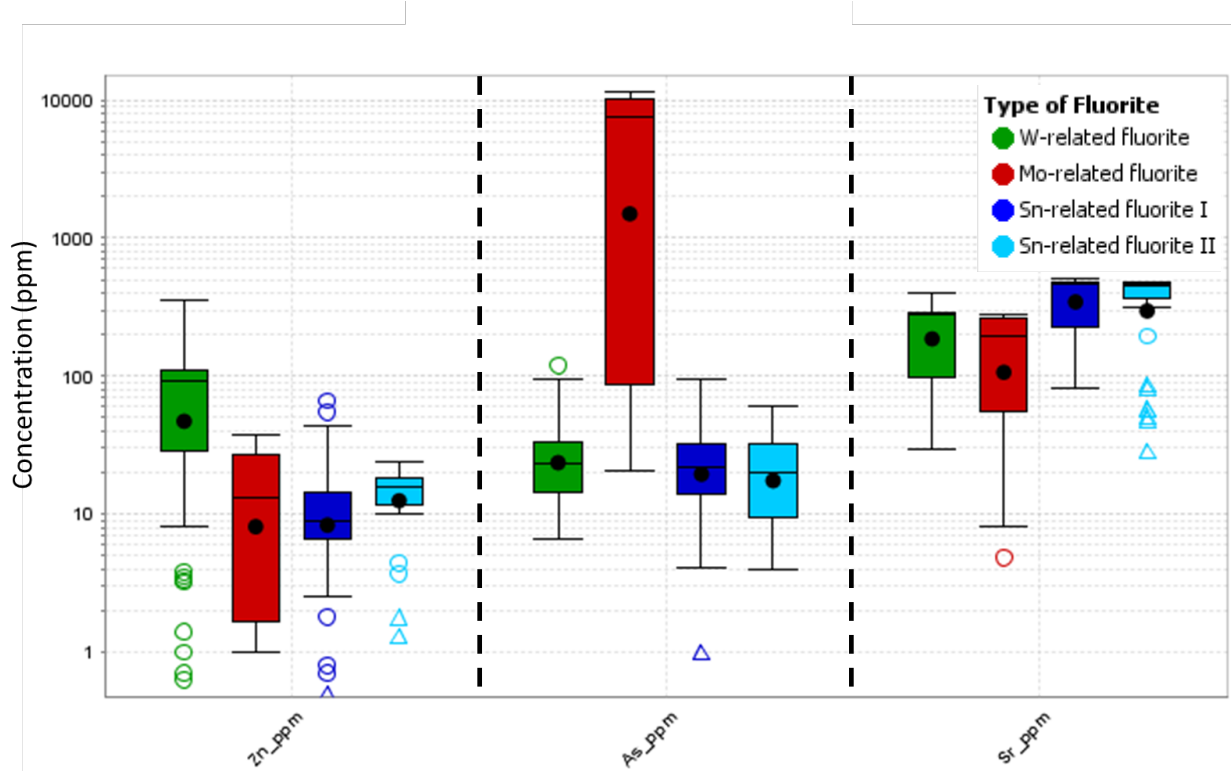


Figure 4.31 Box-whisker plot illustrating the elements with most notable differences in concentration among the different types of fluorite.

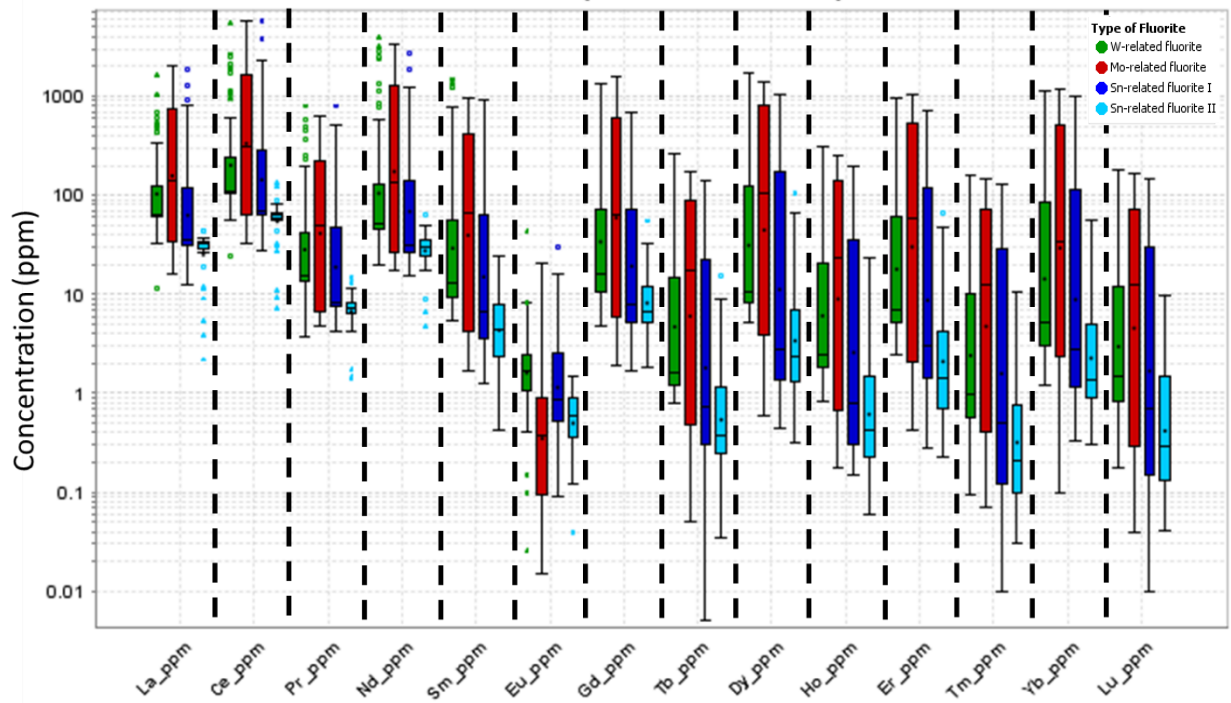


Figure 4.32 Box-whisker plot showing REE concentration in the different types of fluorite. Note that the highest REE concentrations are in Mo-related fluorite, followed by Sn-related fluorite I, W-related fluorite, and Sn-related fluorite II.

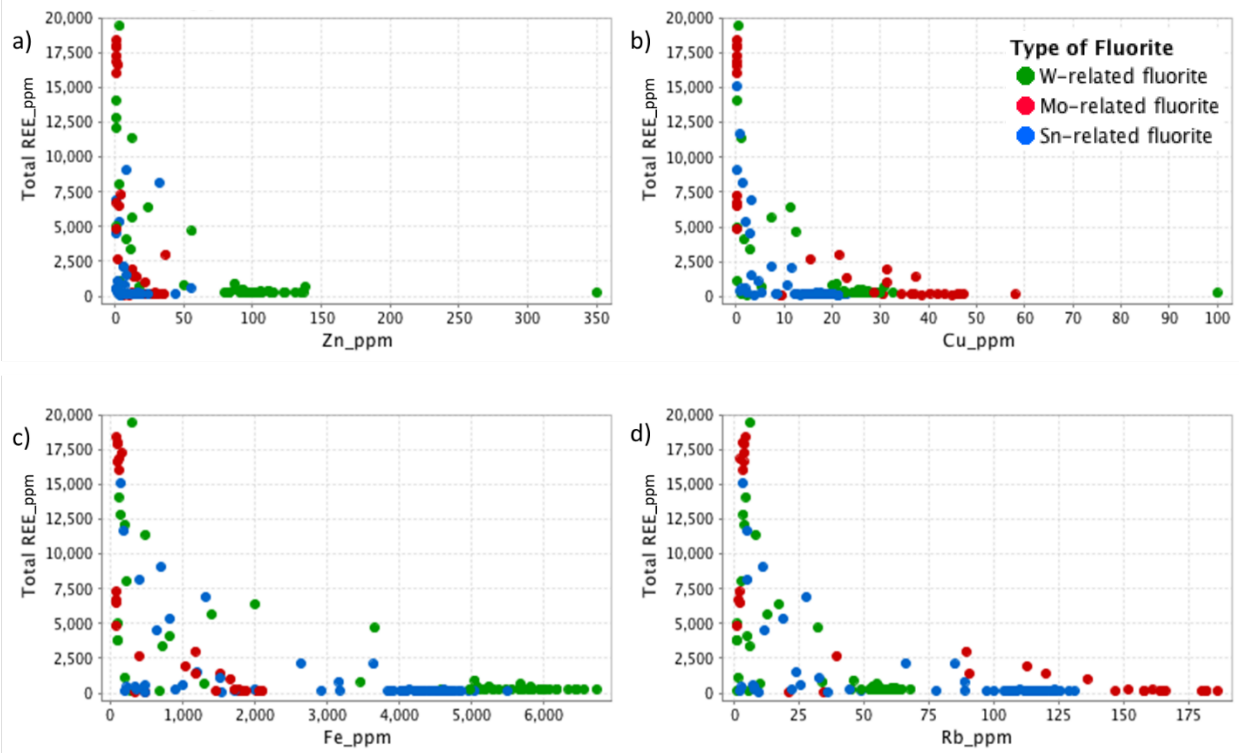


Figure 4.33 Element concentration plots of Zn, Cu, Fe, and Rb versus total REE showing the overall negative correlation between total REE and the other elements.

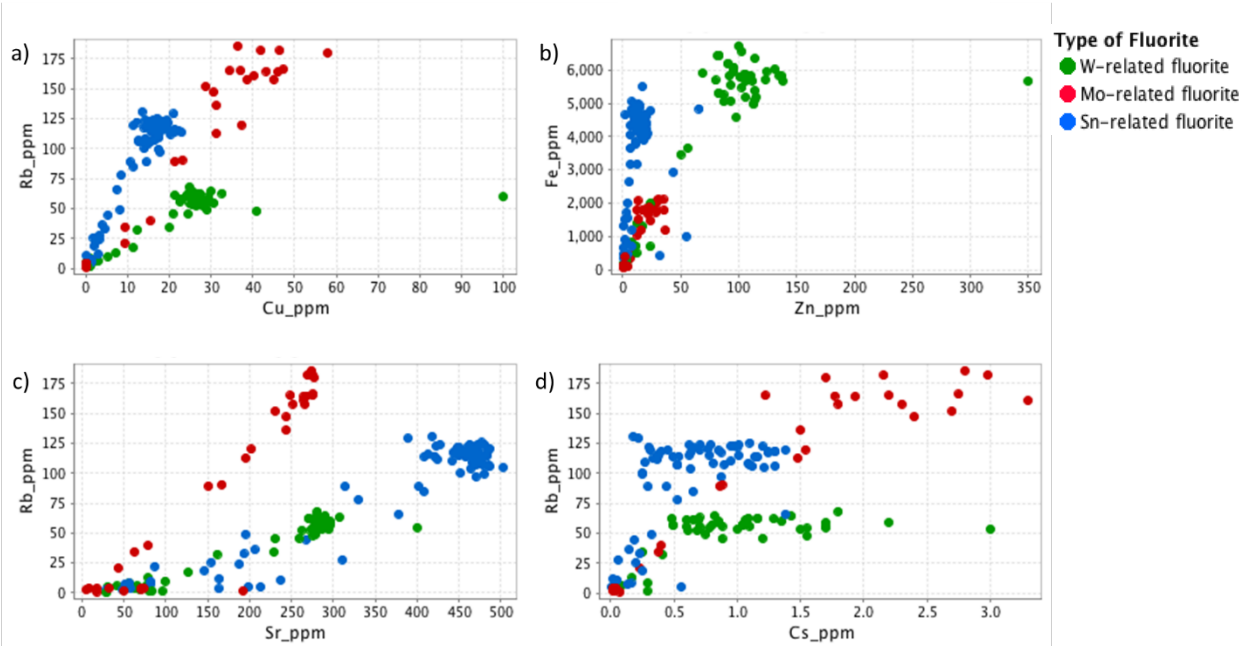


Figure 4.34 Element concentration plots of Cu vs Rb, Zn vs Fe, Sr vs Rb, and Cs vs Rb illustrating they all positively covary and that the different types of fluorite define distinct populations.

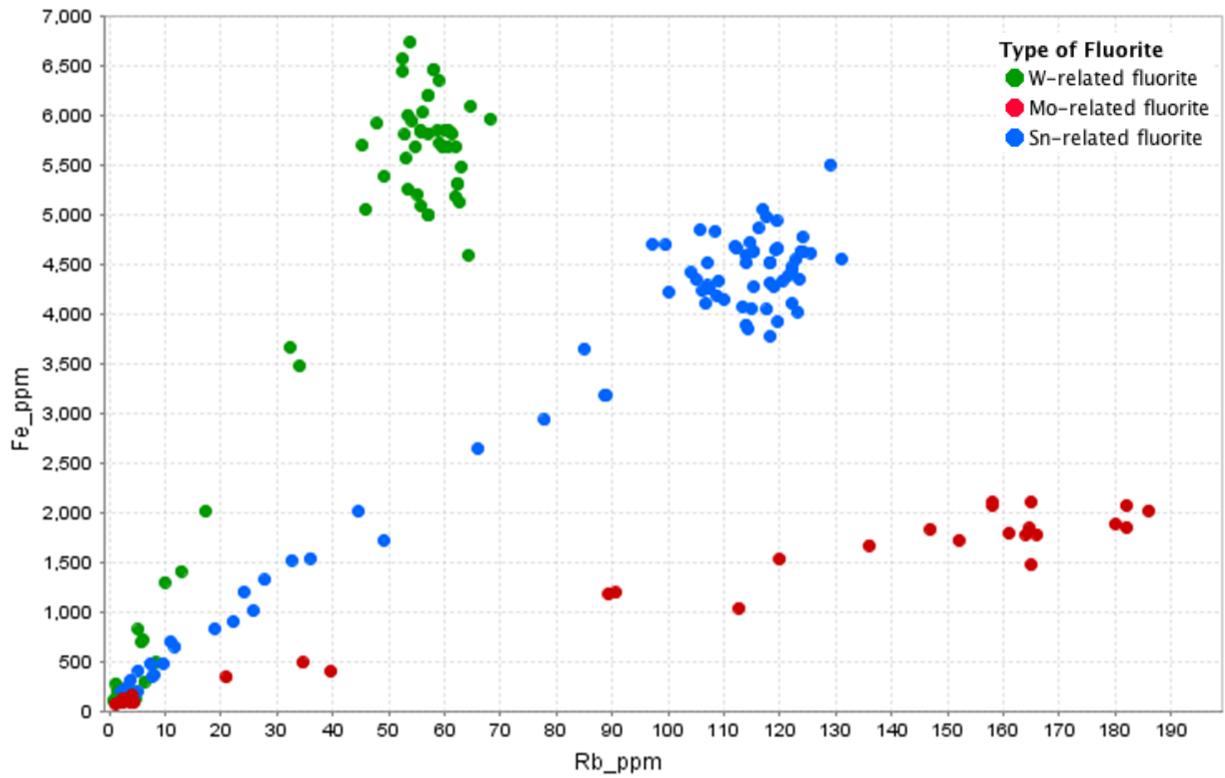


Figure 4.35 Fe vs Rb plot showing three distinct populations that correspond to the three fluorite types.

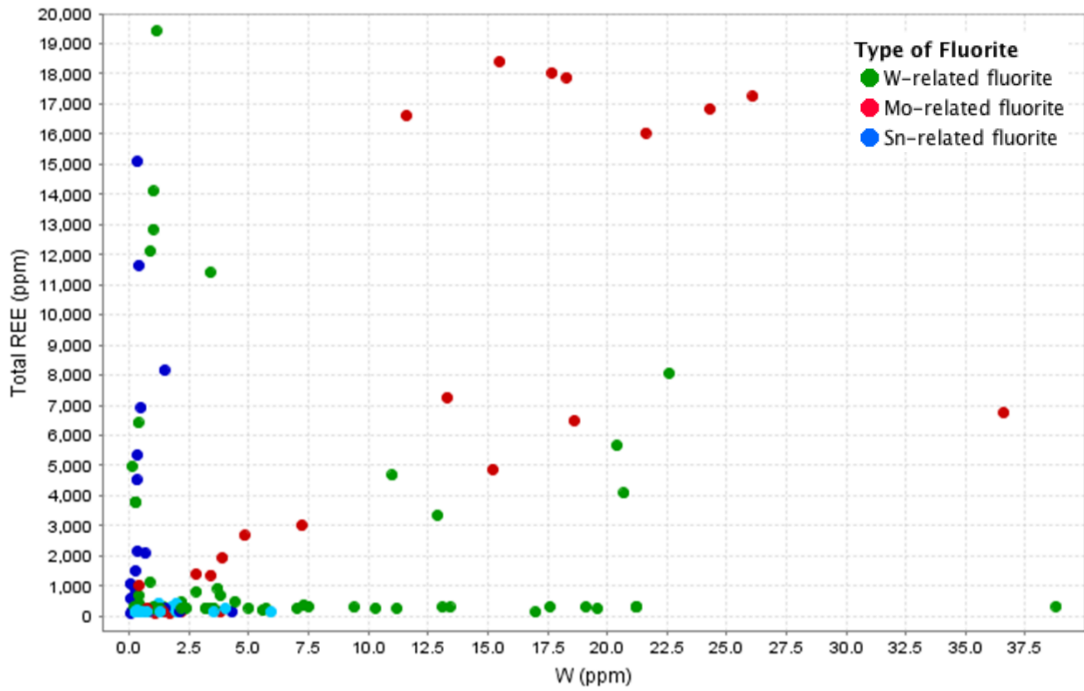


Figure 4.36 Bivariate plot of W versus total REE concentration showing both a negative correlation and a positive correlation, dependent on the type of fluorite.

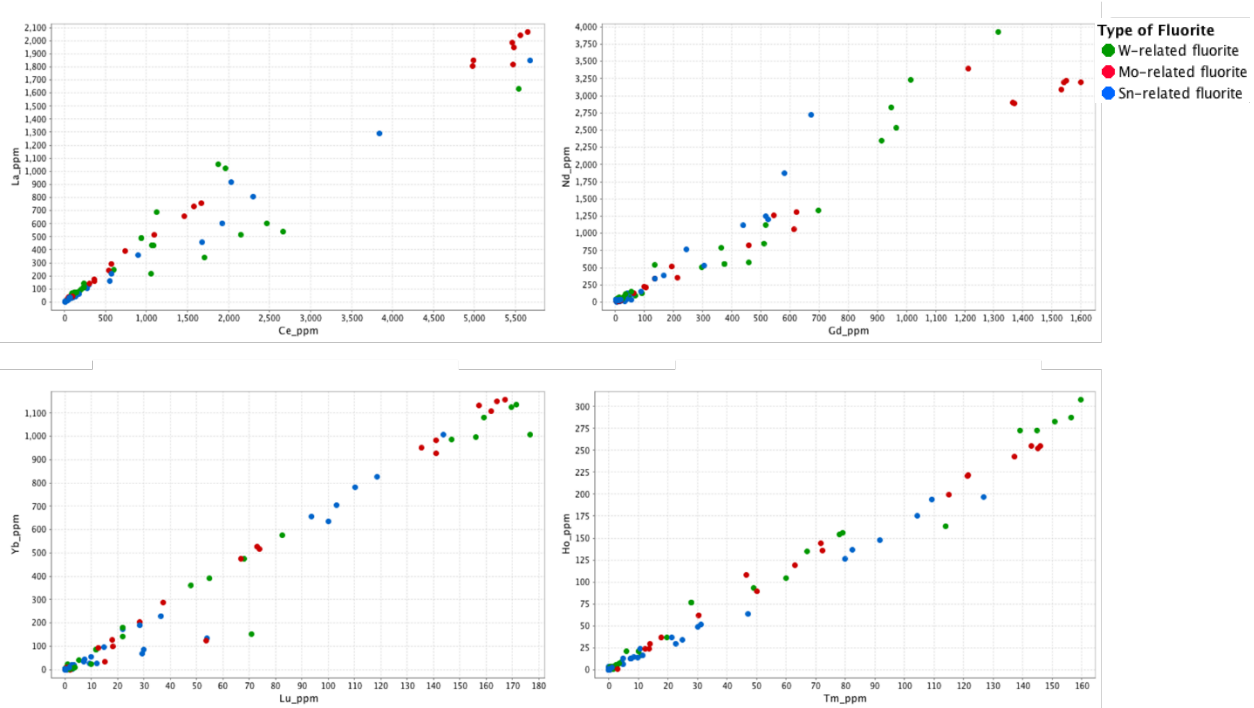


Figure 4.37 Bivariate plots of Ce vs La, Gd vs Nd, Lu vs Yb, and Tm vs Ho concentration to show they all positively covary.

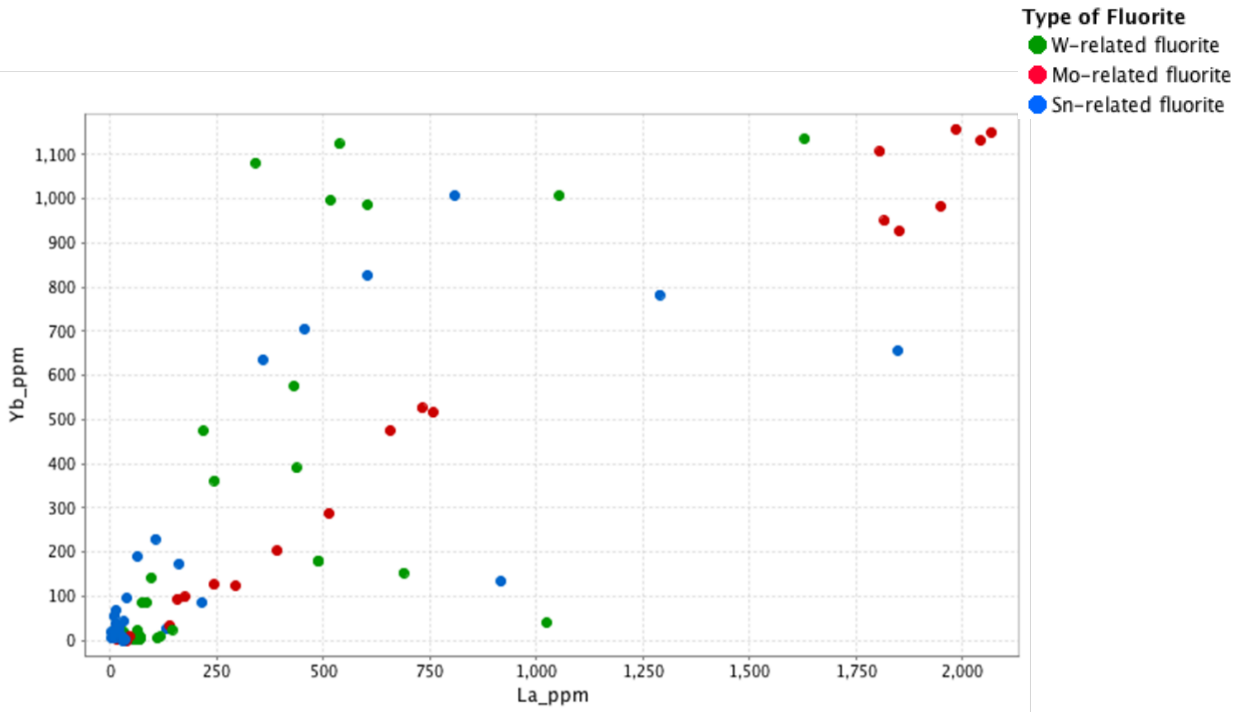


Figure 4.38 Bivariate plot of lanthanum versus ytterbium concentration showing a positive correlation with significant scatter.

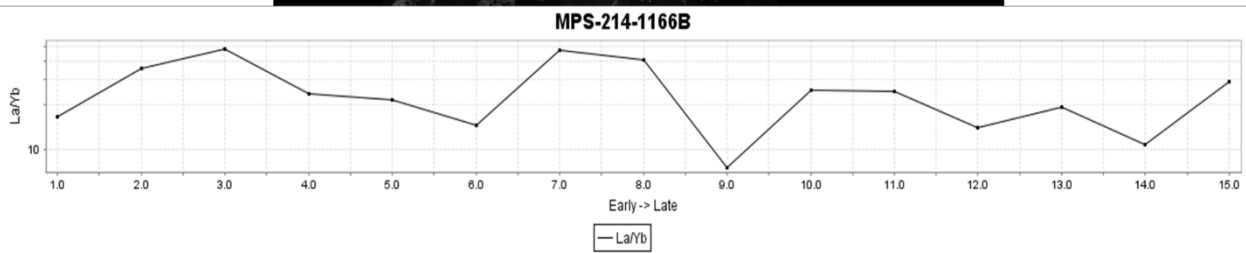
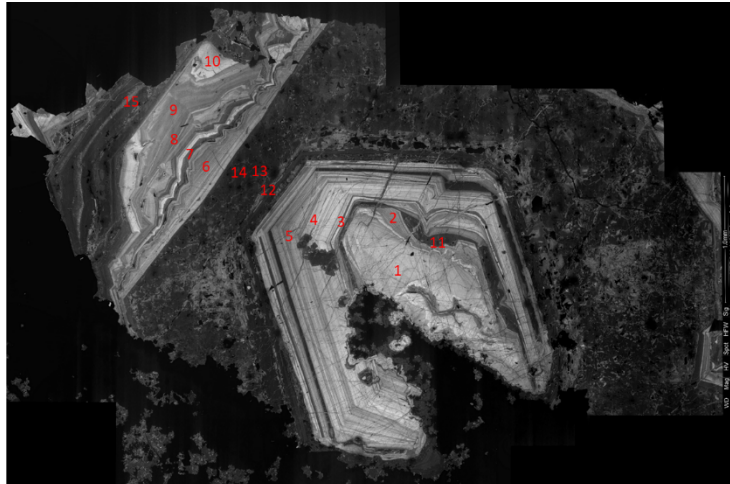
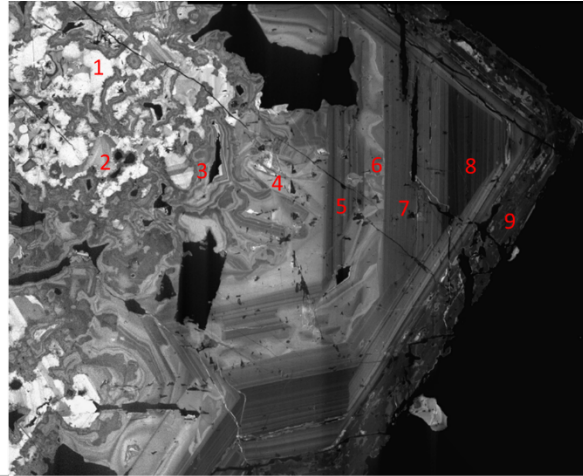


Figure 4.39 CL image of W-related fluorite and a line graph illustrating changes in La/Yb from the earlier to later generations of fluorite. Red numbers denote where LA-ICP-MS analyses were conducted and correspond to the numbers on the x-axis of the line graph below. All other line graphs are constructed in the same manner.



C23-125 A

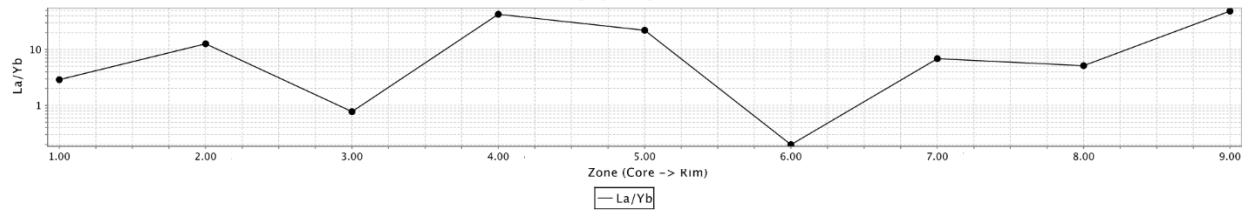


Figure 4.40 CL image of Sn-related fluorite I and a line graph illustrating changes in La/Yb from core to rim (Stages 1 through 4).

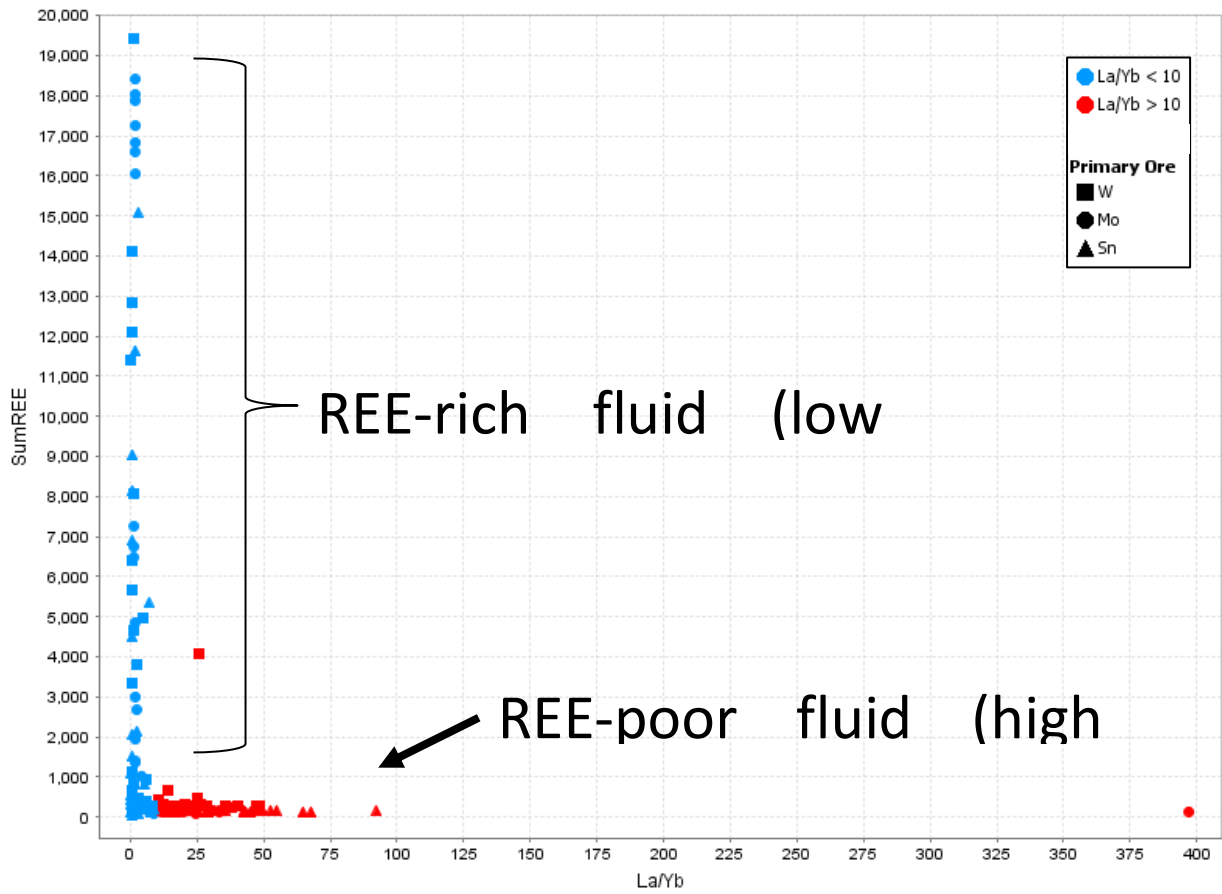


Figure 4.41 Lanthanum/ytterbium versus total REE plot showing a negative correlation.

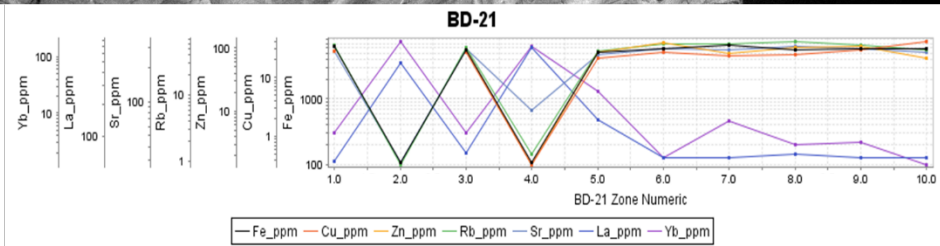
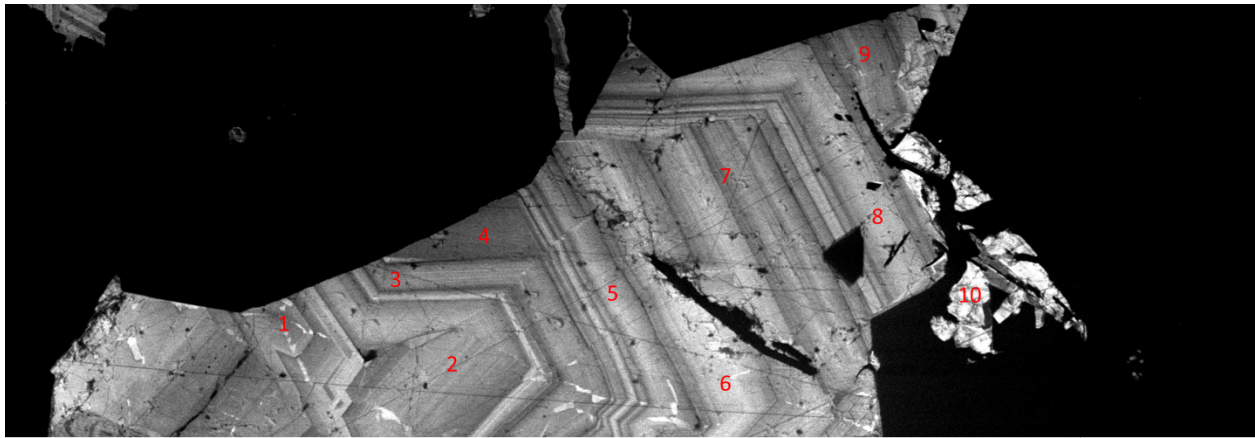


Figure 4.42 CL image of W-related fluorite and a line graph illustrating how Fe, Cu, Zn, Rb, Sr, La, and Yb vary throughout the crystal.

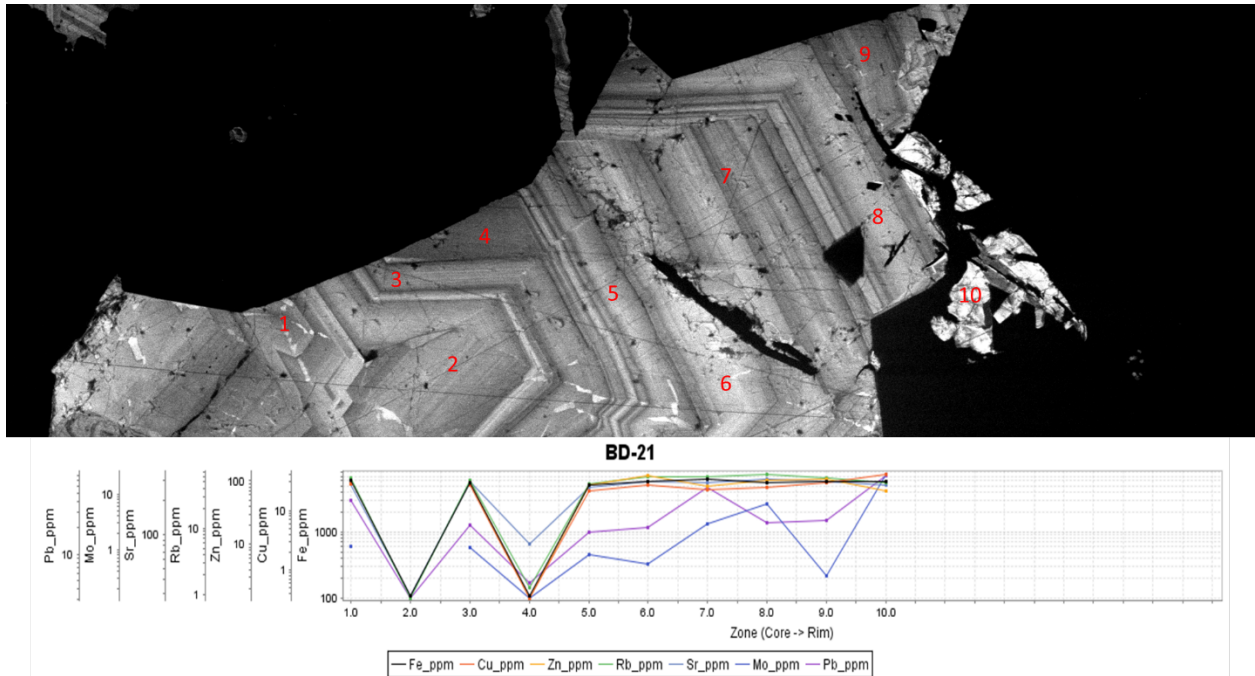


Figure 4.43 CL image of W-related fluorite and a line graph illustrating how Fe, Cu, Zn, Rb, Sr, Mo, and Pb all covary from core to rim within singular zones.

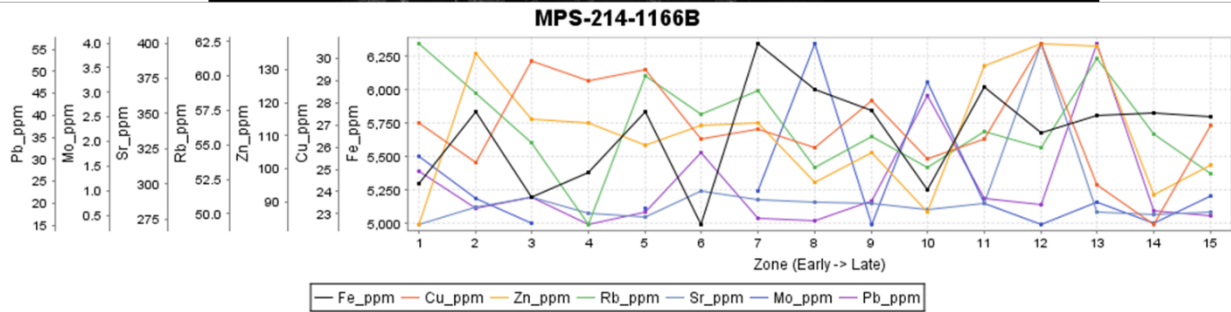
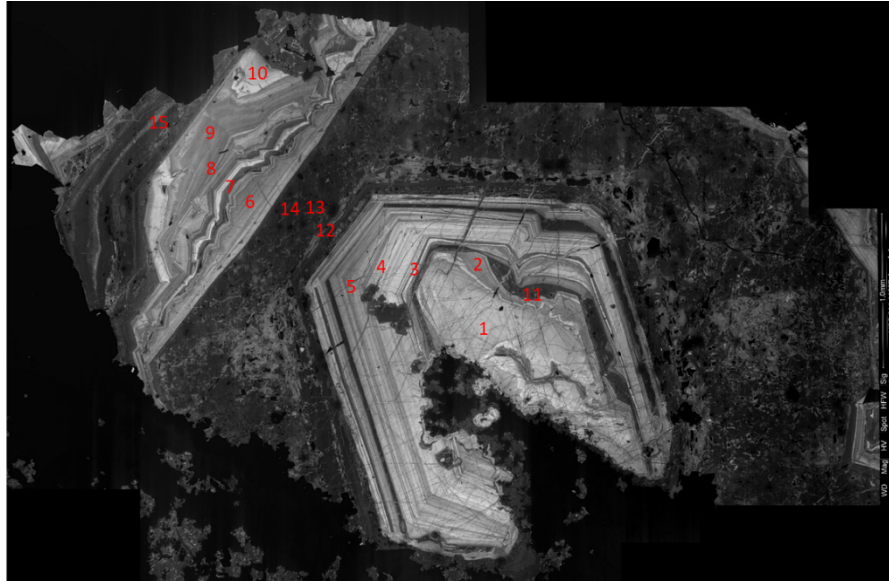


Figure 4.44 CL image of W-related fluorite and a line graph illustrating the exception where Fe, Cu, Zn, Rb, Sr, Mo, and Pb do not covary through a crystal.

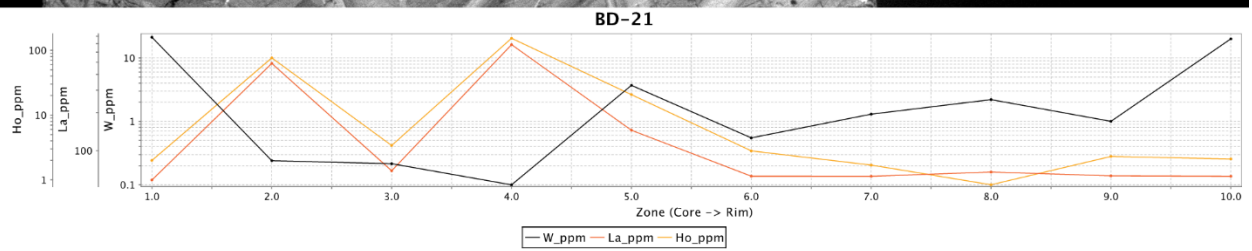
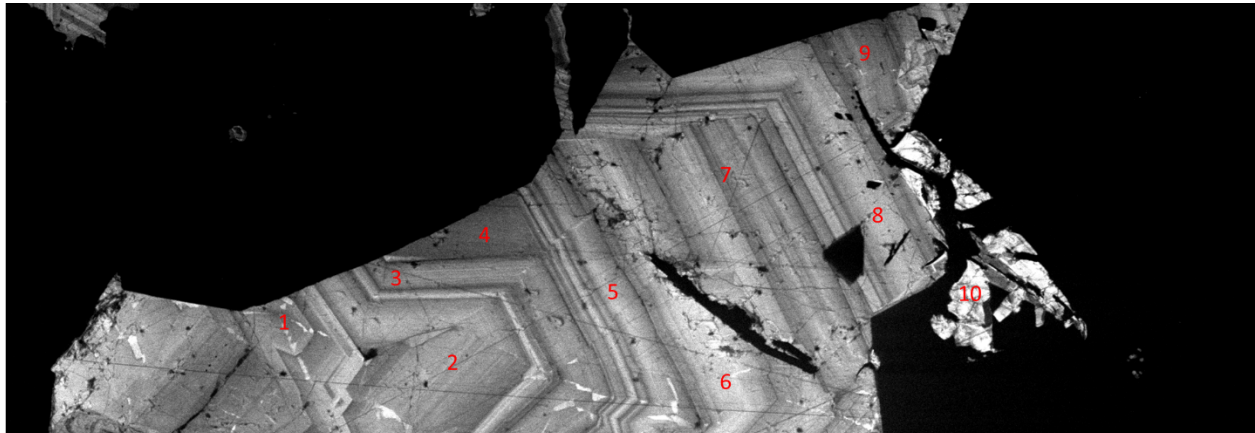


Figure 4.45 CL image of W-related fluorite and a line graph illustrating changes in W, La, and Ho from core to rim.

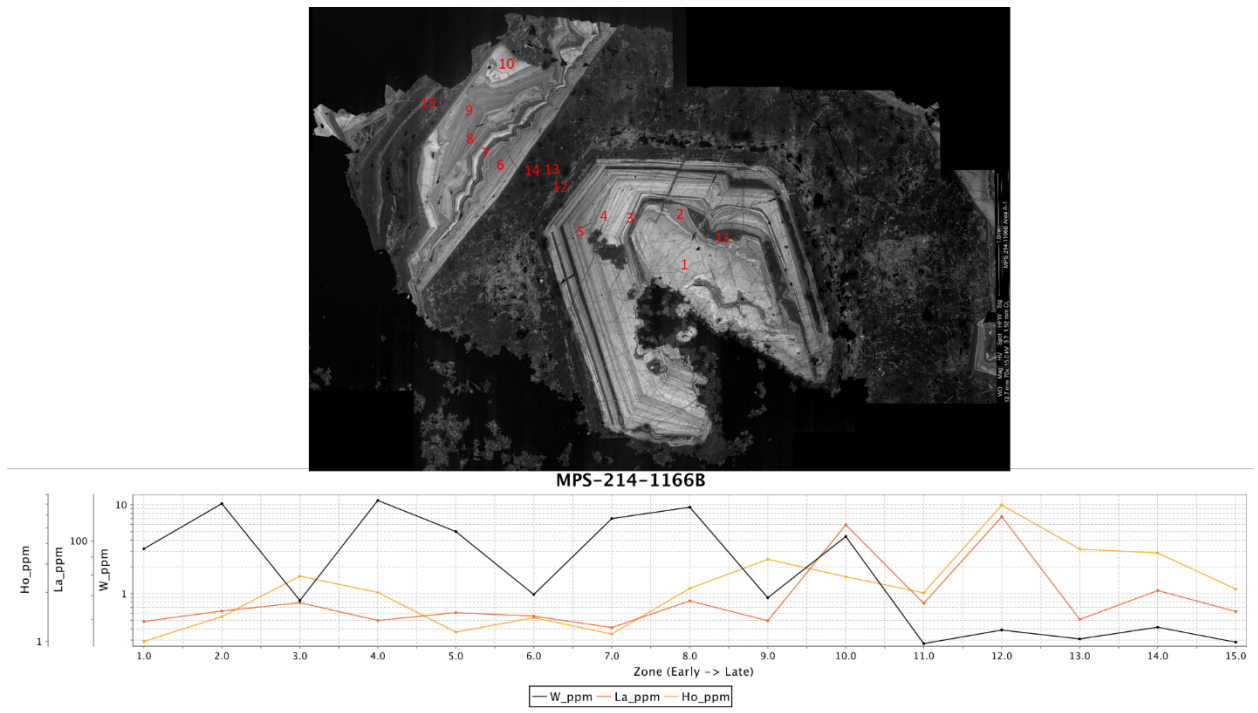


Figure 4.46 CL image of W-related fluorite and a line graph illustrating changes in W, La, and Ho from core to rim.

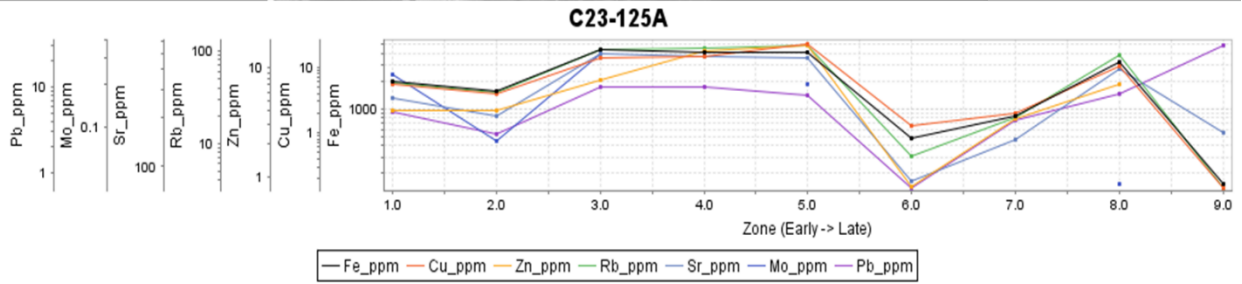
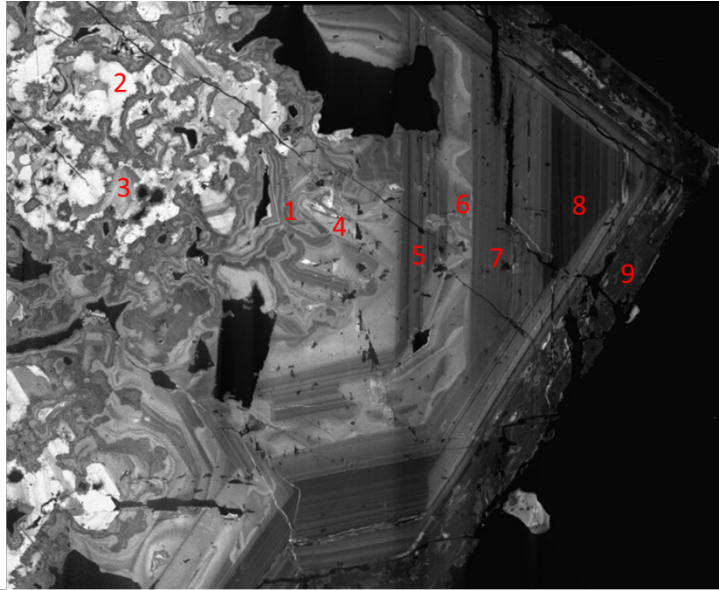
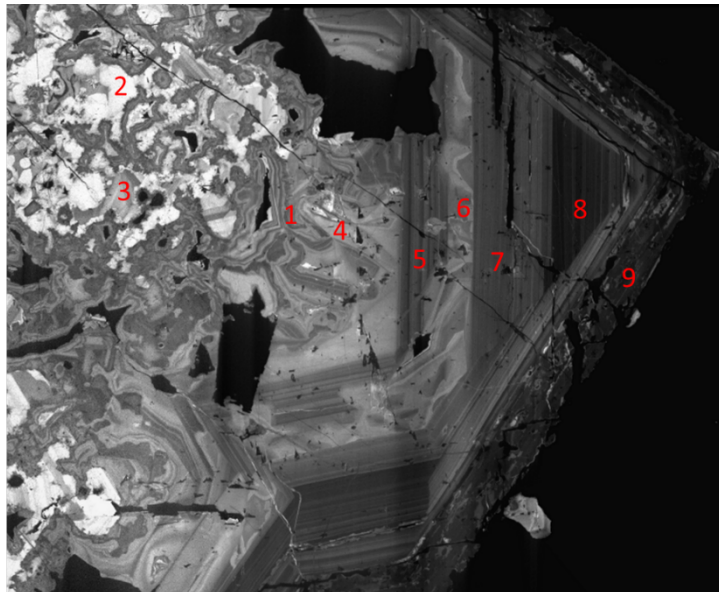


Figure 4.47 CL image of Sn-related fluorite I and a line graph illustrating how Fe, Cu, Zn, Rb, Sr, Mo, and Pb all covary from core to rim.



C23-125A

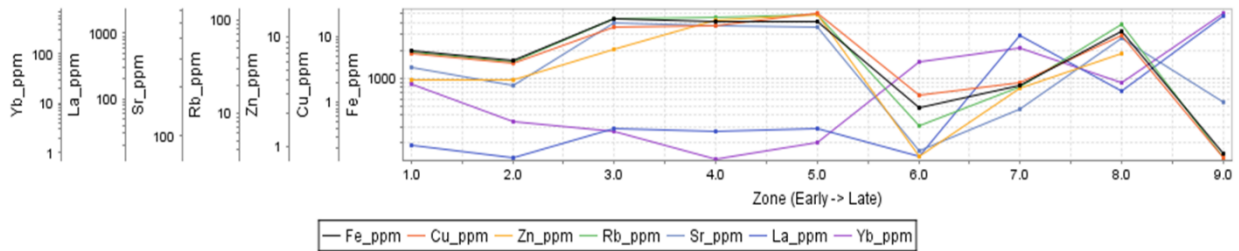


Figure 4.48 CL image of Sn-related fluorite I and a line graph illustrating how Fe, Cu, Zn, Rb, Sr, La, and Yb vary throughout the crystal.

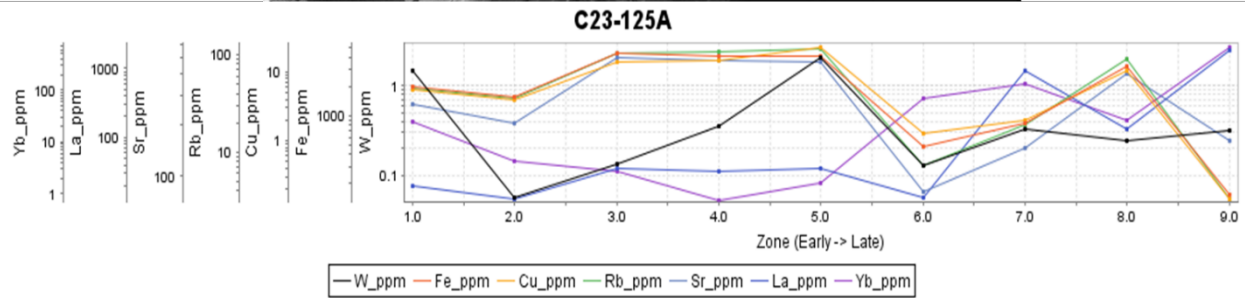
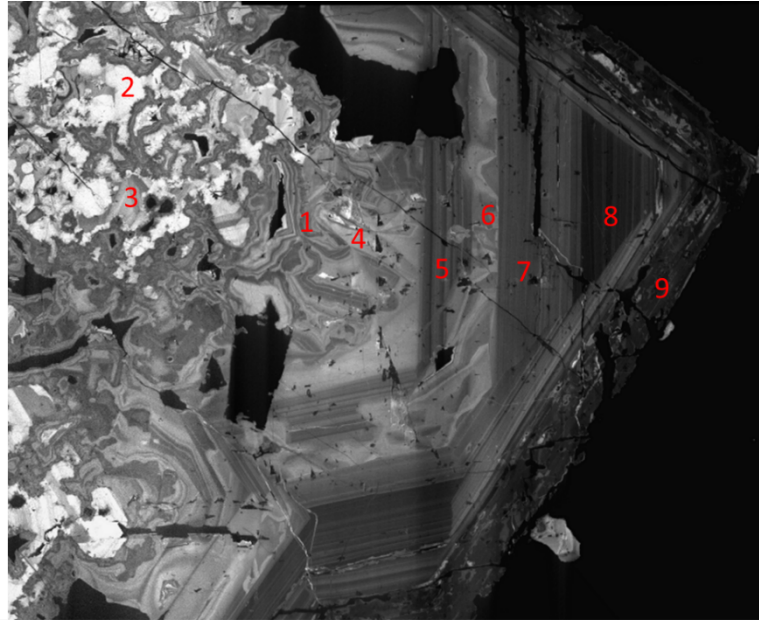
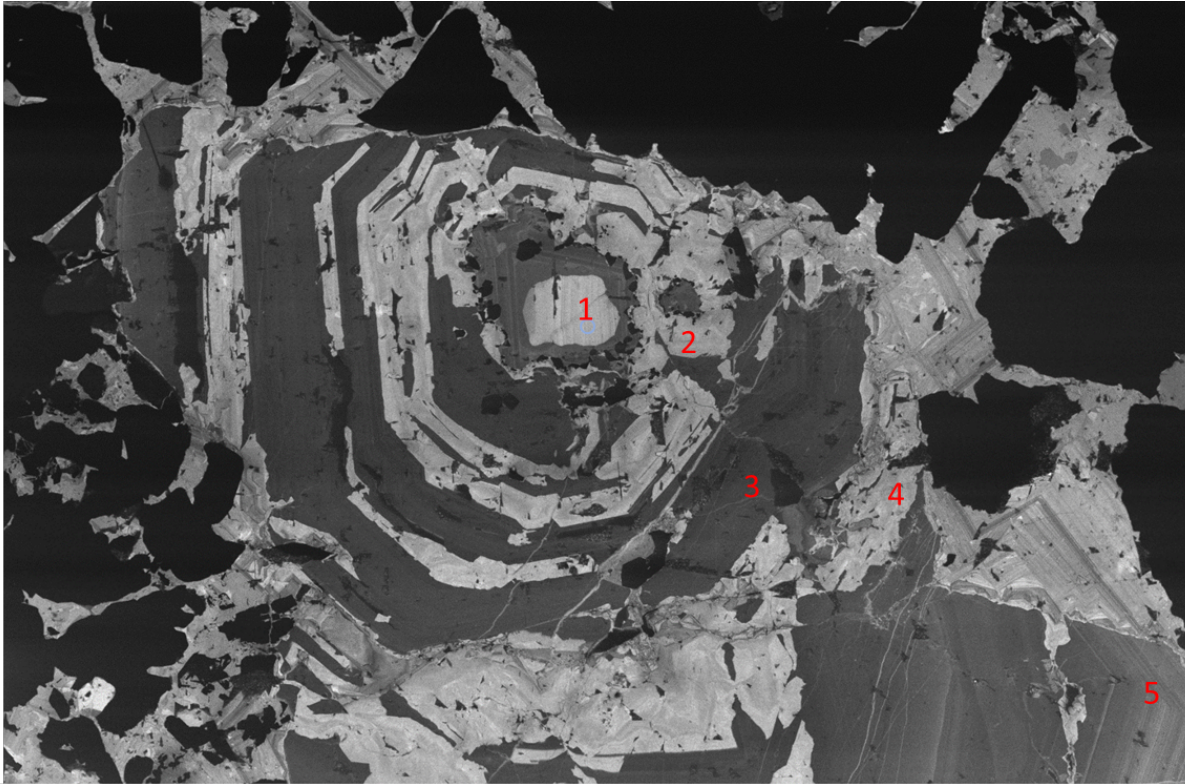


Figure 4.49 CL image of Sn-related fluorite I and a line graph illustrating how W, Fe, Cu, Rb, Sr, La, and Yb vary through a crystal.



C12-157A

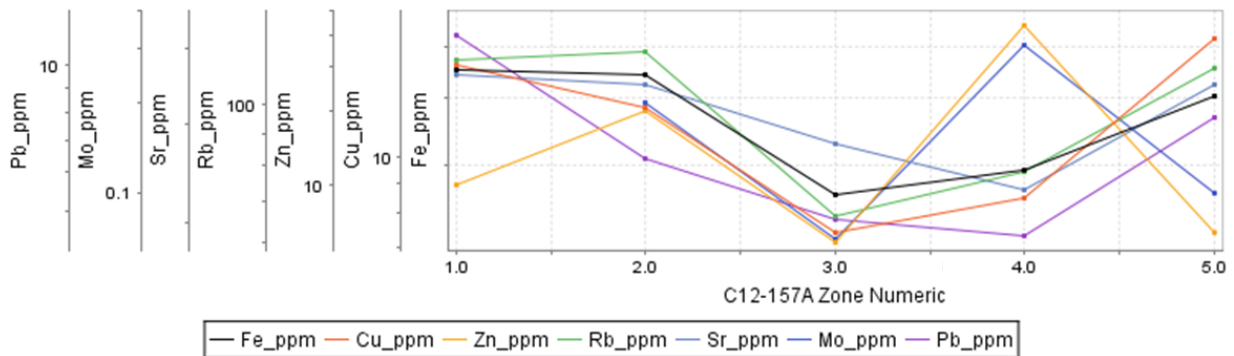
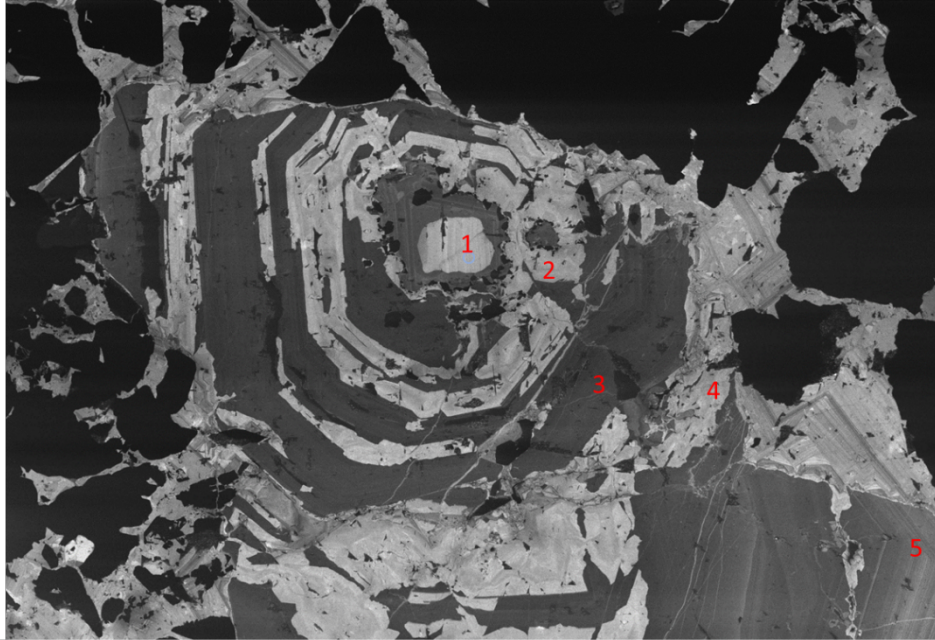


Figure 4.50 CL image of Sn-related fluorite II and a line graph illustrating how Fe, Cu, Zn, Rb, Sr, Mo, and Pb vary within between different zones in a crystal.



C12-157A

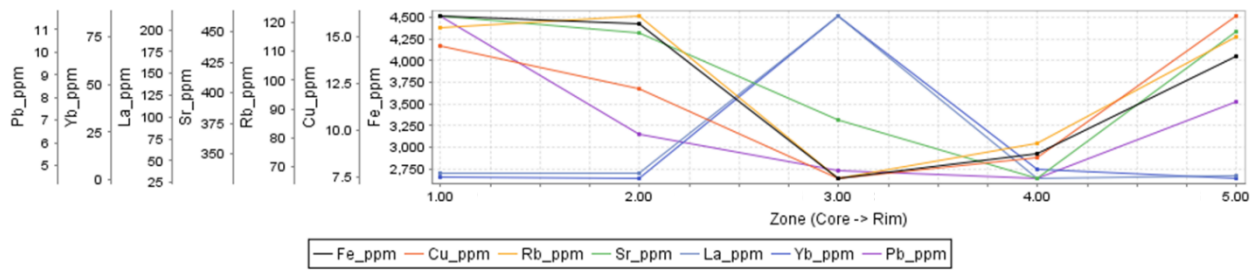
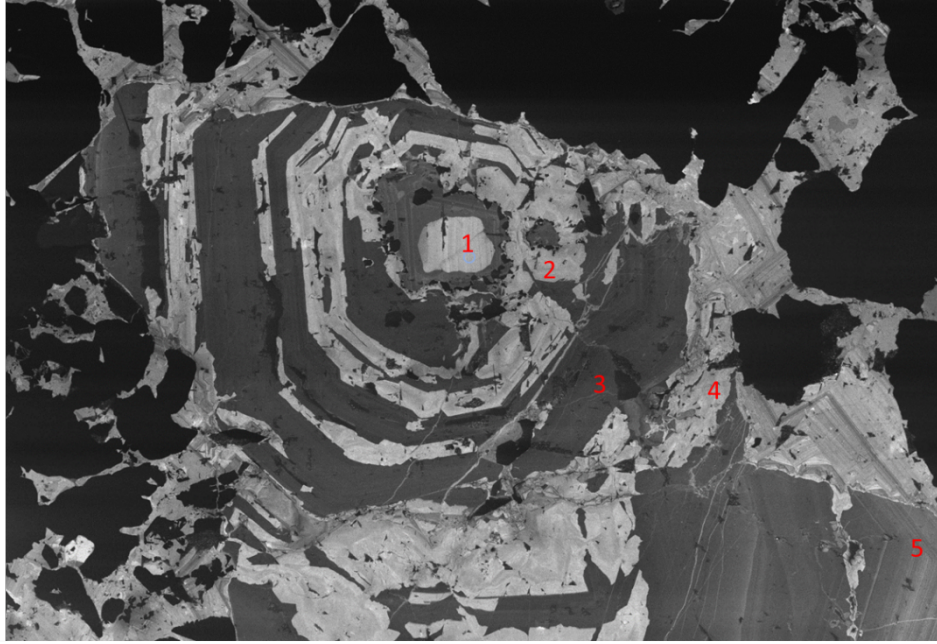


Figure 4.51 CL image of Sn-related fluorite II and a line graph illustrating how Fe, Cu, Rb, Sr, Pb, La, and Yb vary between different zones.



C12-157A

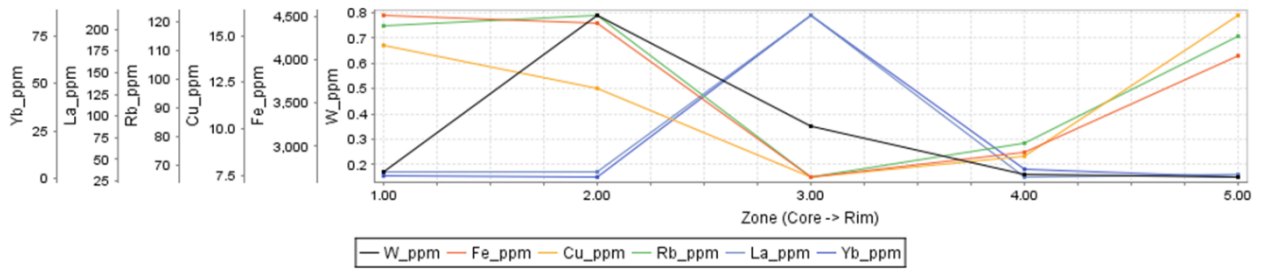


Figure 4.52 CL image of Sn-related fluorite II and a line graph illustrating how W, Fe, Cu, Rb, Sr, La, and Yb vary between different zones.

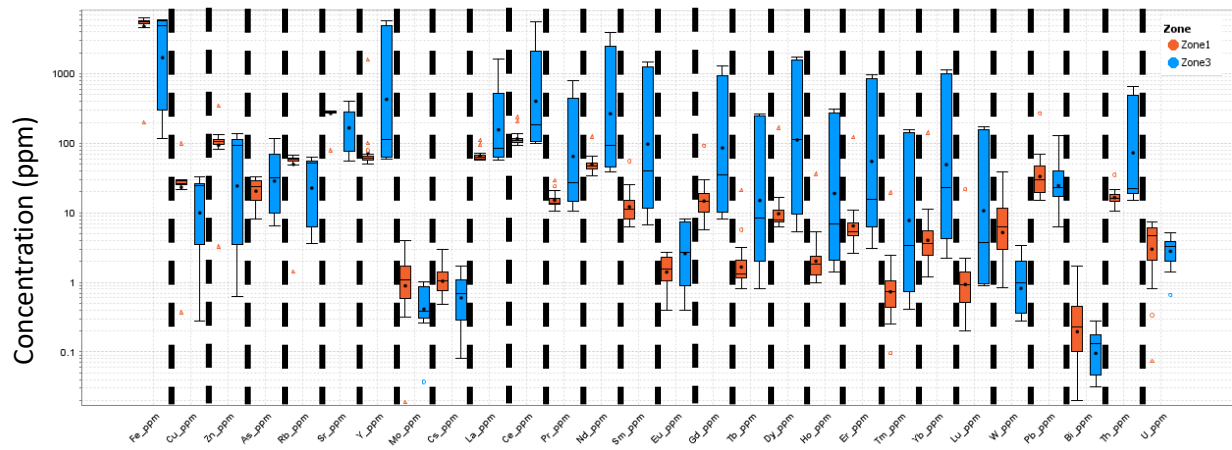


Figure 4.53 Box-whisker plot comparing the planar zones (Zone 1) in MPS to the dark-CL, mineral inclusion-rich zones (Zone 3).



Figure 4.54 Laser ablation spectra of a zone of W-related fluorite with numerous REE-mineral inclusions, illustrating the uniformity of the spectra.

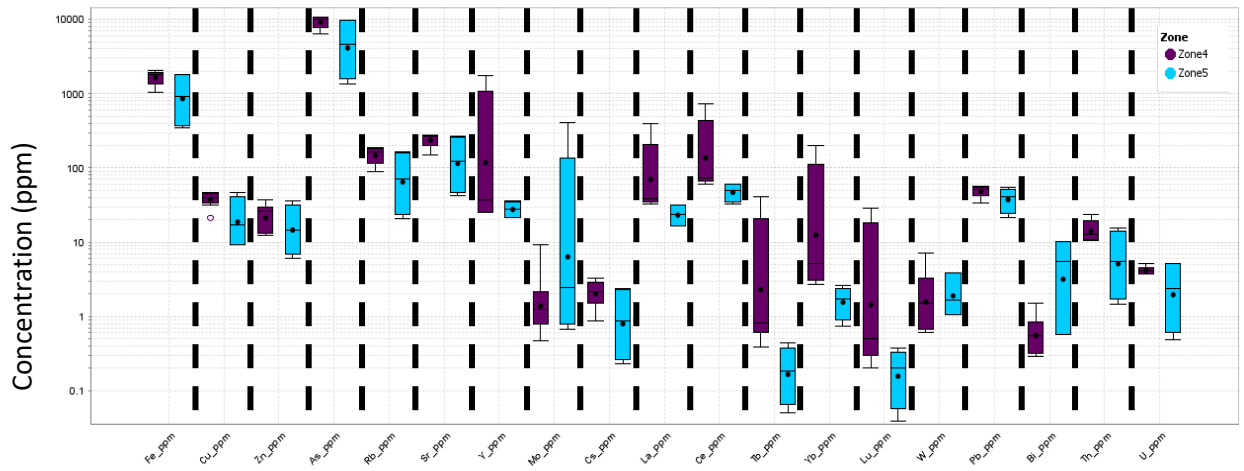


Figure 4.55 Box-whisker plot comparing element concentrations in dull, homogenous Mo-related fluorite to those with a bright rim that is mantled by molybdenite.

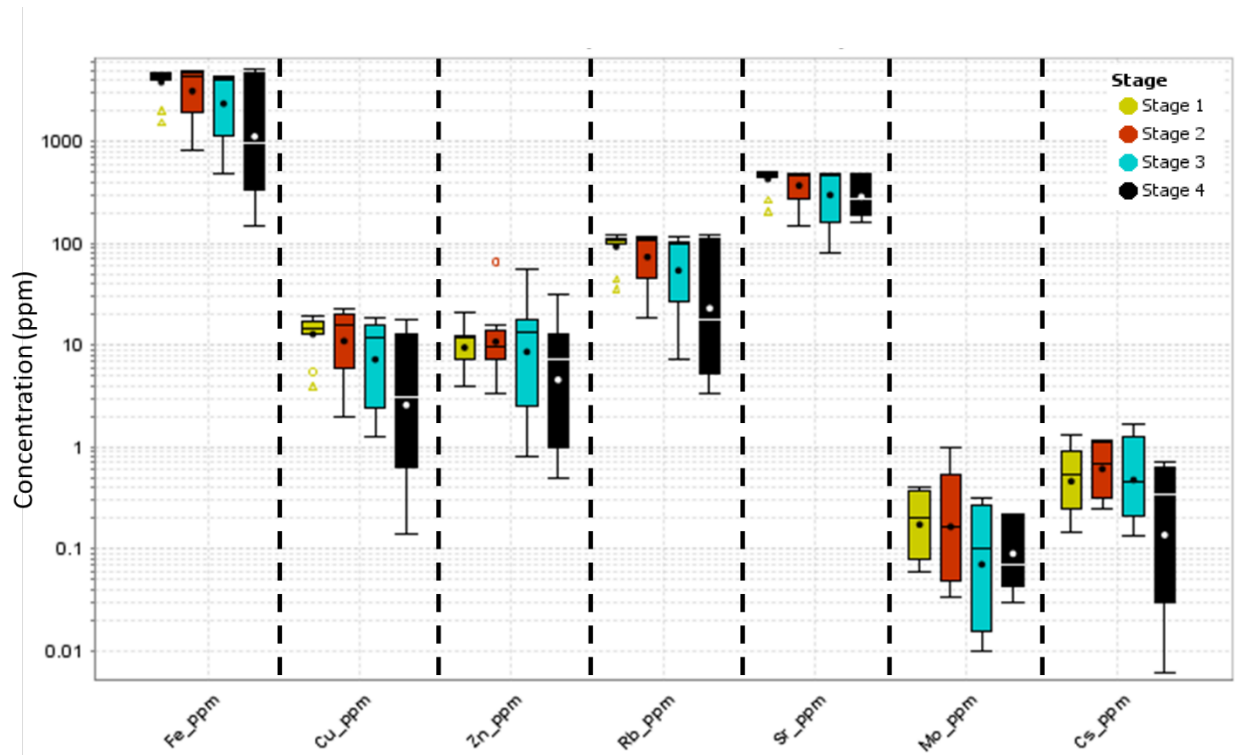


Figure 4.56 Box-whisker plot showing that Fe, Cu, Zn, Rb, Sr, Mo, and Cs decrease in concentration from Type 1 to Type 4 Sn-related fluorite I.

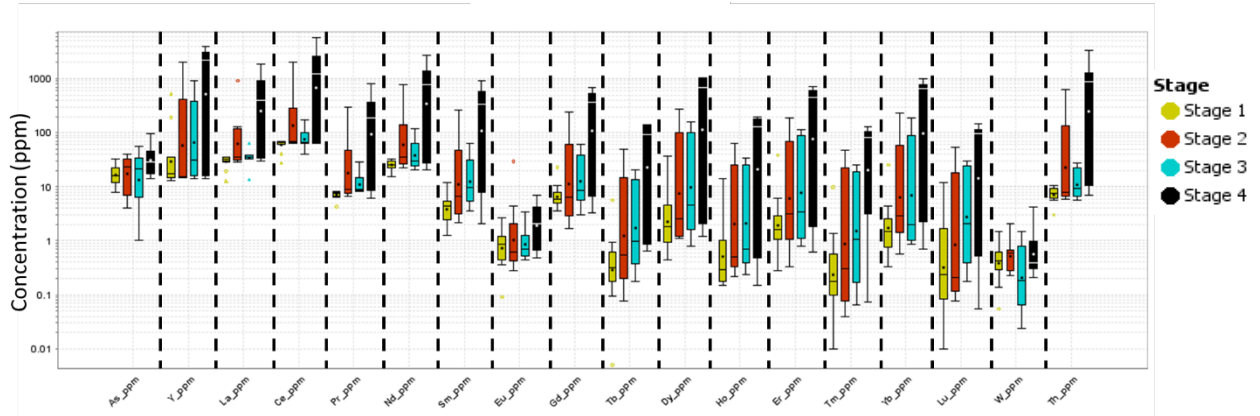


Figure 4.57 Box-whisker plot showing that As, W, REE, Y, and Th increase in concentration from Type 1 to Type 4 Sn-related fluorite I.

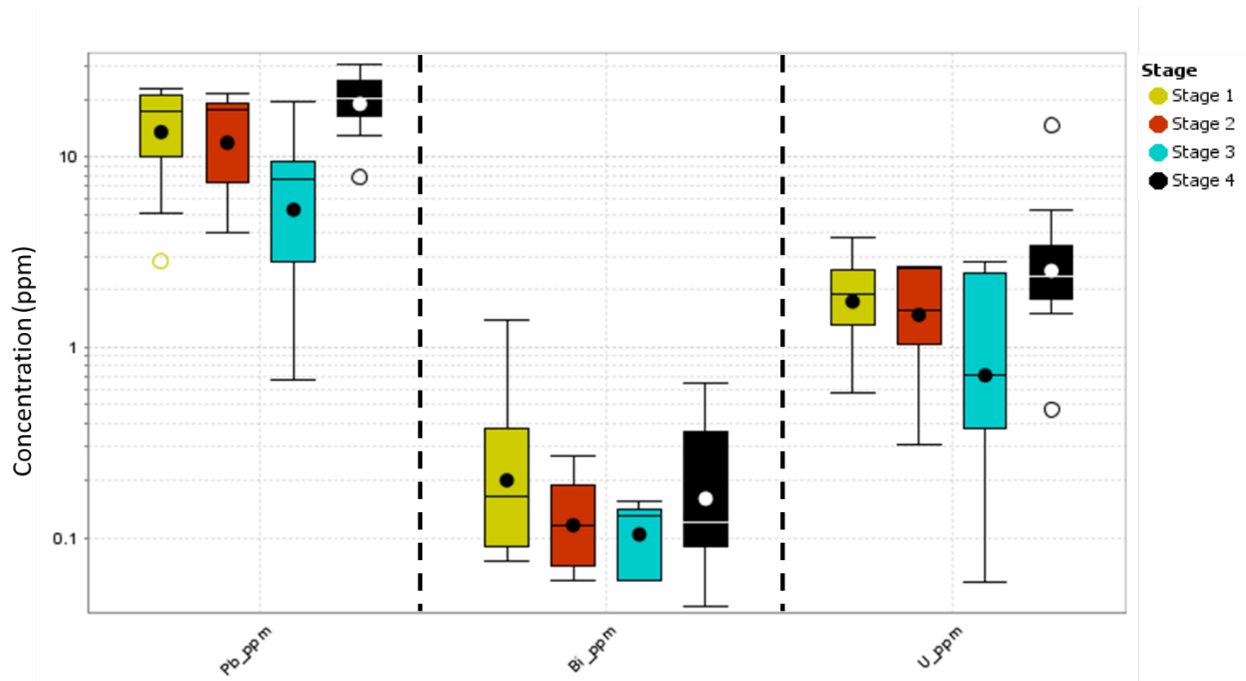


Figure 4.58 Box-whisker plot showing Pb, Bi, and U are similar in concentration in Type 1, Type 2, and Type 4 but are lower in concentration in Type 3 Sn-related fluorite I.

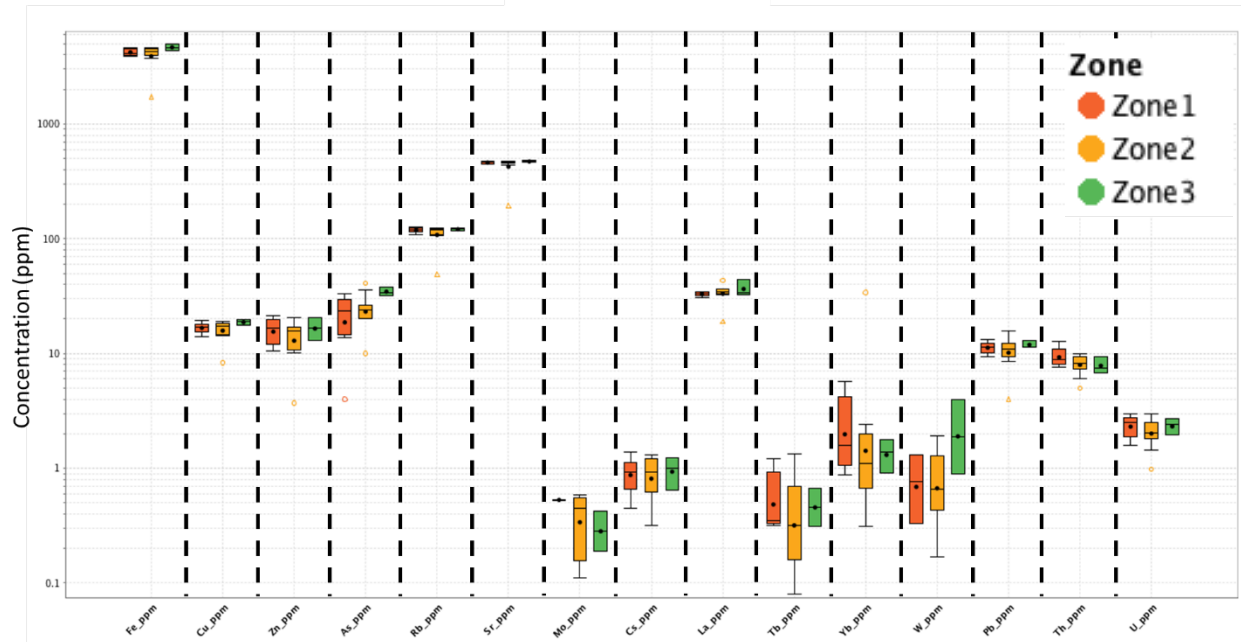


Figure 4.59 Box-whisker plot showing similar element concentrations of three different generations of Sn-related fluorite II in one grain of fluorite.

CHAPTER 5

Discussion

5.1 Previous Work

Assadzadeh et al. (2017) compared the metal ratios and REE concentrations in fluorite from the different orebodies and between the different fluorite types in both the Fire Tower Zone and North Zone. These analyses represented averages taken across multiple growth zones and only three traverses were acquired from individual growth zones in one fluorite crystal. Averaging data across growth zones prevents any subtle changes in fluid composition from being detected, especially considering the complexity exhibited in the fluorite crystals at Mt. Pleasant (Fig. 4.17). In addition, Assadzadeh et al. (2017) reported Sn concentrations in fluorite samples. In this study, Sn was not detected in fluorite (Fig. 5.1). Rather, where Sn was detected it is interpreted to have been derived from ablation of the glue below the rock thin section.

5.2 Fluorite Growth History

Cathodoluminescence images show that most of the W- and Mo-related fluorite has had a simple growth history, as recorded by planar growth zones or homogenous crystals, respectively. Lack of zoning in fluorite crystals indicates that crystallization occurred under relatively constant physicochemical conditions (Götze et al., 2005), whereas oscillatory zoning indicates a varying crystallization environment (Götze et al., 2013). This suggests that Mo-related fluorite formed under constant physicochemical conditions. The bright zones where fluorite is mantled by molybdenite may have resulted from the beta decay of ^{187}Re to ^{187}Os in the adjacent molybdenite, which damaged the fluorite crystal lattice causing a rim with a different CL character (cf. Balogun et al., 1999). The changing conditions under which W-related fluorite formed, as suggested by its planar growth zones (Fig. 14), could have been due to: (1) changing fluid composition over time, (2) different densities of defects during crystal growth, (3) changing growth conditions (i.e. redox conditions, pH, and T), (4) the delay between interface kinetics of a growing crystal and the diffusion of a chemical species in the fluid to the crystal-fluid interface, or any combination of these (Allégre et al., 1981; Götze et al., 2013).

One sample from the FTZ (MPS-214-1166) exhibits a different history from the other W-related fluorite samples. Fluorite crystals from this sample exhibit planar zoning similar to other W-related crystals, but differ in that large (>1mm thick in some places), mineral inclusion-rich, dark-CL zones are present (Fig. 3). The inclusions include REE fluorocarbonate minerals, monazite, wolframite, chlorite, and hematite (Fig. 3). These zones are interpreted to be a late replacement feature based on petrographic, textural, and trace-element chemistry evidence. Both the replacement zones and the smaller replacement fluorite in vugs in the alteration halo (Fig. 2) around the vein containing fluorite are pitted, contain abundant mineral inclusions, and have identical CL character, suggesting they formed during the same replacement event (cf. Harlov et al., 2002; Hellmann and Tisserand, 2006; Putnis, 2009). The trace element chemistry of these replacement zones also differs from the original growth zones as they have lower metal and higher

REE concentrations than the original growth zones. CL images also show that borders between these dark zones and adjacent bright zones are sharp and well-defined. If these zones were the product of a structurally controlled (e.g. fracture- or cleavage-related) dissolution and reprecipitation event, one would expect irregular boundaries. This suggests the original fluorite zones that were replaced were chemically favorable and selectively replaced. Some studies have shown that REE mineral inclusions can nucleate as a result of dissolution-reprecipitation of a REE-bearing host, leaving a secondary REE-depleted host with abundant REE-mineral inclusions (Harlov et al., 2002; 2003; 2005). The replacement fluorite zones with abundant REE-mineral inclusions, however, have relatively high REE concentrations, suggesting that the fluorite was not leached of its REE content but rather the REE were externally sourced.

The REE minerals in the REE-rich replacement zones have a modal abundance of approximately 10 volume % and an average Ce concentration of 38 wt. %. The REE-rich fluorite that hosts these minerals has, on average, approximately 1000 ppm Ce. The concentration of Ce required to precipitate the amount of secondary REE fluorocarbonate mineral inclusions observed in a 1 mm cube of fluorite, in addition to the 1000 ppm concentration of Ce in the host fluorite, necessitates that the precursor fluorite contained approximately 38,900 ppm or 3.89 wt. % Ce. This is highly unlikely, as the highest concentration of cerium measured in fluorite at Mount Pleasant is 5,680 ppm. A more plausible hypothesis is that the fluid responsible for the replacement was enriched in REE, creating both REE-rich fluorite and REE fluorocarbonate mineral inclusions. This fluid was also likely enriched in W as indicated by the abundance of wolframite associated with this replacement event. Although the W concentrations in the fluorite replacement zone are lower than in the primary fluorite, this is likely because W concentrations in the fluid were lowered due to the precipitation of wolframite.

Sn-related fluorite I in the NZ exhibits very complex CL textures in their cores. Sn-related fluorite I clearly represents a complex fluid history, but it is unclear what role, if any, this later fluid played in cassiterite precipitation. This fluorite is interpreted to have developed in the following way: textural relationships suggest that the first generation of fluorite growth is represented by dark-CL zones containing euhedral, acicular crystals of topaz (Fig. 19), with some in close proximity to pre-existing quartz and chlorite grains (Fig. 9 and 19). Subsequently, bright-CL fluorite precipitated, followed by dull-CL fluorite that precipitated into the remaining open space. Zones around the core are planar and alternate between light and dark luminescence. These planar zones show irregular zone boundaries and cross earlier zones that suggest replacement and dissolution of some zones by later fluids, which precipitated a later generation of fluorite (Fig. 22). A final rim of dark-CL fluorite is present that contains abundant REE fluorocarbonates and monazite. Similar to replacement zones in the W-related fluorite, this rim of fluorite is also enriched in REE compared to other zones within the crystal (Fig. 38). Following this REE-rich rim, arsenopyrite and cassiterite precipitated. This relationship further supports a link between REE mineral saturation and (in this case subsequent) ore precipitation.

Sn-related fluorite II also records a complex fluid history that involved the precipitation of an early dark-CL fluorite that underwent dissolution during a later fluid infiltration event. The fluorite that

precipitated after this dissolution event is characterized by bright-CL zones slightly protruding into adjacent dark-CL zones, to thin bright-CL zones that crosscut large dark-CL crystals, to extensively dissolved cores of crystals with rounded dark-CL relicts of earlier fluorite in a matrix of later precipitated bright-CL fluorite (Fig. 26). This fluid infiltration and dissolution event coincided with cassiterite precipitation, as indicated by the numerous cassiterite grains present within the bright-CL fluorite (Fig. 26 and 27). Unlike the other types of fluorite, these different generations of Sn-related fluorite II all have similar trace element chemistry (Fig. 58), suggesting fluids with very similar chemistry.

The dissolution features in fluorite indicate that a change in the crystallization environment caused fluorite solubility to fluctuate. Changes that could have caused the dissolution of fluorite include: an increase in temperature or pressure (Tropper and Manning, 2007), an increase in NaCl concentrations in the fluid (Tropper and Manning, 2007), a decrease in pH (Richardson and Holland, 1979), or a decrease in the F concentration (Nordstrom and Jenne, 1977). With the exception of a change in T or P, any of these changes would reflect the infiltration of fluids with different characteristics into the system. Fluorite precipitation followed fluorite dissolution, which in some cases resulted in fluorite with very similar chemistry to the previous generation. In W-related fluorite, the dissolution and reprecipitation of fluorite was concurrent with wolframite and REE mineral precipitation. Wolframite can precipitate due to a decrease in temperature, NaCl concentration, or an increase in pH (Wood and Samson, 2000). Rare earth element minerals (e.g., monazite, bastnäsite), can precipitate due to an increase in pH (Wood and Williams-Jones, 1994; Migdisov et al., 2016), a decrease in temperature (Migdisov et al., 2016), or due to a decrease in ligand concentrations, such as fluorine (Wood and Williams-Jones, 1994) or chlorine (Migdisov et al., 2016) in the fluid. The simplest scenario to precipitate REE minerals, fluorite, and wolframite would involve a decrease in temperature and an increase in pH, potentially by fluid mixing or wall-rock interaction.

In Sn-related fluorite II, the later precipitation of fluorite is concurrent with cassiterite precipitation. As cassiterite also precipitated along with the second generation of fluorite, the causes for cassiterite precipitation need to be considered. These are: oxidation (Heinrich, 1990), and increase in pH (Taylor and Wall, 1993), and a decrease in temperature (Bhalla et al., 2005). Similar to the W-related fluorite, the simplest scenario to precipitate both fluorite and cassiterite would involve a decrease in temperature and an increase in pH, potentially by fluid mixing or wall-rock interaction.

The mineralization at Mount Pleasant could have resulted from a single fluid, evolving over time due to selective precipitation of the ore minerals (i.e., cassiterite, wolframite, and molybdenite). The alternative hypothesis is that multiple fluids were responsible for the various types of mineralization. The more complex growth history of Sn-related fluorite compared to the relatively simple W- and Mo-related fluorite suggests that the fluids responsible for Sn mineralization had different histories and compositions, and potentially had different origins.

The mineral textures and relationships between fluorite, REE-minerals, wolframite, and cassiterite can be explained by the interplay of different fluids or by the interaction between magmatic-hydrothermal fluids and the host rocks.

5.3 Implications of Fluorite Chemistry

Tungsten-, Mo-, and Sn-related fluorite are differentiated best by their Fe/Rb ratios. The three Rb-Fe populations are defined by Fe/Rb ratios of ~100, ~20, and ~40, for W-, Mo-, and Sn-related fluorite, respectively. A question is whether these distinct Fe/Rb ratios reflect precipitation from compositionally different fluids or from a single evolving fluid under different physicochemical conditions (i.e. different temperature, pressure, fO_2 , pH), which would affect the partitioning of Fe and Rb, as well as other elements, into fluorite.

Trace-element concentrations in a mineral precipitating from a fluid are controlled by the concentration of the elements in the fluid and the relevant mineral-fluid partition coefficients. Partition coefficients vary as a function of the elasticity of a crystal lattice and can be predicted using lattice-strain theory (Blundy and Wood, 1994; van Hinsberg et al., 2010). This in turn allows partitioning to be explained via its dependence on pressure, temperature, and fluid composition (van Hinsberg et al., 2010). Sn-W deposits typically form over a temperature range of 200 to 500°C (Bodnar et al., 2014), which is very similar to the temperatures estimated for Mount Pleasant (Davis and Williams-Jones, 1985; Samson, 1990; Inverno and Hutchinson, 2004; Assadzadeh et al., 2017). A range of 300°C would have an insufficient effect on the partitioning of Fe and Rb into fluorite (cf. Yang and van Hinsberg, 2019) to explain the trends on Figure 4.34. Pressures within the Mount Pleasant system likely varied from 250 to 750 bars (< 1 km depth)(Samson 1990), which would cause negligible effects on Fe and Rb partitioning (Green and Pearson, 1987; Ulmer, 1989), especially given the similar chemistry of fluorite from Sn-related fluorite at Mount Pleasant to that from the East Kemptville Sn deposit, which will be discussed below, and was emplaced at a depth of > 14 km (Kontak et al., 2001). Partitioning cannot explain the markedly different compositions that fluorite associated with different ore minerals exhibit.

Another hypothesis is that the distinct Fe/Rb ratios could be the result of compositionally different fluids. Audetat et al. (2000) concluded that metal ratios in ore-forming fluids dictated the overall metal ratios in a variety of deposits in the Mole Granite, Australia. If each Fe/Rb trend at Mount Pleasant represents a unique fluid, then this implies three sources for these fluids. This suggests that each trend represents an evolved magma unique to each type of mineralization. As mentioned before (see Geologic Setting), three granitic phases are associated with, and have been implied to be responsible for, the Sn-W-Mo mineralization. Three different fluid histories are also supported by the different CL textures of the W-, Mo-, and Sn-related fluorite, in addition to the compositional differences of each type of fluorite. This evidence suggests compositionally different fluids as the most plausible cause of the different Fe/Rb ratios in fluorite associated with different ore minerals.

As described in the Results section, the concentrations of elements in the Mount Pleasant fluorite show a variety of coherent trends and correlations that have different characteristics for different

element pairs. There are three key types of trends: positive linear (Fig. 4.33), positive curved (Fig. 4.33), and negative curved (Fig. 4.32). These trends and correlations could be the result of: 1) crystal interface kinetics, 2) Mixing of two compositionally different fluids, 3) how elements are accommodated into the fluorite structure, or 4) Rayleigh fractionation during magma crystallization. A delay of trace element incorporation due to crystal interface kinetics would result in an increase in concentration of all elements over time, which is not exhibited in fluorite crystals (Figs. 4.41-4.51). Changing fluid composition over time can be assessed by comparing the trace element chemistry of the growth zones. One hypothesis to consider is whether these represent fluid mixing. Each trend could represent mixing with meteoric water where the low concentration endmembers are the meteoric end of the trend. This hypothesis can be tested by examining how REE concentrations vary through a crystal. The ionic radii of LREE are more similar to Ca than HREE, and the stability of REE complexes increase with atomic weight from La to Lu, such that the LREE are more compatible in fluorite and will become progressively depleted in a fluid as a result of fluorite precipitation (Möller et al., 1976; Ekambaram et al., 1986). Thus, the ratio of LREE to HREE (commonly expressed as La/Yb) has been used to determine relative age relationships (i.e., early vs late) between fluorite crystals and zones in a system (Eppinger and Closs, 1990; Hill et al., 2000; Ehya, 2012). Although W, Mo, and Sn-related fluorite exhibit the same range in La and Yb concentrations, all the high concentration endmembers of all Fe-Rb trends are characterized by high La/Yb (Fig. 5.2), and all the low concentration endmembers of all Fe-Rb trends are characterized by low La/Yb. This implies that the high Fe, Rb, and La/Yb endmembers represent earlier formation (Fig. 5.2). The low Fe and Rb concentration endmembers of each trend converge near the origin and have low La/Yb, and would suggest a later formation if fluorite crystallization controlled the REE chemistry of the fluids. This low Fe, Rb, and La/Yb endmember is depleted in all elements with the exception of the REE. Iron and Rb, in addition to Cu, Zn, Sr, and Cs, are negatively correlated with all the REE and Y (Fig. 4.32). In addition the low La/Yb ratios correlate to some replacement and dissolution features (Fig. 4.39). Mixing could also explain the precipitation of wolframite and cassiterite, as a fluid mixing event is the most commonly invoked process for their precipitation (Heinrich, 1990; Wood and Samson, 2000). This hypothesis would imply that the high Fe, Rb, and La/Yb endmember represents the magmatic-hydrothermal fluid composition, which is also supported by the higher concentration of metals compared to the low Fe, Rb, and La/Yb endmember. However, the high concentrations of REE demonstrate that this low Fe, Rb, and La/Yb fluid was relatively enriched in REE (Fig. 4.41), which suggests it was not an external, low-temperature groundwater of meteoric or basinal origin, as such fluids should have had much lower concentrations of REE than any magmatic fluid. In addition, mixing is inconsistent with the curved trends (e.g., Cs vs Rb) as mixing between two fluids should result in linear correlations (Faure, 1998).

Another hypothesis is that these trends are a reflection of how each element is being accommodated into the fluorite crystal structure. Iron, Rb, Cu, Zn are positively correlated. This could suggest that Fe^{3+} and Rb^{1+} are accommodated into the fluorite structure in the form of a coupled substitution, written as: $\text{Fe}^{3+} + \text{Rb}^{1+} \rightleftharpoons 2\text{Ca}^{2+}$

The combined ionic radius for two Ca^{2+} cations is 2 Å and the combined ionic radius for one Fe^{3+} and one Rb^{1+} is 2.12 Å. This is a less than 10% difference in ionic radius, making this a potentially favorable coupled substitution. This hypothesis, however, cannot explain the curved trends exhibited when plotting these elements against Sr, Cs, and REE, because a coupled substitution would result in element pairs either increasing or decreasing together. Also, this hypothesis does not explain the positive correlation between elements that would not be accommodated into fluorite via a coupled substitution, for example Fe^{3+} (in the Fe-Rb model) and Zn^{2+} (Fig. 4.33).

A fourth hypothesis is that these trends are a reflection of Rayleigh fractionation during crystallization and/or fluid exsolution in the source magmas. The nature of the fluctuations in trace-element concentrations within a single fluorite crystal (Fig. 5.3), suggest repeated release of fluid from sequential batches of magma or from a single magma that underwent pulsed crystallization. The similarity in concentration for a given element of the highs and lows in each “pulse” in the fluorite patterns and the presence of unidirectional solidification textures in the Mount Pleasant granites (Sinclair et al., 2006) suggest that the fluctuations are the result of pulsed crystallization of a single magma. In such a model, the trace-element patterns would have been controlled by either mineral-melt partition coefficients ($D^{\text{min/melt}}$) and/or fluid-melt partition coefficients ($D^{\text{fluid/melt}}$). An example is the relationship between Rb and Zn. If $D^{\text{min/melt}}$ controlled the trace element chemistry of the fluids (and hence fluorite), Zn (an incompatible element in rock-forming minerals) would exhibit a negative correlation with Rb (a compatible element in alkali feldspars), which it does not (Fig. 5.4). If $D^{\text{fluid/melt}}$ were controlling the trace element chemistry of fluorite, Zn (a compatible element in the fluid) would exhibit a positive correlation with Rb (another compatible element in the fluid), which it does (Fig. 5.4). The relationship between Fe and Rb with Cs (Fig. 4.33), in addition to Cu, Zn, and Sr, suggests these curved trace element patterns are the result of Rayleigh fractionation during fluid exsolution as the magma evolves.

The concentration of two elements that are compatible in a fractionating phase, such as a hydrothermal fluid, will define curves such as those shown in figures 5.5a and 5.5b, the shape of which will depend on the relative $D^{\text{fluid/melt}}$ values for the elements. Concentration will decrease as the fraction of melt remaining (f) decreases with time. The pattern exhibited when Cs is plotted against Fe, Rb, Cu, Zn, and Sr (Fig 5.6) is consistent with it having a higher partition coefficient into the fractionating phase than the other compatible elements (Zajacz et al., 2008) (Fig. 5.5a and 5.5b). This figure is consistent with the more rapid depletion of Cs in the melt than Fe, Rb, Cu, Zn, and Sr because Cs is more compatible in the fluid. Similarly, a plot of an incompatible element versus a compatible element will show a curved negative correlation (Fig. 5.7). The curved negative correlation between the REE and Fe, Rb, Cu, Zn, Sr, and Cs (Fig. 4.32) can also be explained by Rayleigh fractionation during fluid exsolution in the source magmas. In this figure the fluid increased in REE concentrations over time because the REE would have been incompatible in the fluid, and Fe, Rb, Cu, Zn, Sr, and Cs concentrations decreased over time because they would have been compatible in the fluid (Zajacz et al., 2008). In conclusion, Rayleigh fractionation can explain the observed patterns in the trace element chemistry of fluorite, and compositionally different fluids can explain the three distinct trends within the overall trends, which is best represented by the Fe vs Rb plot (Fig. 4.34).

5.4 Comparison with Other Deposits

Out of all trace-element pairings, the Fe/Rb ratios in fluorite from Mount Pleasant define the most distinct populations with respect to the primary ore minerals that the fluorite is associated with (i.e., W, Mo, or Sn-related). Trace-element indicators are not always useful when examined in other deposits and trace elements may not show the same relationships when examined in different deposits (Gagnon et al., 2003). In what follows, the Fe/Rb ratios in fluorite from Mount Pleasant are compared to Fe/Rb ratios from fluid inclusions in other deposits. This comparison is approached with the assumption that Fe/Rb in fluorite is a proxy for fluid composition, as are fluid inclusions.

East Kemptville is a Sn deposit located in southern Nova Scotia. Cassiterite is the primary ore mineral, but the deposit also contains base metal sulfides and minor amounts of wolframite and molybdenite. The deposit is hosted in veins and massive greisens, similar to Mount Pleasant. Fluorite is associated with cassiterite and base metal sulfides such as sphalerite (Halter et al., 1996). Fluorite from the East Kemptville Sn deposit was analyzed as part of this study, and has an Fe/Rb ratio of 39, which is very similar to the Fe/Rb ratio of 43 for Sn-related fluorite at Mount Pleasant (Fig. 5.8).

The Mole granite is located in eastern Australia and is composed of three texturally distinct variants that are mineralogically and geochemically identical (Pettke et al., 2005), much like Mount Pleasant. The Mole granite exhibits a zonal distribution of Sn, W, base metal, and Au-Bi deposits (Audetat et al., 2000). The Sn-W mineralization in the Mole granite is similar to that at Mount Pleasant in terms of the style of mineralization (veins of wolframite and open space filling of cassiterite) to the association of mineralization with fluorite (wolframite intergrown with fluorite and synchronous precipitation of cassiterite and fluorite) (Audetat et al., 2000). Audetat et al. (2000) presented fluid inclusion data from Sn, W, and Au-Bi deposits in the Mole granite. The average Fe/Rb ratio for all the fluid inclusions in the Mole granite deposits is 43, identical to the average Fe/Rb ratio of Sn-related fluorite at Mount Pleasant. Although East Kemptville and Mole granite deposits were emplaced at greater depths, > 14 km (Kontak et al., 2001) and 4 ± 1 km (Audetat, 1999), respectively, they have similar Fe/Rb ratios to that of the Sn-related fluorite at Mount Pleasant (Fig. 5.8).

The Cave Peak Mo-Nb (Cu-W) deposit in Texas consists of three Mo orebodies associated with several intrusive granites and a breccia pipe (Audetat et al., 2008). A zone within quartz crystals contains numerous mineral inclusions of molybdenite, biotite, columbite, cassiterite, and yttrifluorite, with syn-mineralization fluid inclusions having an average Fe/Rb ratio of 4 (Audetat et al., 2008). The Fe/Rb ratio from the Cave Peak Mo-Nb (Cu-W) deposit is the lowest reported here, but is most similar to the Fe/Rb ratio of 21 for Mo-related fluorite at Mount Pleasant.

Lüders et al. (2009) analyzed fluid inclusions in quartz, fluorite, and rhodochrosite associated with molybdenite and associated with sulfides in the Sweet Home Mo mine in Colorado. The fluid inclusions associated with molybdenite have an average Fe/Rb ratio of 9, and the fluid inclusions associated with sulfides have an average Fe/Rb ratio of 26. The average Fe/Rb ratio for all the

fluid inclusion populations is 16, which is similar to the Fe/Rb ratio of Mo-related fluorite at Mount Pleasant.

Li et al. (2012) analyzed fluid inclusions in quartz associated with molybdenite and in quartz associated with polymetallic sulfides in the Yuchiling porphyry Mo deposit. The fluid inclusions in quartz associated with molybdenite have an Fe/Rb ratio of 18 and fluid inclusions in quartz associated with polymetallic sulfides have a Fe/Rb ratio of 23. The average Fe/Rb ratio for the fluid inclusion populations is 20, similar to the Fe/Rb ratio of Mo-related fluorite at Mount Pleasant. Both the Sweet Home Mo mine and the Yuchiling porphyry Mo deposit contain molybdenite and later sulfides, but lack wolframite and cassiterite (Lüders et al. 2009; Li et al., 2012).

The above analysis shows that there are similarities in the Fe/Rb ratios for a given metal association among these deposits. The Fe/Rb ratios from Mount Pleasant, and all other deposits examined, range from approximately 1 to 200, with low Fe/Rb ratios (~20) typically associated with Mo mineralization, and medium Fe/Rb ratios (~40) typically associated with Sn mineralization. Although the W-mineralization at Mount Pleasant is associated with high Fe/Rb ratios (~100), this is not seen in fluid inclusions from other W-rich deposits. Unlike Mount Pleasant, where evidence indicates the different metals reflect different source magmas, the Mole granite deposits were sourced from the Mole granite and the telescoped mineralization around it has been concluded to be a result of selective precipitation (Audetat et al., 2008). This selective precipitation has resulted in a spatial and temporal distribution of different ore types with similar Fe/Rb ratios in fluorite. This implies that Fe/Rb is indicative of source and, in certain locations like Mount Pleasant, can be an indicator of specific mineralization.

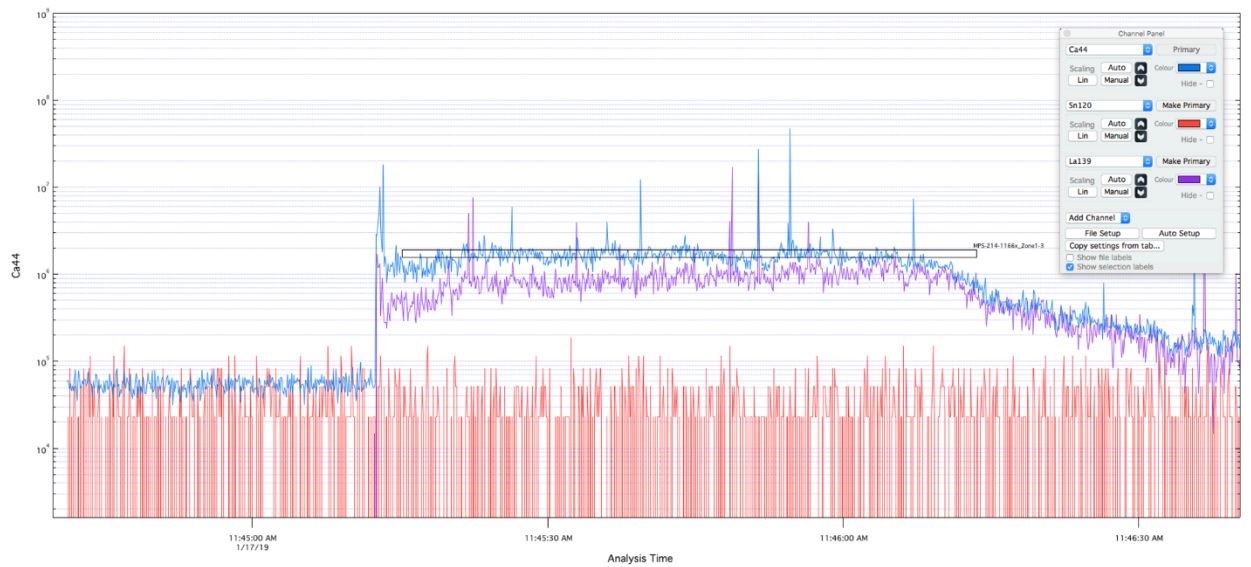


Figure 5.1 An example of a laser-ablation spectrum of fluorite showing that Sn is below the limit of detection.

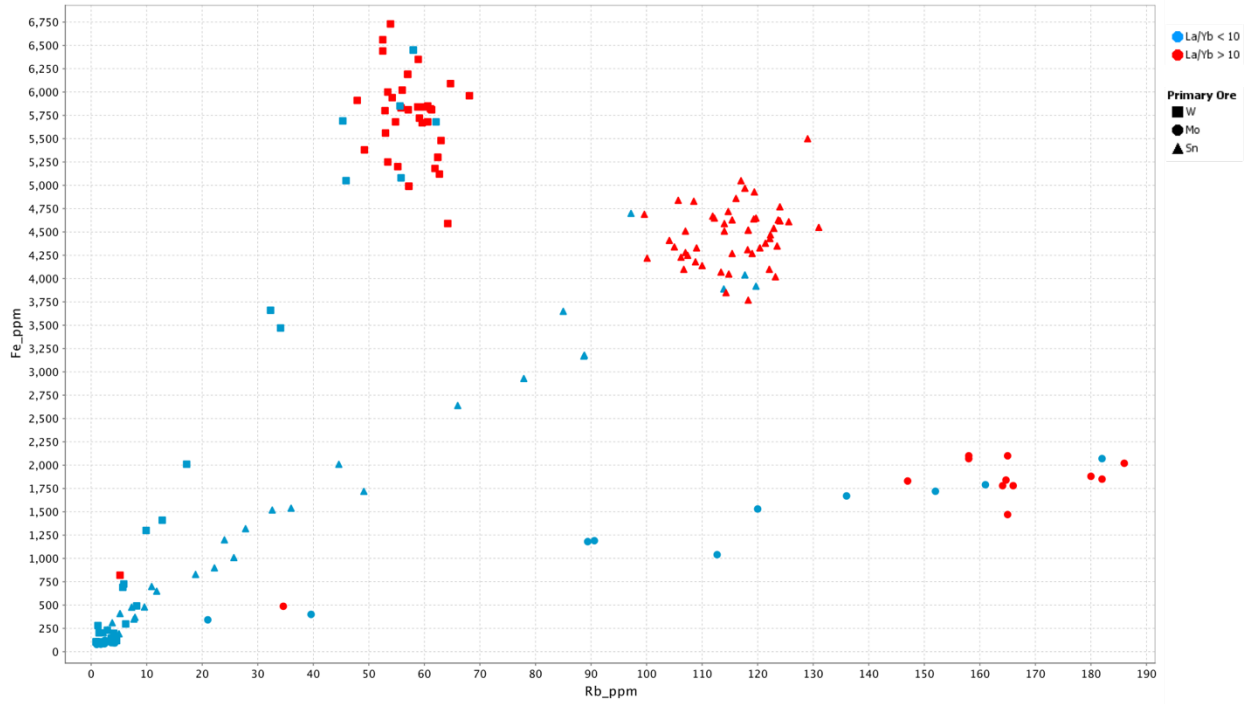


Figure 5.2 Iron versus Rubidium plot showing all Fe/Rb trends and that the high Fe and Rb concentration endmembers have a higher La/Yb ratio and the low Fe and Rb concentration endmembers have a lower La/Yb ratio.

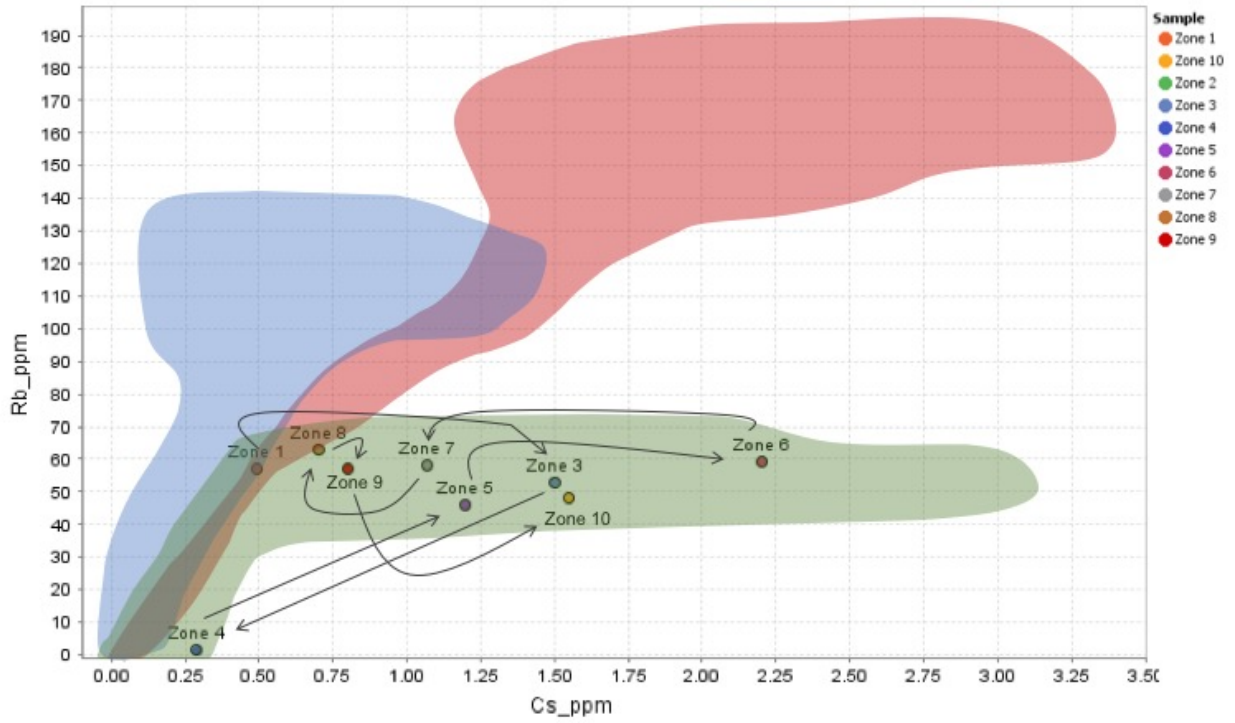


Figure 5.3 Cesium versus rubidium plot showing how Rb and Cs vary from zone to zone within a single crystal of W-related fluorite, overlain by the Cs/Rb fields for the entire data set.

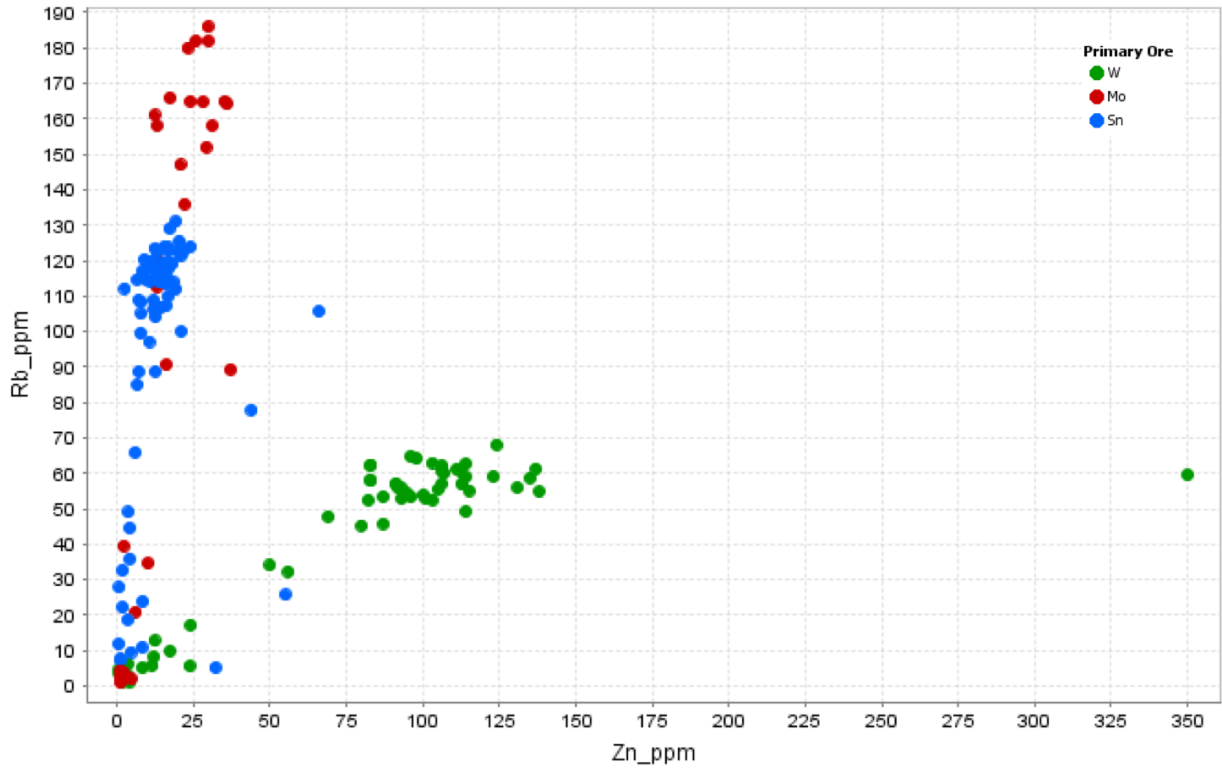


Figure 5.4 Zinc versus rubidium plot showing a positive correlation between these two elements in each population.

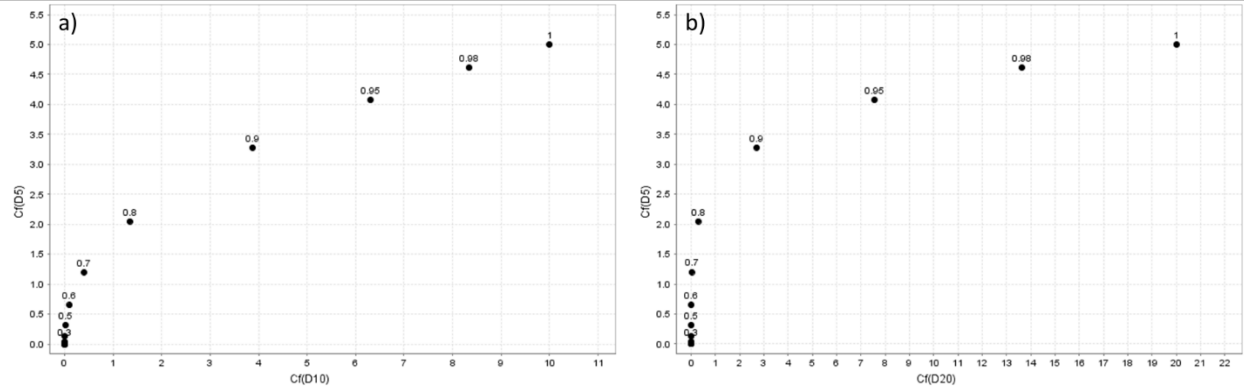


Figure 5.5 Variation in concentration (C_f) of two compatible elements in a fractionating phase using the Rayleigh fractionation model, based on the equation: $\frac{C_f}{C_0} = f^{D-1}$. The initial concentrations of the elements in the reservoir (C_0) is 1. In a crystallizing magma, the fractionation phase could either be a mineral or a hydrothermal fluid. Data labels = f , the fraction of melt remaining. Both a) and b) illustrate the relationships for moderately compatible elements with partition coefficients (D) = 10 and 5 (a) and 20 and 5 (b). Such fractionation will generate minerals or fluids with positively correlated curved trends, where the early-formed phases will have high concentrations that will decrease with time.

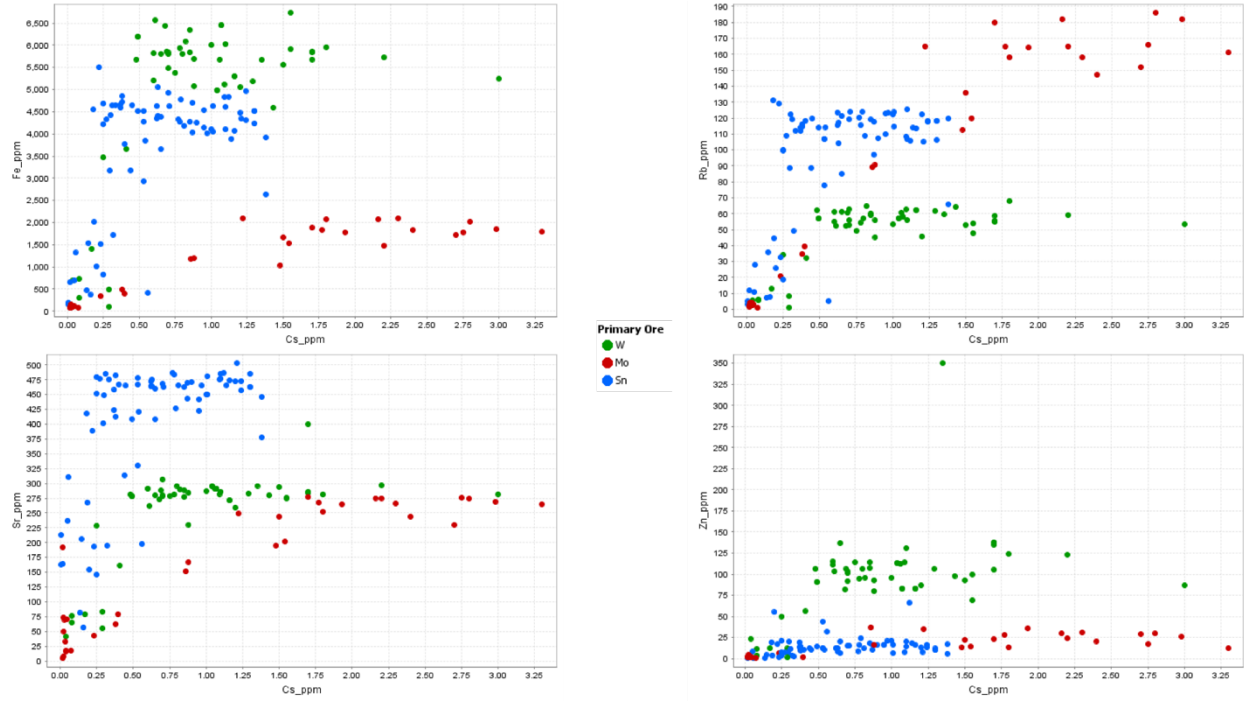


Figure 5.6 Bivariate plots showing Cs plotted against Fe, Rb, Zn, and Sr.

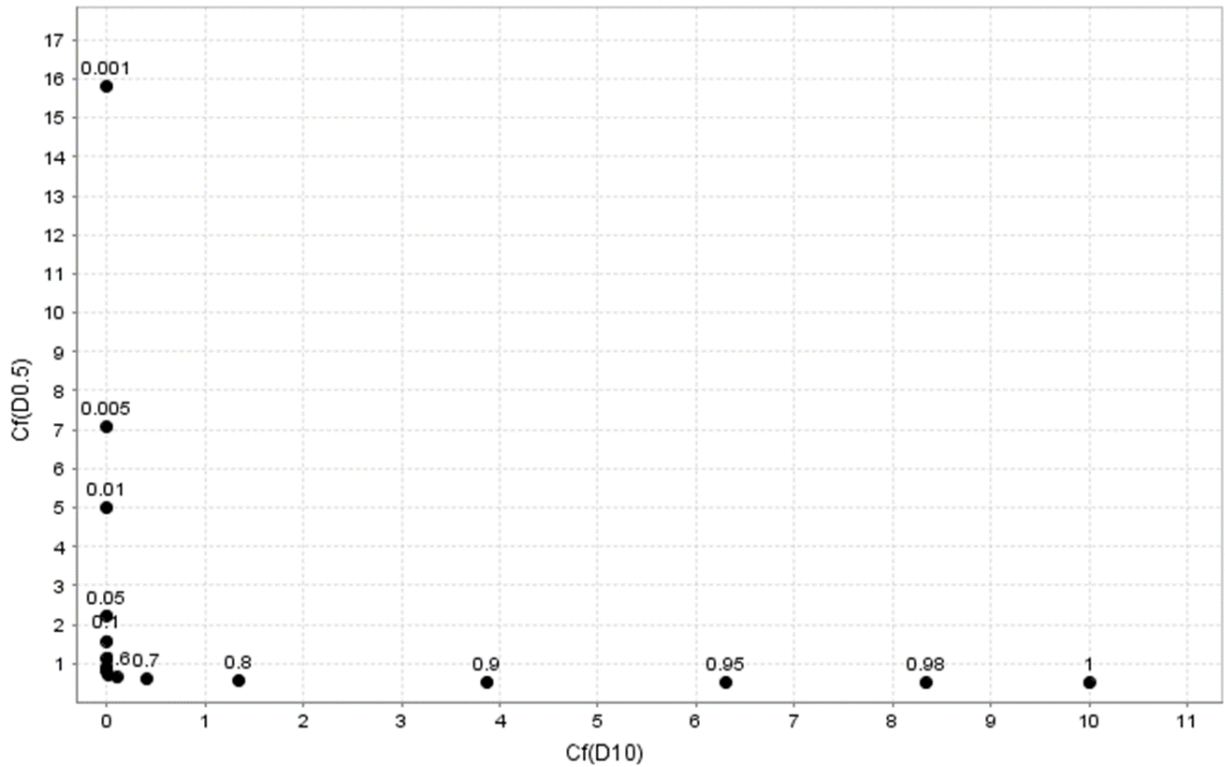


Figure 5.7 Rayleigh fractionation model for concentrations (C_f) of a moderately incompatible element ($D = 0.5$) relative to a moderately compatible element in a fractionating phase. Variables are the same as in Figure 5.6.

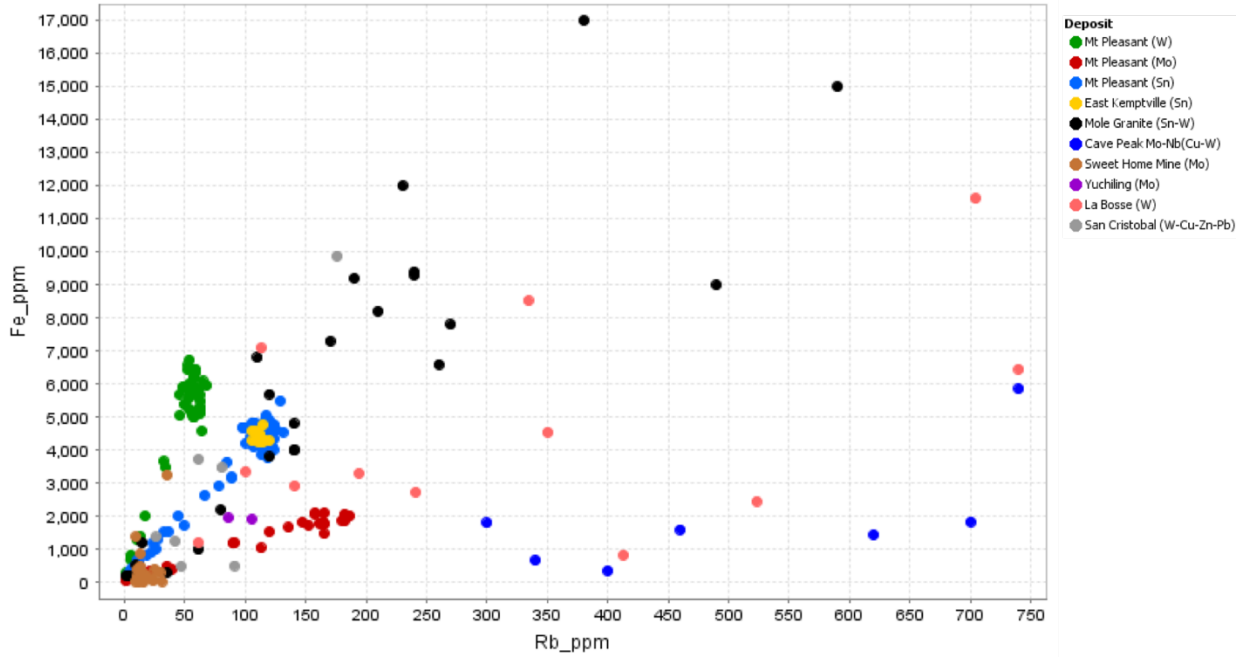


Figure 5.8 Iron versus rubidium plot showing the various Fe/Rb trends at Mount Pleasant and in other W, Mo, and Sn deposits. Data sources for other deposits are provided in the text.

CHAPTER 6

Conclusions

The Mount Pleasant Sn-W-Mo deposit hosts two mineralized zones, the North Zone and Fire Tower Zone, that contain different proportions of ore minerals, making it a suitable place to examine the relationship between metal concentrations in hydrothermal fluids and metal endowment in ore deposits. Fluorite is ubiquitous at Mount Pleasant and is associated with wolframite, molybdenite, and cassiterite, making it a good candidate as a proxy for fluid composition. One of the main objectives of this study was to assess if the strikingly different metal endowments of the North Zone and Fire Tower Zone were the result of compositionally different fluids containing high concentrations of a particular ore metal or whether the various ore assemblages were the result of selective precipitation of ore minerals from compositionally similar fluids. This was achieved by examining the growth history (using optical and cathodoluminescence imaging) and the trace-element chemistry of fluorite (using laser ablation ICP-MS spectrometry) in the various metal assemblages. Optical microscopy, EDS analyses, CL imaging, and the trace-element chemistry in fluorite show a complexity that reflects a complex fluid architecture. Another objective of this study was to determine the character of the ore-forming fluid(s) by examining the growth history (i.e. using CL) and compositional evolution (i.e. intra-crystal trace-element behavior) of fluorite to investigate the fluid history of the various zones of mineralization.

The conclusions of this study are as follows:

- High laser power (4.1 mJ) and a high repetition rate (100-150 Hz) were the optimal ablation parameters that resulted in the highest quality spectra obtainable with the system used.
- Fluorite associated with W, Mo, and Sn mineralization are each characterized by different fluid histories based on the CL characteristics of the associated fluorite.
- Wolframite and cassiterite mineralization are spatially and temporally associated with REE minerals.
- Fluorite associated with W mineralization has a higher W/Mo ratio (~3) than Mo-related fluorite (~0.5).
- No Sn was detected in samples of fluorite from Mount Pleasant.
- Three distinct populations of fluorite trace-element chemistry, represented by W-, Mo-, and Sn-related fluorite, are interpreted to have resulted from Rayleigh fractionation during fluid exsolution in the source magmas.
- The wolframite, molybdenite, and cassiterite mineralization are each the product of compositionally different fluids based on the three distinct populations that exist in the Rayleigh fractionation model.

- Trace-element fluctuations in single fluorite crystals suggest that the source magmas underwent pulsed crystallization.
- It is inferred from the Rayleigh fractionation model that each type of mineralization originated from one of the three associated granitic phases.
- A comparison of Mount Pleasant with other deposits shows that Mo mineralization is characterized by low Fe/Rb ratios (~20) in fluorite and/or fluid inclusions, and that Sn mineralization is characterized by high Fe/Rb ratios (~40) in fluorite and/or fluid inclusions.
- Tungsten mineralization is characterized by high (~100) Fe/Rb ratios in fluorite at Mount Pleasant but in other W deposits, fluid inclusions have Fe/Rb ratios ranging from ~1 to ~160.
- In fluorite and/or fluid inclusions, Fe/Rb ratios may be a useful parameter to discriminate between different fluid sources.

Suggestions for Future Work

There are four recommendations for future work.

- Employ the use of a femtosecond laser to analyze major and trace elements in fluid inclusions to better understand the fluid architecture and history at Mount Pleasant.
- Obtain oxygen isotope data on chlorite, quartz, and cassiterite to further assess fluid origins and the potential role of fluid mixing.
- Cassiterite dating would be beneficial to compare with molybdenite age dates from Thorne et al. (2013) to quantify the time between the two mineralization events, if any.
- Conduct more fluorite trace-element studies in other Sn-W-Mo deposits to further test the conclusions from this study regarding the uniqueness of fluid trace-element chemistry (e.g., Fe/Rb ratios) in different types of ore assemblages and to better understand the processes that controlled trace-element chemistry.

REFERENCES

- Allègre, C.J., Provost, A., Jaupart, C., 1981. Oscillatory zoning: a pathological case of crystal growth. *Nature* 294, 223–228.
- Assadzadeh, G.E., Samson, I.M., Gagnon, J.E., 2017. The trace element chemistry and cathodoluminescence characteristics of fluorite in the Mount Pleasant Sn-W-Mo deposits: Insights into fluid character and implications for exploration. *Journal of Geochemical Exploration* 172, 1–19.
- Audétat, A., 1999. The magmatic-hydrothermal evolution of the Sn/W-mineralized Mole Granite (Eastern Australia). ETH Zurich.
- Audétat, A., Günther, D., Heinrich, C.A., 2000. Causes for Large-Scale Metal Zonation around Mineralized Plutons: Fluid Inclusion LA-ICP-MS Evidence from the Mole Granite, Australia 19.
- Audetat, A., Pettke, T., Heinrich, C.A., Bodnar, R.J., 2008. Special Paper: The Composition of Magmatic-Hydrothermal Fluids in Barren and Mineralized Intrusions. *Economic Geology* 103, 877–908.
- Bailey, A.D., Hunt, R.P., Taylor, K.N.R., 1974. An E.S.R. study of natural fluorite containing manganese impurities. *Mineral. mag.* 39, 705–708.
- Balogun, F.A., Ojo, J.O., Ogundare, F.O., Fasasi, M.K., Hussein, L.A., 1999. TL response of a natural Fluorite. *Radiation Measurements* 5.
- Bhalla, P., Holtz, F., Linnen, R.L., Behrens, H., 2005. Solubility of cassiterite in evolved granitic melts: effect of T, fO₂, and additional volatiles. *Lithos* 80, 387–400.
- Bill, H., Calas, G., 1978. Color centers, associated rare-earth ions and the origin of coloration in natural fluorites. *Phys Chem Minerals* 3, 117–131.
- Blundy, J., Wood, B., 1994. Prediction of crystal–melt partition coefficients from elastic moduli. *Nature* 372, 452–454.
- Bodnar, R.J., Lecumberri-Sanchez, P., Moncada, D., Steele-MacInnis, M., 2014. Fluid Inclusions in Hydrothermal Ore Deposits, in: *Treatise on Geochemistry*. Elsevier, pp. 119–142.
- Davis, W.J., Williams-Jones, A.E., 1985. A fluid inclusion study of the porphyry-greisen, tungsten-molybdenum deposit at Mount Pleasant, New Brunswick, Canada. *Mineral. Deposita* 20.
- Deng, X.-H., Chen, Y.-J., Yao, J.-M., Bagas, L., Tang, H.-S., 2014. Fluorite REE-Y (REY) geochemistry of the ca. 850Ma Tumen molybdenite–fluorite deposit, eastern Qinling, China: Constraints on ore genesis. *Ore Geology Reviews* 63, 532–543.

- Ehya, F., 2012. Variation of mineralizing fluids and fractionation of REE during the emplacement of the vein-type fluorite deposit at Bozijan, Markazi Province, Iran. *Journal of Geochemical Exploration* 112, 93–106.
- Ekambaram, V., Brookins, D.G., Rosenberg, P.E., Emanuel, K.M., 1986. Rare-earth element geochemistry of fluorite-carbonate deposits in western Montana, U.S.A. *Chemical Geology* 54, 319–331.
- Eppinger, R.G., Closs, L.G., 1990. Variation of trace elements and rare earth elements in fluorite; a possible tool for exploration. *Economic Geology* 85, 1896–1907.
- Faure, G., 1998. *Principles and Applications of Geochemistry*.
- Gagnon, J.E., Samson, I.M., Fryer, B.J., Williams-Jones, A.E., 2003. Compositional Heterogeneity in Fluorite and the Genesis of Fluorite Deposits Insights from LA-ICP-MS Analysis. *The Canadian Mineralogist* 41, 365–382.
- Götze, J., Plötze, M., Trautmann, T., 2005. Structure and luminescence characteristics of quartz from pegmatites. *American Mineralogist* 90, 13–21.
- Götze, J., Schertl, H.-P., Neuser, R.D., Kempe, U., Hanchar, J.M., 2013. Optical microscope-cathodoluminescence (OM-CL) imaging as a powerful tool to reveal internal textures of minerals. *Miner Petrol* 107, 373–392.
- Green, T.H., Pearson, N.J., 1987. An experimental study of Nb and Ta partitioning between Ti-rich minerals and silicate liquids at high pressure and temperature. *Geochimica et Cosmochimica Acta* 51, 55–62.
- Halter, W.E., Williams-Jones, A.E., Kontak, D.J., 1996. The role of greisenization in cassiterite precipitation at the East Kemptville tin deposit, Nova Scotia. *Economic Geology* 91, 368–385.
- Harlov, D.E., Förster, H.-J., 2003. Fluid-induced nucleation of (Y+REE)-phosphate minerals within apatite: Nature and experiment. Part II. Fluorapatite. *American Mineralogist* 88, 1209–1229.
- Harlov, D.E., Förster, H.-J., Nijland, T.G., 2002. Fluid-induced nucleation of (Y + REE)-phosphate minerals within apatite: Nature and experiment. Part I. Chlorapatite. *American Mineralogist* 87, 245–261.
- Harlov, D.E., Wirth, R., Förster, H.-J., 2005. An experimental study of dissolution–reprecipitation in fluorapatite: fluid infiltration and the formation of monazite. *Contrib Mineral Petrol* 150, 268–286.
- Heinrich, C.A., 1990. The chemistry of hydrothermal tin(-tungsten) ore deposition. *Economic Geology* 85, 457–481.

- Hellmann, R., Tisserand, D., 2006. Dissolution kinetics as a function of the Gibbs free energy of reaction: An experimental study based on albite feldspar. *Geochimica et Cosmochimica Acta* 70, 364–383.
- Hill, G.T., Campbell, A.R., Kyle, P.R., 2000. Geochemistry of southwestern New Mexico fluorite occurrences implications for precious metals exploration in fluorite-bearing systems. *Journal of Geochemical Exploration* 68, 1–20.
- Hunt, P.A., Roddick, J.C., 1990. Radiogenic Age of Isotopic Studies: (No. 3). Geological Survey of Canada.
- Inverno, C.M.C., Hutchinson, R.W., 2006. Petrochemical discrimination of evolved granitic intrusions associated with Mount Pleasant deposits, New Brunswick, Canada. *Applied Earth Science* 115, 23–39.
- Inverno, C.M.C., Hutchinson, R.W., 2004. The endogranitic tin zone, Mount Pleasant, New Brunswick, Canada and its metallogenesis. *Applied Earth Science* 113, 261–288.
- Jakeš, P., 1982. Transactions of the Royal Society of Edinburgh: Earth Sciences. *Geochimica et Cosmochimica Acta* 46, 115.
- Jeffries, T.E., Jackson, S.E., Longerich, H.P., 1998. Application of a frequency quintupled Nd:YAG source ($\lambda=213$ nm) for laser ablation inductively coupled plasma mass spectrometric analysis of minerals. *Journal of Analytical Atomic Spectrometry* 13, 935–940.
- Jimenez, T., 2011. Variation in Hydrothermal Muscovite and Chlorite Composition in the Highland Valley Porphyry Cu-Mo District, British Columbia, Canada. The University of British Columbia.
- Kooiman, G.J.A., McLeod, M.J., Sinclair, W.D., 1986. Porphyry tungsten-molybdenum orebodies, polymetallic veins and replacement bodies, and tin-bearing greisen zones in the Fire Tower Zone, Mount Pleasant, New Brunswick. *Economic Geology* 81, 1356–1373.
- Kuikka, J., 2018. Major and trace element characteristics of biotite and chlorite as proxies for gold ore mineralization. *Geotieteiden ja maantieteen laitos*.
- Li, N., Ulrich, T., Chen, Y.-J., Thomsen, T.B., Pease, V., Pirajno, F., 2012. Fluid evolution of the Yuchiling porphyry Mo deposit, East Qinling, China. *Ore Geology Reviews* 48, 442–459.
- Lüders, V., Romer, R.L., Gilg, H.A., Bodnar, R.J., Pettke, T., Misantoni, D., 2009. A geochemical study of the Sweet Home Mine, Colorado Mineral Belt, USA: hydrothermal fluid evolution above a hypothesized granite cupola. *Miner Deposita* 44, 415–434.

- Makin, S.A., Simandl, G.J., Marshall, D., 2013. Fluorite and its potential as an indicator mineral for carbonatite-related rare earth element deposits 6.
- Mao, M., Simandl, G.J., Spence, J., Neetz, M., Marshall, D., 2015. Trace element composition of fluorite and its potential use as an indicator in mineral exploration 26.
- McCutcheon, S.R., Anderson, H.E., Robinson, P.T., 1997. Stratigraphy and eruptive history of the Late Devonian Mount Pleasant Caldera Complex, Canadian Appalachians. *Geol. Mag.* 134, 17–36.
- Migdisov, A., Williams-Jones, A.E., Brugger, J., Caporuscio, F.A., 2016. Hydrothermal transport, deposition, and fractionation of the REE: Experimental data and thermodynamic calculations. *Chemical Geology* 439, 13–42.
- Möller, P., Parekh, P.P., Schneider, H.-J., 1976. The application of Tb/Ca-Tb/La abundance ratios to problems of fluorspar genesis. *Mineral. Deposita* 11, 111–116.
- Nordstrom, D.K., Jenne, E.A., 1977. Fluorite solubility equilibria in selected geothermal waters. *Geochimica et Cosmochimica Acta* 41, 175–188.
- Pettke, T., Audétat, A., Schaltegger, U., Heinrich, C.A., 2005. Magmatic-to-hydrothermal crystallization in the W–Sn mineralized Mole Granite (NSW, Australia). *Chemical Geology* 220, 191–213.
- Pouliot, G., Barondeau, B., Sauve, P., Davis, M., 1978. Distribution of Alteration Minerals and Metals in the Fire Tower Zone at Brunswick Tin Mines LTD., Mount Pleasant Area, New Brunswick. *Canadian Mineralogist* 16, 223–237.
- Putnis, A., 2009. Mineral Replacement Reactions. *Reviews in Mineralogy and Geochemistry* 70, 87–124.
- Richardson, C.K., Holland, H.D., 1979. Fluorite deposition in hydrothermal systems. *Geochimica et Cosmochimica Acta* 43, 1327–1335.
- Samson, I.M., 1990. Fluid evolution and mineralization in a subvolcanic granite stock; the Mount Pleasant W-Mo-Sn deposits, New Brunswick, Canada. *Economic Geology* 85, 145–163.
- Schwinn, G., Markl, G., 2005. REE systematics in hydrothermal fluorite. *Chemical Geology* 216, 225–248.
- Sinclair, W.D., Kooiman, G.J.A., Martin, D.A., Kjarsgaard, I.M., 2006. Geology, geochemistry and mineralogy of indium resources at Mount Pleasant, New Brunswick, Canada. *Ore Geology Reviews* 28, 123–145.
- Taylor, J.R., Wall, V.J., 1993. Cassiterite solubility, tin speciation, and transport in a magmatic aqueous phase. *Economic Geology* 88, 437–460.

- Thorne, K.G., Fyffe, L.R., Creaser, R.A., 2013. Re-Os geochronological constraints on the mineralizing events within the Mount Pleasant Caldera: implications for the timing of sub-volcanic magmatism. *Atlantic Geology* 49, 131.
- Tropper, P., Manning, C.E., 2007. The solubility of fluorite in H₂O and H₂O–NaCl at high pressure and temperature. *Chemical Geology* 242, 299–306.
- Ulmer, P., 1989. The dependence of the Fe²⁺-Mg cation-partitioning between olivine and basaltic liquid on pressure, temperature and composition: An experimental study to 30 kbars. *Contr. Mineral. and Petrol.* 101, 261–273.
- van Hinsberg, V.J., Migdisov, A.A., Williams-Jones, A.E., 2010. Reading the mineral record of fluid composition from element partitioning. *Geology* 38, 847–850.
- Whalen, J.B., Currie, K.L., Chappell, B.W., 1987. A-type granites: geochemical characteristics, discrimination and petrogenesis. *Contrib Mineral Petrol* 95, 407–419.
- Wood, S.A., Samson, I.M., 2000. The Hydrothermal Geochemistry of Tungsten in Granitoid Environments: I. Relative Solubilities of Ferberite and Scheelite as a Function of T, P, pH, and mNaCl. *Economic Geology* 95, 143–182.
- Wood, S.A., Williams-Jones, A.E., 1994. The aqueous geochemistry of the rare-earth elements and yttrium 4. Monazite solubility and REE mobility in exhalative massive sulfide-depositing environments. *Chemical Geology* 115, 47–60.
- Xu, C., Taylor, R.N., Li, W., Kynicky, J., Chakhmouradian, A.R., Song, W., 2012. Comparison of fluorite geochemistry from REE deposits in the Panxi region and Bayan Obo, China. *Journal of Asian Earth Sciences* 57, 76–89.
- Yang, L., van Hinsberg, V.J., 2019. Liquid immiscibility in the CaF₂-granite system and trace element partitioning between the immiscible liquids. *Chemical Geology* 511, 28–41.
- Zajacz, Z., Halter, W.E., Pettke, T., Guillong, M., 2008. Determination of fluid/melt partition coefficients by LA-ICPMS analysis of co-existing fluid and silicate melt inclusions: Controls on element partitioning. *Geochimica et Cosmochimica Acta* 72, 2169–2197.
- Zhang, W., Lentz, D.R., Charnley, B.E., 2017. Petrogeochemical assessment of rock units and identification of alteration/mineralization indicators using portable X-ray fluorescence measurements: Applications to the Fire Tower Zone (W-Mo-Bi) and the North Zone (Sn-Zn-In), Mount Pleasant deposit, New Brunswick, Canada. *Journal of Geochemical Exploration* 177, 61–72.

VITA AUCTORIS

NAME: James Greene
PLACE OF BIRTH: New Jersey, United States
YEAR OF BIRTH: 1994
EDUCATION: Stockton University, B.Sc., Galloway, NJ, 2016
University of Windsor, M.Sc., Windsor, ON, 2019